

Synthesis of carbon nanofibers made from nickel catalysts confined within hollow carbon spheres

by

Bonakele Patricia Mtolo

Student number: 737945

BSc (Hons)

A dissertation submitted to the Faculty of Science at the University of
the Witwatersrand, Johannesburg, in fulfilment of the requirement for
the degree of

Master of Science in Chemistry

Supervisor: Prof Neil J. Coville

Co-supervisor: Dr. Manoko S. Maubane-Nkadimeng

University of the Witwatersrand, Johannesburg, March 2020

DECLARATION

I hereby declare that this dissertation submitted to the University of the Witwatersrand, Johannesburg, is my own work, unaided work under the supervision of Professor Neil.J Coville and Doctor Manoko S. Maubane-Nkadimeng. The work has not been submitted for any degree or examined in any other university.

WITS
UNIVERSITY



A handwritten signature in black ink, appearing to read 'Bonakele Mtolo'.

Bonakele Patricia Mtolo

On the 18th day of March 2020 at the University of the Witwatersrand

ABSTRACT

Hollow carbon spheres (HCSs) are known to exhibit exceptional properties such as having a high surface to volume ratio, encapsulation ability and excellent chemical as well as thermal stability. The hollow cavity of the spheres can act as a nanoreactor to build structures such as carbon nanofibers (CNFs) and carbon nanotubes (CNTs) through an encapsulated metal, metal alloy or metal oxide catalyst. As such, this study reports on the encapsulation of nickel oxide inside hollow carbon spheres (NiO@HCSs). For comparison, NiO was also deposited outside HCSs to give NiO/HCSs catalyst. NiO particles were completely reduced to Ni at 450 °C under the continuous flow of H₂ gas (100 mL/min) to give Ni@HCSs for the particles deposited inside and outside HCSs, respectively. The synthesis of CNFs was achieved by the decomposition of acetylene gas (100 mL/min) over Ni@HCSs (0.5, 5, and 10 wt% Ni loading) using a chemical vapour decomposition (CVD) technique.

Transmission electron microscopy (TEM) studies showed that Ni/HCSs resulted in enormous growth of CNFs and agglomeration of the Ni catalyst particles. Ni@HCSs catalysts resulted in minimal agglomeration of Ni nanoparticles (NPs) at a low loading (0.5 wt%) when compared to a high loading (10 wt%). The average Ni grains were determined to be 12 ± 8 nm, 22 ± 5 nm and 51 ± 12 nm for 0.5 wt%, 5 wt% and 10 wt% Ni loading, respectively. To selectively prepare CNFs with a controllable size and morphology, the NiO@HCSs at lower loading (0.5 wt%) was used for the synthesis of the CNFs using acetylene and trichloroethylene (TCE) and further studies.

The effect of reaction parameters on the synthesis of the CNFs including temperature, growth time and flow rate was investigated. CNFs synthesized using acetylene showed the successful growth of monomodal and bimodal growth with straight and helical morphology at elevated temperatures. TEM analysis revealed that as the temperature increased, nickel fracturing occurred which resulted in the formation of thin CNFs (*ca.* 11 nm). The growth time had a significant impact on the CNFs yield and CNFs with variable lengths were observed. It was observed that H₂ flow rate modified the morphologies of the CNFs synthesized.

The CNFs synthesized using TCE as a carbon source resulted in a high yield of carbon. Various fiber morphologies (tripod-like, flower-like, CNFs with a hollow central core and rough outer edges) were observed. This indicated that the Ni particles underwent major reconstruction during CNF growth. It was also demonstrated that different nickel precursors (nickel acetate

hexahydrate, nickel chloride hexahydrate and nickel nitrate) only had a slight effect on the morphology of the CNFs. Raman studies revealed that the CNFs synthesized using nickel acetate resulted in the formation of a more graphitic carbon compared to other nickel compounds. The TGA data corroborated this finding.

DEDICATION

This work is dedicated to my dearest family:

My mother Nomvula Mtolo, my grandmother Nobulawo Nomthenjwa Mtolo, my aunt Fikile Maria Sefatsa, my cousin Thembeke Mtolo and younger sister Flatha Mtolo.

ACKNOWLEDGEMENTS

First and foremost, I would like to thank the almighty **GOD** for giving me the courage and strength when all seemed impossible. I would like to extend my profound gratitude to my supervisor Prof. Neil J. Coville for his outstanding and insightful contribution towards this work. A great thanks for all your support and guidance to the success of this project. A warm thanks goes to my co-supervisor Dr. Manoko Maubane-Nkadimeng for her great inputs, support and considerable efforts to hone this work.

This work would be incomplete without the research facilities provided by the Microscopy and Microanalysis unit (MMU) at the University of the Witwatersrand. To all the MMU team, I am truly grateful for your patience and assistance with the techniques. A warm thanks goes to Dr. Rudolph Erasmus for his assistance with Raman spectroscopy analysis. I would also like to thank Ms Rhadzu Rikhotso from CSIR Nanocentre, Pretoria, for her assistance with high resolution transmission electron microscopy (HRTEM) measurements.

A huge thanks goes to the **CATMAT** group for their positive criticism and valuable suggestion which helped to improve the outcome of this work. Special thanks goes to Ms Phumza Mente, Mr Orlette Mkhari, Mr Thomas Mongwe, Ms Thuli Buthelezi, and Ms Lerato Mokoloko, for your assistance with sample analysis. To my other colleagues in lab 116/120, thanks for your support, encouragements and making lab 116/120 to feel like a 'home away from home'. My heartfelt appreciation goes to Dr. B. K Mutuma for her kindness, time, and the great inputs she provided towards the accomplishment of this work.

I would also like to extend my thanks to my beloved friends and family who have been my pillar of strengths during this journey. I am truly grateful for all the love, supports and your kindness.

I would also like to acknowledge the National Research Foundation (NRF) and Wits Postgraduate Merit Award (PMA) for financial support. This research work would not have been possible without the assistance.

PRESENTATIONS AND AWARDS

Poster Presentations

- ❖ “Synthesis of carbon nanofibers made from nickel catalysts confined within hollow carbon spheres”, Catalysis Society of South Africa (CATSA) Conference, University of Cape Town, Langebaan, November 2019.
- ❖ “Synthesis of carbon nanofibers made from nickel catalysts confined within hollow carbon spheres”, The 10th Cross Faculty Symposium, Wits University, Johannesburg, September 2019.
- ❖ “Synthesis of carbon nanofibers made from nickel catalysts confined within hollow carbon spheres”, Centre of Excellence Annual Student Workshop, University of the Witwatersrand, Johannesburg, May 2019.
- ❖ “Synthesis of carbon nanofibers made from nickel catalysts confined within hollow carbon spheres”, The 43rd SACI National Convention, CSIR-ICC, Pretoria, December 2018.

Awards

- ❖ Won third prize, best poster presentation, CATSA, November 2019.
- ❖ MSc Postgraduate Merit Award (Wits University), February 2018-November 2019.
- ❖ Poster presentation certificate: CoE-SM/AMSEN annual student presentation, May 2019.
- ❖ Poster presentation certificate, 43rd SACI National Convention, December 2018.
- ❖ Poster presentation certificate, 10th Cross Faculty Symposium, September 2019.

TABLE OF CONTENTS

DECLARATION.....	I
ABSTRACT.....	II
DEDICATION.....	IV
ACKNOWLEDGEMENTS	V
PRESENTATIONS AND AWARDS	VI
TABLE OF CONTENTS	VII
LIST OF FIGURES	XIII
LIST OF TABLES	XVIII
LIST OF ABBREVIATIONS	XX
CHAPTER 1	1
1.1. Introduction: Overview of Carbon-based nanomaterials	1
1.2. Motivation	1
1.3. Aim and objectives of the study	2
1.4. Dissertation Outline.....	3
References	4
CHAPTER 2: Literature review	5
2.1. Carbon nanomaterials: History and discovery	5
2.1.1. Carbon nanofibers: Structure and morphology	6
2.1.2. Application of the carbon nanofibers	8
2.1.2.1. Catalyst and catalyst support	8
2.1.2.2. Energy storage device.....	8
2.1.2.3. Selective adsorption agents	9
2.1.2.4. Polymer composites.....	9
2.1.3. Synthesis of CNFs	10
2.1.3.1. The CVD set-up.....	10

2.1.3.2. Growth mechanism of carbon nanofibers.....	11
2.1.4. Catalysts used for the growth of CNFs.....	12
2.1.4.1. Use of nickel as a catalyst to grow CNFs.....	13
2.1.4.1.1. Unsupported Ni catalysts.....	13
2.1.4.1.2. Supported metal catalysts.....	14
2.2. Hollow carbon spheres.....	16
2.2.1. Synthesis of the HCSs.....	16
2.2.1.1. Hard templating strategy.....	16
2.2.1.2. Soft templating strategy.....	17
2.2.2. Applications of the HCSs.....	17
2.2.2.1. Catalyst support.....	18
2.2.2.2. Energy storage.....	18
2.2.2.3. Fuel cells.....	19
2.2.3. Use of the HCSs as a nanoreactor.....	19
References.....	21
CHAPTER 3: Synthesis and characterization of Ni nanoparticles encapsulated inside hollow carbon spheres.....	26
3.1. Introduction.....	26
3.2. Experimental procedure.....	27
3.2.1. Materials.....	27
3.2.2. Synthesis of polystyrene spheres (PSs).....	28
3.2.3. Loading of Ni on the polystyrene spheres (NiO/PSs).....	28
3.2.4. Synthesis of Ni inside hollow carbon sphere (NiO@HCSs).....	28
3.2.5. Loading of Ni outside HCSs (NiO/HCSs).....	29
3.2.6. Characterization techniques.....	29
3.2.6.1. Transmission electron microscopy (TEM).....	29
3.2.6.2. Scanning electron microscopy (SEM).....	29

3.2.6.3. Temperature programmed reduction (TPR)	30
3.2.6.4. Raman spectroscopy	30
3.2.6.5. Thermal gravimetric analysis (TGA)	30
3.2.6.6. Brunauer Emmet and Teller (BET) analysis	30
3.2.6.7. Powder X-ray diffraction (PXRD)	30
3.3. Results and Discussion.....	31
3.3.1. Characterization of NiO/HCSs catalyst.....	31
3.3.1.1. Morphology analysis: TEM.....	31
3.3.1.2. XRD analysis of NiO/HCSs catalyst.....	34
3.3.1.3. TPR analysis of the NiO/HCSs catalyst	35
3.3.1.4. BET analysis of HCSs and NiO/HCSs catalyst.....	36
3.3.1.5. TGA analysis of HCSs and NiO/HCSs catalyst	37
3.3.2. Characterization of NiO@HCSs catalyst	38
3.3.2.1. Morphology analysis of NiO@HCSs catalyst.....	38
3.3.2.1.1. Morphology analysis of the catalyst using a silica template	38
3.3.2.1.2. Morphology analysis of the NiO@HCSs catalyst with different Ni loading using PSs template.....	40
3.3.2.2. XRD analysis of the NiO@HCSs catalysts.....	42
3.3.2.3. TPR studies of the NiO@HCSs catalysts.....	43
3.3.2.4. BET analysis of the NiO@HCSs catalysts.....	45
3.3.2.5. TGA analysis of the NiO@HCSs catalysts	47
Conclusions	49
References	50
CHAPTER 4: Synthesis of CNFs over Ni/HCSs and Ni@HCSs catalysts using acetylene as a carbon source	53
4.1. Introduction	53
4.2. Experimental Procedure	54
4.2.1. Synthesis of NiO/HCSs or NiO@HCSs catalyst.....	54

4.2.2. Synthesis of CNFs using NiO/HCSs or NiO@HCSs catalyst.....	54
4.2.3. Determination of carbon yield.....	55
4.2.4. Characterization techniques.....	55
4.3. Results and discussion.....	56
4.3.1. Characterization of CNFs using a NiO/HCSs catalyst: TEM and XRD analysis of the synthesized CNFs	56
4.3.2. Characterization of CNFs grown over NiO@HCSs catalyst.....	57
4.3.2.1. Synthesis of CNFs over NiO@HCSs catalyst: Effect of metal loading on CNFs growth.....	57
4.3.2.2. Synthesis of CNFs over 0.5 wt% NiO@HCSs catalyst: Effect of growth temperature	60
4.3.2.2.1. Morphology analysis: TEM of CNFs grown at different reaction temperatures	60
4.3.2.2.2. XRD of CNFs grown at different reaction temperatures.....	62
4.3.2.2.3. Raman analysis of CNFs grown at different reaction temperatures.....	63
4.3.2.2.4. TGA analysis of CNFs grown at different reaction temperatures	64
4.3.2.3. Synthesis of CNFs over NiO@HCSs catalyst: Effect of H ₂ flow rate	66
4.3.2.3.1. TEM analysis of CNFs grown at different H ₂ flow rates	67
4.3.2.3.2. Raman analysis of CNFs synthesized at different H ₂ flow rates.....	69
4.3.2.3.3. TGA analysis of CNFs synthesized at different H ₂ flow rates.....	70
4.3.2.4. Synthesis of CNFs over NiO@HCSs catalyst: Effect of reaction time.....	72
4.3.2.4.1. TEM analysis of CNFs synthesized at different reaction times	72
4.3.2.4.2. Raman analysis of CNFs synthesized at different reaction times	74
4.3.2.4.3. TGA analysis of CNFs synthesized at different reaction times.....	75
Conclusions	77
References	78
CHAPTER 5: Synthesis of carbon nanofibers over NiO@HCSs catalyst using trichloroethylene as a carbon precursor.	79

5.1. Introduction	79
5.2. Experimental Procedure	80
5.2.1. Synthesis NiO@HCSs catalyst.....	80
5.2.2. Synthesis of CNFs using 0.5 wt% NiO@HCSs catalyst	80
5.2.3. Determination of the carbon yield	81
5.2.4. Characterization techniques.....	81
5.3. Results and discussion.....	82
5.3.1. Synthesis of CNFs using 0.5 wt% NiO@HCSs catalysts (nickel acetate hexahydrate precursor).	82
5.3.1.1. The influence of reaction temperature on CNFs growth.	82
5.3.1.1.1. Morphology analysis: TEM analysis	82
5.3.1.1.2. Raman analysis of CNFs synthesized at different growth temperatures.....	84
5.3.1.1.3. Thermal gravimetric analysis (TGA) analysis of CNFs grown at different reaction temperatures.....	86
5.3.1.2. The influence of H ₂ flow rate on the synthesis of CNFs using TCE.....	88
5.3.1.2.1. TEM analysis of CNFs grown at different H ₂ flow rates	88
5.3.1.2.2. Raman analysis of CNFs grown at different H ₂ flow rates.	91
5.3.1.2.3. TGA analysis of CNFs grown at different H ₂ flow rates.	93
5.3.1.3. The influence of reaction time on the synthesis of CNFs.....	95
5.3.1.3.1. TEM analysis of CNFs synthesized at different reaction times.	95
5.3.1.3.2. Raman analysis of CNFs synthesized at different reaction times.	97
5.3.1.3.3. TGA analysis of CNFs synthesized at different reaction times using TCE.	98
5.3.2. Synthesis of CNFs using different Ni precursors.	101
5.3.2.1. Characterization of NiO@HCSs catalyst using different Ni precursors	101
5.3.2.1.1. Morphology analysis: TEM analysis of NiO@HCSs catalysts synthesized using different Ni precursors.	101
5.3.2.1.2. Structural analysis: XRD analysis of CNFs synthesized using different Ni precursor	102

5.3.2.2. Synthesis of CNFs synthesized using different Ni precursors	103
5.3.2.2.1. Morphology analysis of CNFs synthesized using different Ni precursor: TEM analysis.	103
5.3.2.2.2. Raman analysis of CNFs synthesized using different Ni precursors.....	105
5.3.2.2.3. TGA analysis of CNFs synthesized using different Ni precursors.....	106
Conclusions	108
References	110
CHAPTER 6: General conclusions and recommendations	112
6.1. Conclusions	112
6.2. Recommendations	114
Supplementary Information	116
Appendix A	116
Appendix B	117
Appendix C	118

LIST OF FIGURES

Chapter 2

Figure 2. 1: Structural representation of carbon allotropes [2].	5
Figure 2. 2: Structural forms of carbon nanofibers classified by the arrangement of graphene sheets with respect to the filament axis [16].	7
Figure 2. 3: TEM images of carbon nanofibers grown from a Cu catalyst showing a variety of morphologies. (a) Helical fiber. (b) Straight fiber. (c) Fibonacci- like fiber. (d) Spring-like fiber. (e) Intertwined helical fiber. (f) Curled fiber [50].	7
Figure 2. 4: Schematic representation of a horizontal CVD set-up.	11
Figure 2. 5: Animated representations of the growth mechanisms of carbon nanofibers. (a) root-growth. (b) tip-growth.	12
Figure 2. 6: TEM images of CNFs synthesized using (a) C_2H_2 , (b) C_2H_2/TCE [26] (c) HC�NFs along with planar CNFs with a yield of ~90% and ~10% respectively (d) reveals that HC�NF grown from the polygonal Ni nanoparticle (indicated by arrow) [48] and (e) SEM image of linear CNFs synthesized by CCVD at 660 °C for 3 min using Ni particles when the gas flow rate of C_2H_2 , H_2 , and N_2 was 20, 60 and 140 mL/min, respectively [45].	14
Figure 2. 7: TEM image of CNFs prepared from different catalyst supports (a) Cu/MgO [42], (b) Cu@SiO ₂ and (c) Cu/SiO ₂ [37].	15
Figure 2. 8: The preparation and analysis of HCSs. (a) Schematic representation of HCSs synthesis. (b) SEM and TEM images of HCSs [55].	17
Figure 2. 9: TEM images of CNFs synthesized from CuO@HCSs catalyst as confirmed by tilting experiments. Image a-e show helix movement in a HCS as the tilting angle is varied, a) -60° b) -30° c) 0° d) +30° e) +60° [69].	20

Chapter 3

Figure 3. 1: TEM micrographs of PSs (a-b) and HCSs (c-d) and their corresponding particle size distribution curves, respectively.	32
Figure 3. 2: TEM images of NiO/HCSs (a-b) and NiO/HCSs_annealed (c-d) and their corresponding particle distribution curves.	33

Figure 3. 3: TEM images of tubular-structures formed as a result of annealing at high magnification.	33
Figure 3. 4: XRD patterns of HCSs, NiO/HCSs, and NiO/HCSs_annealed.....	34
Figure 3. 5: TPR profile of NiO/HCSs catalyst.	36
Figure 3. 6: Typical N ₂ adsorption-desorption of (a, b) HCSs and (c, d) NiO/HCSs and their corresponding pore size distribution curves.	37
Figure 3. 7: Shows percentage weight loss of as-prepared materials as a function of temperature, (a) TGA and (b) DTG profiles of HCSs and NiO/HCSs catalyst.....	38
Figure 3. 8: SEM images of (a) pristine silica, (b) NiO@SiO ₂ , (c) SiO ₂ @NiO@SiO ₂ , (d) HCSs, (e) NiO@HCSs-1 and (f) NiO@HCSs-2.....	39
Figure 3. 9: Schematic representation of the synthesis of NiO@HCSs catalyst.	40
Figure 3. 10: TEM images of (a) 10 wt% _trial, (b) 10 wt%, (c) 5 wt% and (d) 0.5 wt% NiO@HCSs catalysts.....	41
Figure 3. 11: XRD patterns of 0.5 wt%, 5 wt%, and 10 wt% NiO@HCSs catalysts.	43
Figure 3. 12: TPR profiles of 5 wt% and 10 wt% NiO@HCSs catalysts.....	44
Figure 3. 13: N ₂ adsorption-desorption isotherms of (a) 0.5 wt%, (b) 5 wt% and (c) 10 wt% NiO@HCSs catalysts.....	45
Figure 3. 14: Pore size distribution curves of (a) 0.5 wt%, (b) 5 wt% and (c) 10 wt% NiO@HCSs catalysts.....	46
Figure 3. 15: Shows percentage weight loss of NiO@HCSs catalyst. (a) TGA plots of 0.5 wt%, 5 wt% and 10 wt% NiO@HCSs and (b) DTG plots of 0.5%, 5 wt% and 10 wt% NiO@HCSs.	48

Chapter 4

Figure 4. 1: CVD set-up for the synthesis of CNFs using acetylene as a carbon source.....	55
Figure 4. 2: TEM images of CNFs using acetylene over NiO/HCSs (a-d) (synthesized at 450 °C, H ₂ /C ₂ H ₂ =100 mL/min) and XRD pattern of CNFs.	57
Figure 4. 3: TEM images of CNFs using acetylene over NiO@HCSs catalyst, (a) CNF_10 wt%, (b) CNF_5 wt%, and (c) CNF_0.5 wt% (synthesized at 450 °C, H ₂ /C ₂ H ₂ =100 mL/min, 5 min).....	58
Figure 4. 4: High magnification TEM images of CNFs grown from 0.5 wt% NiO@HCSs catalyst (450 °C, H ₂ /C ₂ H ₂ =100 mL/min, 5 min).....	59

Figure 4. 5: TEM tilting experiment micrographs showing the helix movement in a HCSs nanoreactor, (a) -45° (b) -30° (c) 0° (d) +30° and (e) +55° .	59
Figure 4. 6: TEM images of CNFs using acetylene over 0.5 wt% NiO@HCSs catalyst at (a) CNF_250, (b) CNF_300 and (c) CNF_350 (H ₂ /C ₂ H ₂ = 100 mL/min, 5 min).	60
Figure 4. 7: TEM images of CNFs using acetylene over 0.5% Ni@HCSs catalyst at (a) CNF_450, (b) CNF_500 and (c) CNF_600 (H ₂ /C ₂ H ₂ =100 mL/min, 5 min).	61
Figure 4. 8: Graph showing % yield of CNFs as the reaction temperature increased.	62
Figure 4. 9: XRD patterns of CNFs grown at different temperatures (reaction conditions: H ₂ /C ₂ H ₂ = 100 mL/min, 5 min).	63
Figure 4. 10: Raman spectra of CNFs grown at different temperatures (H ₂ /C ₂ H ₂ (100 mL/min, 5 min).	64
Figure 4. 11: TGA plots of CNFs synthesized at different temperatures (H ₂ /C ₂ H ₂ (100 mL/min, 5 min).	65
Figure 4. 12: DTG plots of CNFs synthesized at different temperatures (H ₂ /C ₂ H ₂ =100 mL/min, 5 min).	66
Figure 4. 13: TEM images of CNFs synthesized at different H ₂ flow rate, (a) CNF_20, (b) CNF_50, (c) CNF_80, (d) CNF_100 (inset; HRTEM image showing clearly the mono-directional growth of CNF from a single nickel particle) and (e) CNF_120 mL/min.	68
Figure 4. 14: Plot of carbon % yield obtained at different H ₂ flow rates.	69
Figure 4. 15: Raman spectra of CNFs synthesized at different H ₂ flow rates.	70
Figure 4. 16: TGA plots of CNFs synthesized at different H ₂ flow rates.	71
Figure 4. 17: CNFs synthesized at different H ₂ flow rates.	71
Figure 4. 18: TEM images of CNFs synthesized at reaction time, (a) CNF_5, (b) CNF_15, (c) CNF_30, (d) CNF_60 and (e) CNF_90 min.	73
Figure 4. 19: Statistical plot of CNFs synthesized at different reaction times. A direct relationship between the % yield and reaction time was observed.	74
Figure 4. 20: Raman spectra of CNFs synthesized at different reaction times.	74
Figure 4. 21: TGA plots of CNFs synthesized at different reaction times.	75
Figure 4. 22: TGA plots of CNFs synthesized at different reaction times.	76

Chapter 5

Figure 5. 1: CVD set-up for the synthesis of CNFs using TCE as a carbon source.	81
--	----

Figure 5. 2: TEM images of CNFs using TCE over 0.5 wt% NiO@HCSs catalyst at (a) TCE _350, (b) TCE _450 (inset, HRTEM showing monomodal growth of CNFs with irregular morphology), (c) TCE _500 and (d) TCE_600.....	83
Figure 5. 3: Graph showing % yield of CNFs as the reaction temperature increases.....	84
Figure 5. 4: Raman plots of CNFs synthesized at different temperatures.	85
Figure 5. 5: TGA plots of CNFs synthesized at different temperatures.	86
Figure 5. 6: DTG plots of CNFs synthesized at different temperatures.	87
Figure 5. 7: TEM images of Ni catalysts; (a), (b) TCE deposited in the absence of H ₂ and (c), (d) TCE deposited in the absence of N ₂ (synthesized at 450 °C for 5 min).....	89
Figure 5. 8: TEM images of CNFs synthesized at different H ₂ flow rate, (a) TCE _20, (b) TCE _50, (c) TCE _80, (d) TCE _100 and (e) TCE _120 mL/min.....	90
Figure 5. 9: Statistical plot of CNFs synthesized at different H ₂ flow rates.	91
Figure 5. 10: Raman spectra of CNFs synthesized at different H ₂ flow rate, TCE_20, TCE_50, TCE_ 80, TCE_100 and TCE_120 mL/min (synthesized at T= 450 °C, for 5 min).	92
Figure 5. 11: TGA plots of CNFs synthesized at the different H ₂ flow rate (T= 450 °C, growth time 5 min).....	93
Figure 5. 12: TGA plots of CNFs synthesized at different H ₂ flow rates (T= 450 °C, growth time 5 min).....	94
Figure 5. 13: TEM images of CNFs synthesized at reaction time, (a) TCE _5, (b) TCE _15, (c) TCE _30, (d) TCE _60 and (e) TCE _90 min.....	96
Figure 5. 14: Statistical plot of CNFs synthesized at different reaction times. A direct relationship between the % carbon yield and CNFs growth time was observed.....	97
Figure 5. 15: Raman spectra of CNFs synthesized at different reaction times (synthesized at T= 450 °C, H ₂ /N ₂ flow rate =100 mL/min).	98
Figure 5. 16: TGA plots of CNFs synthesized at different reaction times (T= 450°C, H ₂ /N ₂ flow rate of 100 mL/min).....	99
Figure 5. 17: DTG plots of CNFs synthesized at different reaction times (T= 450°C, H ₂ /N ₂ flow rate of 100 mL/min).....	100
Figure 5. 18: TEM images of (a) Ni_nit, (b) Ni_chl and (c) Ni_ace catalysts	102
Figure 5. 19: XRD spectra of Ni_chl, Ni_nit and Ni_ace catalysts.....	103
Figure 5. 20: TEM images of TCE_chl, TCE_nit, and TCE_ace, showing CNFs with a monomodal growth (synthesized at 450 °C, H ₂ /N ₂ = 100 mL/min, for 5 min).	104
Figure 5. 21: TEM image of CNFs with a hollow central core.	105

Figure 5. 22: Raman spectra of TCE_chl, TCE_nit, and TCE_ace (synthesized at 450 °C, H ₂ /N ₂ = 100 mL/min, for 5 min).....	106
Figure 5. 23: TGA profiles of CNFs synthesized from different Ni compounds (synthesized at 450 °C, H ₂ /N ₂ = 100 mL/min, for 5 min).....	107
Figure 5. 24: DTG profiles of CNFs synthesized from different Ni compounds (synthesized at 450 °C, H ₂ /N ₂ = 100 mL/min, for 5 min).....	108

Chapter 6

Figure 6. 1: TEM images of CNFs synthesized using different carbon precursors, Acetylene (a, b) and TCE (c, d) synthesized at 450 °C and 600 °C.....	114
---	-----

Supplementary Information

Appendix A

Figure S3. 1: TEM image of Ni@HCSs-1.....	116
Figure S3. 2: TGA profiles (a) and derivative curves (b) of the HCSs and NiO@HCSs catalysts synthesized using silica template.	116

Appendix B

Figure S4. 1: EDS spectra of CNFs synthesized at 450 °C for 5 min using acetylene as a carbon source.	117
---	-----

Appendix C

Figure S5. 1: EDS spectra of CNFs synthesized at 450 °C for 5 min using TCE as a carbon source.	118
Figure S5. 2: N ₂ adsorption-desorption and corresponding pore size distribution curves of NiO@HCSs catalysts (a, b) Ni_nit; (c, d) Ni_ace and (e, f) Ni_chl.....	119
Figure S5. 3: TPR profiles of NiO@HCSs catalysts prepared from different nickel compounds.	120

LIST OF TABLES

Chapter 3

Table 3. 1: Textural properties of the as-synthesized HCSs and NiO/HCSs catalyst.....	36
Table 3. 2: Calculated particle sizes of the HCSs (shell thickness and inner diameter) and Ni nanoparticles	42
Table 3. 3: Textural properties of the as-synthesized NiO@HCSs catalysts.....	47
Table 3. 4: Summarizes the decomposition temperature of NiO@HCSs catalysts	48

Chapter 4

Table 4. 1: The I_D/I_G ratios of D and G peaks of the obtained CNFs	64
Table 4. 2: Summarizes decomposition temperature of CNFs at different temperatures	66
Table 4. 3: Summary of the Raman data of the obtained CNFs.....	70
Table 4. 4: Summarizes maximum decomposition temperatures of CNFs at different H ₂ flow rates	72
Table 4. 5: Summary of the Raman data of the obtained CNFs.....	75
Table 4. 6: Summarizes maximum decomposition temperatures of CNFs at different time intervals.....	77

Chapter 5

Table 5. 1: The I_D/I_G ratios of D and G peaks of the obtained CNFs	85
Table 5. 2: Summarizes the decomposition temperature of CNFs synthesized at different temperatures.....	88
Table 5. 3: The I_D/I_G ratios of D and G peaks of the obtained CNFs	92
Table 5. 4: Summarizes maximum decomposition temperatures of CNFs at different H ₂ flow rates	94
Table 5. 5: The I_D/I_G ratios of D and G peaks of the obtained CNFs	98
Table 5. 6: Summarizes maximum decomposition temperatures of CNFs at different time intervals.....	100

Table 5. 7: The I_D/I_G ratios of D and G peaks of the CNFs prepared from different Ni compounds 106

Table 5. 8: Summarizes maximum decomposition temperatures of the as-prepared CNFs . 108

Supplementary Information

Appendix A

Table S3. 1: Surface area data of HCSs and NiO@HCSs catalysts synthesized using silica template..... 117

LIST OF ABBREVIATIONS

Abbreviation	Definition
BET	Brunauer-Emmet and Teller
C ₂ H ₂	Acetylene
CNFs	Carbon nanofibers
CNTs	Carbon nanotubes
CVD	Chemical vapour deposition
DTG	Differential thermal gravimetric
EDS	Energy dispersive X-ray spectroscopy
fcc	Face centered cubic structure
HCSs	Hollow carbon spheres
HDP	Homogeneous deposition precipitation
HF	Hydrofluoric acid
NiO	Nickel oxide nanoparticles
NiO/HCSs	Nickel oxide outside hollow carbon spheres
NiO@HCSs	Nickel oxide inside hollow carbon spheres
NPs	Nanoparticles
PSs	Polystyrene spheres
PXRD	Powder X-ray diffraction
RF	Resorcinol formaldehyde
SEM	Scanning electron microscopy
SERS	Surface enhanced Raman-scattering
TCE	Trichloroethylene

TEM	Transmission electron microscopy
TGA	Thermal gravimetric analysis
TPR	Temperature programmed reduction
wt%	Weight percentage

CHAPTER 1

1.1. Introduction: Overview of Carbon-based nanomaterials

The synthesis and application of carbon-based materials history date back to the discovery of carbon black fabricated from the combustion of fuels which were used to make inks and tattoos [1]. Recently, carbon nanomaterials have been recognised as one of the core components of nanotechnology due to their inherent quantum size and shape effects which give them a wide potential of applications in many fields. Carbon allotropes' such as graphene, diamond, and carbon nanotubes (CNTs) has made carbon technology become a forefront area in the entire field of nanotechnology [2-4]. Various synthetic routes have been developed for the production of these carbonaceous materials. Among the existing methods, the catalytic chemical vapour deposition technique (CCVD) is the commonly used method for their synthesis; it has great advantages over the other methods because it is cheap, simple to operate and also produces high purity products [3-6]. Also, the method offers advantages such as the ability to vary reaction parameters that can affect the morphology, particle size and yield of products.

1.2. Motivation

Globally there is an intense interest in developing a new class of materials with exceptional properties which can render a wide variety of potential applications in many fields. Recently, carbon-based nanomaterials have attracted increasing attention in research laboratories owing to their fascinating properties and noteworthy applications [1, 10, 13]. Among the well-known carbon nanomaterials, filamentous carbon materials commonly known as carbon nanofibers (CNFs) are one of the most studied nanomaterials [9]. Initially, these materials were reported to be grown from carbon-containing gases using metallic crucibles and their presence was considered a nuisance. Thus, their production was not considered important in the early years. However, the recent outburst of renaissance in these materials originates from their unique structural and electrical properties similar to those of CNTs such as having a high specific surface area, flexibility, high mechanical and electrical conductivity and strength [4]. These properties have made CNFs to be ideal candidates in research and useful material in established commercial applications e.g. in water treatment as an adsorbent, in catalysis as a support material for catalysts, in energy storage devices as a cathode material and a reinforcing material

in polymeric composites e.g. CFRP material used in aerospace, bicycle frames, and automobiles [10-12].

In general, the growth of CNFs involves the decomposition of a volatile hydrocarbon over the surface of a nano-sized metal particle, which is normally a transition metal such as Cu, Fe, Ni, Co catalysts [9-11]. For CNFs synthesized using the CVD method, the size of the metal nanoparticle plays a vital role in determining the size and shape of the CNFs grown [10, 13]. CNFs have been previously grown on both unsupported and supported metal nanoparticles. Typical supports studied include traditional supports such as silica, titania, and alumina. The issue faced with growing CNFs on unsupported metal nanoparticles is that at elevated temperatures, the metal nanoparticles readily agglomerate forming large particles and this affects the size and shape of the CNFs formed. Also, metal agglomeration still prevails on traditional supports due to weak metal-support interactions. Consequently, this affects the morphology of the catalytically grown CNFs and the CNFs grown can grow to be very long lengths. One process that could mitigate the metal sintering and control the CNF length is to ‘encapsulate’ both the catalyst and the CNFs. This could be achieved by encapsulating them inside a hollow sphere e.g. a ship-in-a-bottle strategy. Thus, numerous questions arise: *Can the encapsulation of metal nanoparticles inside a hollow sphere e.g. hollow carbon spheres (HCSs) minimize metal sintering at high temperatures and improve their catalytic activity? Is it possible to build structures such as CNFs and CNTs inside the hollow carbon spheres (HCSs)? Can different structures of CNFs be grown inside the HCSs and can their growth be controlled inside HCSs (size, morphology, and length)?*

As such the research project tackles the issue of metal nanoparticle agglomeration at high temperatures and opens a new window to synthesize carbon structures at the nano level using HCSs as a nano-reactor.

1.3. Aim and objectives of the study

The study aimed to synthesize Ni@HCSs catalysts and investigate the concept of using HCSs as a nanoreactor to grow carbon nanofibers. This will provide information to understand the processes that govern the CNFs growth and their control. The aim will be achieved by accomplishing the following objectives:

- ❖ Synthesize and characterize pristine polystyrene spheres (PSs), Ni/PSs, Ni/PSs@C, and HCSs.

- ❖ Synthesize and characterize Ni catalysts supported outside/inside hollow carbon spheres (Ni/HCSs and Ni@HCSs, respectively) by the CVD method using nitrogen as a carrier gas. The effect of temperature and flow rate will be studied.
- ❖ Synthesize and characterize CNFs grown from a Ni/HCSs and Ni@HCSs catalysts using a CVD reactor and acetylene as the carbon source and hydrogen.
- ❖ Study the effect of reaction parameters such as temperature, growth time, carrier gases (N₂ or Ar) and flow rate to obtain optimum growth conditions of CNFs from Ni. The effect of using different Ni compounds for CNF growth was to be evaluated.
- ❖ Characterize the as-synthesized materials using techniques that include, Thermogravimetric Analysis (TGA), Brunauer-Emmet and Teller (BET) analysis, Power X-ray Diffraction, Transmission Electron Microscopy (TEM) and Raman Spectroscopy.

1.4. Dissertation Outline

Chapter 1: Gives an overview of the research to be performed and its importance. It also outlines the motivation of the study, aims, and objectives.

Chapter 2: This chapter presents a detailed background associated with carbon nanostructures (CNFs and HCSs), their synthesis, properties, and applications. It also gives literature associated with the use of Ni nanoparticles as potential catalysts for the synthesis of CNFs.

Chapter 3: This chapter discusses the synthesis and characterization of Ni nanoparticles supported outside/inside hollow carbon spheres.

Chapter 4: This chapter provides the synthesis of helical CNFs formed over Ni/HCSs and Ni@HCSs catalysts using acetylene as a carbon source.

Chapter 5: This chapter describes the synthesis of CNFs formed over supported Ni catalysts using trichloroethylene as a carbon precursor. A brief study of the effect of using different nickel compounds for the synthesis of CNFs is also discussed in this chapter.

Chapter 6: This chapter provides general conclusions and recommendations for the overall research conducted for future studies.

References

1. N.J. Coville, S.D. Mhlanga, E.D. Nxumalo, A. Shaikjee, *South African Journal of Science*, 107 (3/4) (2011) 1-15.
2. S. Iijima, *Nature*, 354 (1991) 56-58.
3. B.K. Mutuma, *Synthesis and characterization of Solid, Hollow, Core-shell and worm-like carbon nanostructures for Application in Organic Photovoltaic Devices and Chemical Sensors*, Ph.D. Thesis, University of the Witwatersrand, Johannesburg, (2016).
4. T.N. Phaahlamohlaka, D.O. Kumi, M.W. Dlamini, R. Forbes, L.L. Jewell, D.G. Billing, N.J. Coville, *ACS Catalysis*, 7 (2017) 1568-1578.
5. M.O. Dawood, M.A.M. Hassan, *International Journal of Nanoscience and Nanoengineering*, 1 (1) (2014) 1-7.
6. P.E. Anderson, N.M. Rodriguez, *Chemistry of Materials*, 12 (3) (2000) 823-830.
7. K.P. De Jong K.P, J.W. Geus J.W, *Catalysis Reviews-Science & Engineering*, 42 (4) (2000) 481-510.
8. G.A. Jimenez G.A, S.C. Jana S.C, *Carbon*, 45 (2007) 20179.
9. M.S. Maubane M.S, *Nickel and copper catalysed synthesis of carbon fibers*, Ph.D. Thesis, University of the Witwatersrand, Johannesburg, (2013).
10. N.M. Rodriguez N.M, *Materials Research Society*, 8 (12) (1993) 3233-3248.
11. A. Shaikjee A, N.J. Coville N.J, *Carbon*, 50 (2012) 1099-1108.
12. R. Usamentiaga R, C. Ibara-Castanedo C, M. Klein M, X. Maldague X, J. Peeters J, A. Sanchez-Beato A, *Sensors*, 17 (2017) 2679.
13. S. Bhoware S, M.S. Maubane M.S, T. Phaahlamohlaka T, A. Shaikjee A, N.J. Coville N.J, *Chemical Physics Letters*, 577 (2013) 71-75.

CHAPTER 2

Literature review

2.1. Carbon nanomaterials: History and discovery

Carbon is a marvellous and versatile element in the periodic table and one of the most abundant elements on earth [1]. Carbon has led to the evolution of many carbon nanomaterials that can show unique chemical and physical properties. Carbon forms a wide range of allotropes such as diamond, graphene, fullerenes and carbon nanotubes (CNTs) (**figure 2.1**) [1-3]. The C_{60} commonly referred to as “buckminster fullerene or buckyball” was the first fullerene to be discovered in 1985 by Kroto and coworkers [4]. This molecule is described as an enclosed spherical shaped molecule that consists of 60 carbon atoms arranged with 12 pentagonal and 20 hexagonal rings. The discovery of fullerenes, graphene, and their tubular form which was later popularized in 1991 by Iijima as CNTs, has since made carbon materials a hot topic in many research fields [3,5]. The distinct morphologies of the carbon nanomaterials are a direct consequence of the molecular bonding mode of electrons in carbon that can show different hybridization (sp , sp^2 , sp^3) states [6]. These materials made from carbon exhibit unique mechanical, thermal, electrical and magnetic properties [7, 8] which have made them ideal candidates for use in several technologies. The carbon nanomaterials have shown diverse potential applications in areas such as supercapacitors [9], medicine for cancer therapy [10] catalysis, PEM fuel cells, sensors, and also in water treatment [11, 12].

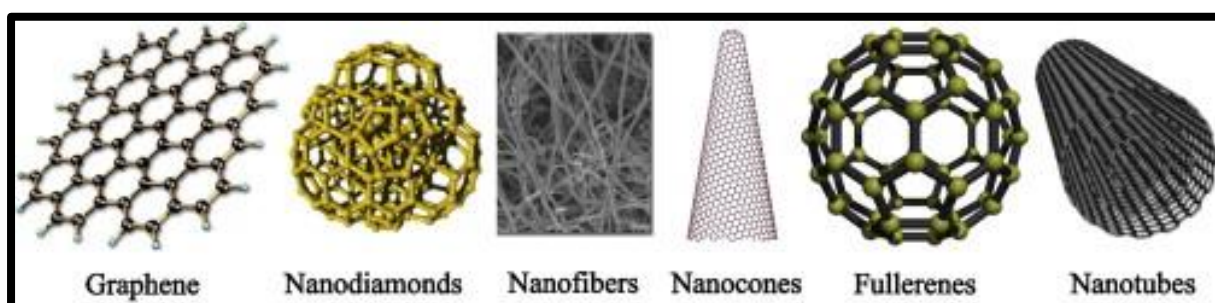


Figure 2. 1: Structural representation of carbon allotropes [2].

Among the various carbon-based nanomaterials, carbon nanofibers (CNFs) were studied decades ago. The history of CNFs dates back to 1889 [13, 14] when CNFs were reported to be

grown from carbon-containing gases using metallic crucibles as the catalyst. Robertson was among the first researchers to recognize that the interaction of methane and metal surfaces led to the formation of graphitic carbon at low temperatures [14]. Initially, these materials were referred to as carbon filaments and they often emerged as by-products during the catalytic conversion of carbon-containing gases e.g. in the Fischer Tropsch process used to produce fuels [14, 15]. The presence of CNFs created problems including blockage of reactors, catalyst deactivation due to encapsulation of the active metal component and also reduced heat transfer. Thus their production was viewed as a hindrance in the early years. However, the recent outburst of interest in these materials originates from their exceptional chemical and physical properties.

2.1.1. Carbon nanofibers: Structure and morphology

Carbon nanofibers (CNFs) belong to the carbon fiber (CF) family and are defined as a sp^2 hybridization-based, discontinuous and highly graphitic carbon material with a cylindrical shape [16]. Compared to the CF, they exhibit a diameter ranging from 3 to 100 nm and a length that can range from micrometers to a few centimeters [1, 14-16]. These materials are composed of graphene layers that are stacked upon each other and adopt different morphologies. Depending on the arrangement of the graphene layers, three main structural arrangements have been identified, namely platelet, herringbone and tubular like filaments as shown in **figure 2.2**. In a platelet form, the graphene layers are arranged perpendicular to the fibers axis, in herringbone form the layers are at an angle to the fiber axis and are parallel to the fiber axis in the tubular form [16, 17].

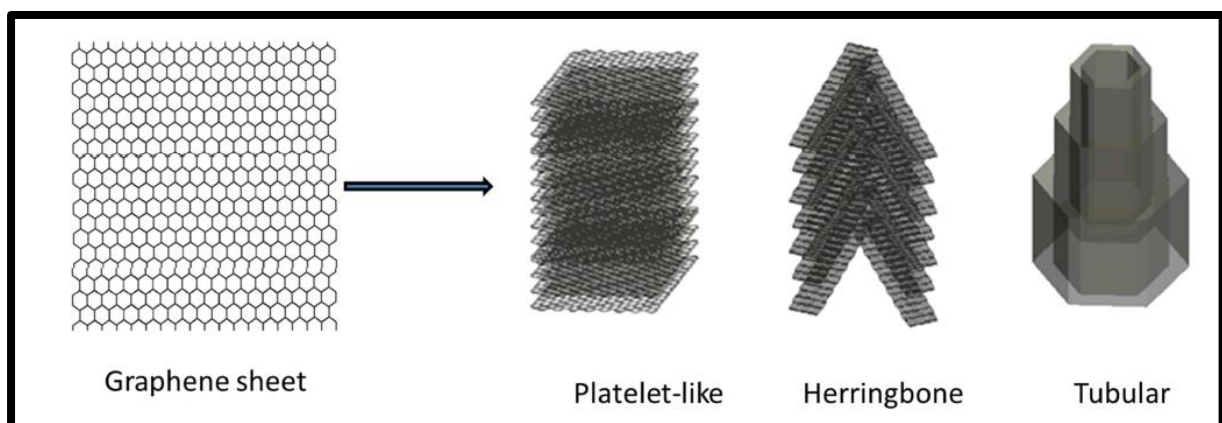


Figure 2. 2: Structural forms of carbon nanofibers classified by the arrangement of graphene sheets with respect to the filament axis [16].

CNFs can adopt a variety of conformations including helical, linear, branched, bidirectional coiled, etc. and some of these conformations are shown in **figure 2.3**. The different morphologies of CNFs have been reviewed [32, 37, 50]. The difference in the morphologies observed depends on the synthesis route used i.e. the catalyst, carbon source, temperature and the synthetic technology employed. For example, using the catalytic chemical vapour deposition (CCVD) technique, acetylene as carbon source and Cu as a catalyst, the CNFs grown can be helical in shape. The control of the morphology of carbon nanofibers remains a challenge partly due to many reaction parameters that influence their morphology. However, control over their size and shape can be achieved by using identical reaction conditions for their synthesis.

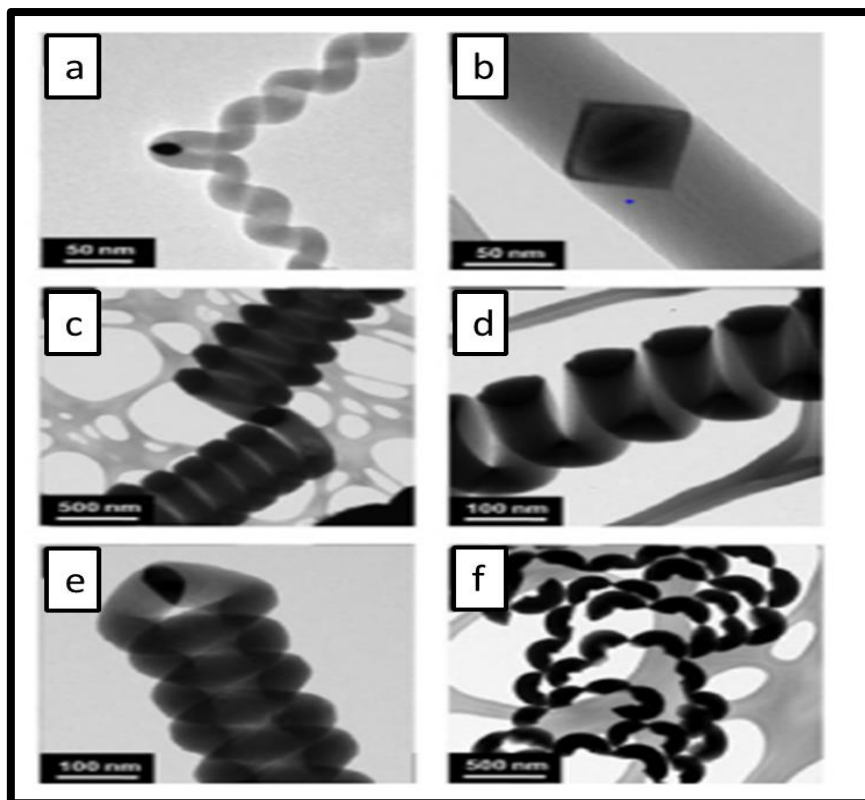


Figure 2. 3: TEM images of carbon nanofibers grown from a Cu catalyst showing a variety of morphologies. (a) Helical fiber. (b) Straight fiber. (c) Fibonacci- like fiber. (d) Spring-like fiber. (e) Intertwined helical fiber. (f) Curled fiber [50].

2.1.2. Application of the carbon nanofibers

As a result of their exceptional structural and electrical properties, such as having a high specific surface area, flexibility, high mechanical strength and electrical conductivity [60]. CNFs have been explored in a wide range of applications. CNFs have been used as a support material in catalysis [58-59]. CNFs have also been used as cathode material in energy storage devices [13, 71-72], adsorbents in water treatment [23, 78] and reinforcing fillers in polymeric composites [73-77].

2.1.2.1. Catalyst and catalyst support

Carbon nanofibers are a common support material used in heterogeneous catalysis [13]. CNFs used as a support media offer added advantages over the traditional supports such as silica and alumina due to their unique structural and electrical properties. It is believed that nanofibers form strong interactions with metal nanoparticles deposited over their surface and as a consequence, the morphology of the catalyst particle can be modified which can result in unexpected activity and selectivity patterns [23]. Salman *et al.* [70] conducted a study on the hydrogenation of crotonaldehyde to crotyl alcohol by Ni supported on different types of graphite nanofiber materials (two types; orientated differently) and compared its activity with Ni supported on γ -Al₂O₃ support under similar conditions. They found that Ni has a significant activity and good conversion when supported on graphite nanofiber materials as opposed to being supported on γ -Al₂O₃. They attributed this finding to the strong metal-support interactions of the graphite nanofiber materials with Ni nanoparticles. Toebes *et al.* [58] observed that the hydrogenation of cinnamaldehyde was enhanced as the number of oxygen-containing groups on the surface of the CNF decreased using CNF supported ruthenium catalysts. Bezemer *et al.* [59] conducted a study on cobalt nanoparticles supported on carbon nanofibers and silica using homogenous deposition precipitation under different pH conditions for Fischer-Tropsch synthesis (FTS). The catalytic tests from the study revealed that the CNF-supported catalysts modified at high pH resulted in a higher cobalt specific activity in the FTS reaction compared to their low pH modified counterparts.

2.1.2.2. Energy storage device

Carbon nanofibers have shown potential to be used as an electrode material in batteries and supercapacitors [71-72]. Particularly, in supercapacitors, the operation of the device is based on a phenomenon at the interface between an ionic conductive electrolyte and an electrically conductive high surface area electrode. The commonly used electrolyte and electrode materials

are sulphuric acid and activated carbon, respectively [23]. Although activated carbons exhibit a very high surface area ($\sim 1000 \text{ m}^2/\text{g}$), it possesses poor electrical conductivity. Therefore, catalytically grown CNFs have been used as a replacement material for the activated carbon due to their equivalent high surface area ($\sim 700 \text{ m}^2/\text{g}$, when activated) and high electrical conductivity, which improves the performance of the supercapacitors [13].

Barranco *et al.* [71] reported on the use of amorphous CNFs activated in KOH as electrode material in supercapacitors. They observed that the performance of amorphous CNFs was superior to that of activated carbon and this aspect was related to their high electrical conductivity and relatively high surface area. Zhou *et al.* [72] obtained a high specific capacity of 263.7 F g^{-1} at a discharge current density of 100 mA g^{-1} and very good cycling stability of energy storage with a retention ratio of 86.9% after 200 cycles using graphene beaded carbon nanofibers (G/CNF).

2.1.2.3. Selective adsorption agents

CNFs have been exploited as a suitable adsorbent in liquid phase reactions systems as they provide improved transport properties and excellent mechanical properties over those found with conventional adsorbents [23]. Moreover, the pore structure of CNFs is ideal for the rapid adsorption/desorption of large amounts of gases. Raghubanshi *et al.* [48] investigated and reported that as-synthesized helical CNFs, mixed with NaAlH_4 , enhanced the hydrogen desorption kinetics by 5 times compared to using pristine NaAlH_4 complex. Lekota *et al.* [78] reported on the extraction and preconcentration of carbamazepine (CBZ) from wastewater using carbon nanofiber coated with magnesium oxide-zinc oxide (MgO-ZnO-CNFs) composite. They found that MgO-ZnO-CNFs composite an adsorbent material resulted in low LOD, high preconcentration factor, low sample consumption and excellent recoveries (ranging from 97.8 to 102%) with high accuracy and precision.

2.1.2.4. Polymer composites

Carbon fibers have been utilised as a composite reinforcement material [74-75]. For fibers to be considered as a reinforcement material, their diameters should be small as this affects the fiber strength. As such, catalytically grown CNFs have been used in polymer composites as a result of their small diameters compared to other carbon fibers. One of the most commonly known carbon fiber composites with vast application in industry is the carbon fiber reinforced polymer (CFRP), which consists of a continuous polymer matrix reinforced by carbon fiber [73, 77]. These polymers lead to a high-performance material allowing weight reduction

compared to the conventional metals (steel, titanium, and aluminium). Carbon fiber reinforced composites have low densities, excellent strength and stiffness, high corrosion and chemical resistance [76]. CFRP is used in aerospace, automobile, civil engineering and sports goods such as CFRP bicycle frames, which have become a performance material in the cycling world [60, 74-75].

2.1.3. Synthesis of CNFs

Despite their broad applications, the synthesis of CNFs remains a crucial factor in the CNFs science and nanotechnology field as their synthesis impacts on their application [28]. Thus, attempts have been made to produce CNFs with a well-known structure and in good yield. CNFs have been synthesized through three main documented synthetic routes and these are the arc discharge, laser ablation, and chemical vapour deposition (CVD) methods [14-25]. These reported methods have been extensively used to synthesize carbon nanomaterials. However, the arc-discharge and laser ablation have rarely been used as these methods usually require a high reaction temperature and are costly (energy-intensive) and only give a low yield of carbon nanomaterials [18]. Thus, the CVD method is the most frequently used method for the growth of CNFs as it allows large scale manufacturing of the carbon nanomaterials.

2.1.3.1. The CVD set-up

The CVD method requires a carbon precursor and a metal catalyst (supported or unsupported) to produce carbon nanomaterials. Most CVD reactions are normally performed in a horizontal furnace as depicted in **figure 2.4**. The furnace can also be arranged in a vertical position, where the carbon source is injected at the top or bottom of the quartz tube [14, 24-25]. In a typical CVD set-up, the reactor comprises a quartz tube inserted in a hot oven (heated to the desired reaction temperature) and a catalyst placed at the center of the quartz tube. The carbon source is then passed through the quartz tube using an appropriate carrier gas. The carbon source then decomposes on the surface of a reactive species to produce the desired product.

The advantages of this method, compared to conventional methods, is that this method provides enhanced versatility in the array of materials that can be obtained and a large number of parameters such as reaction time, temperature, flow rate, etc. can be varied and investigated during CNF growth [24, 26]. The method also provides ease of production on a large scale (even for industrial use) and products are highly pure and reproducible. Moreover, this method allows control of the carbon nanomaterial morphology and structure through tuning of the

catalyst composition in conjunction with the carbon-containing gas and reaction parameters [31].

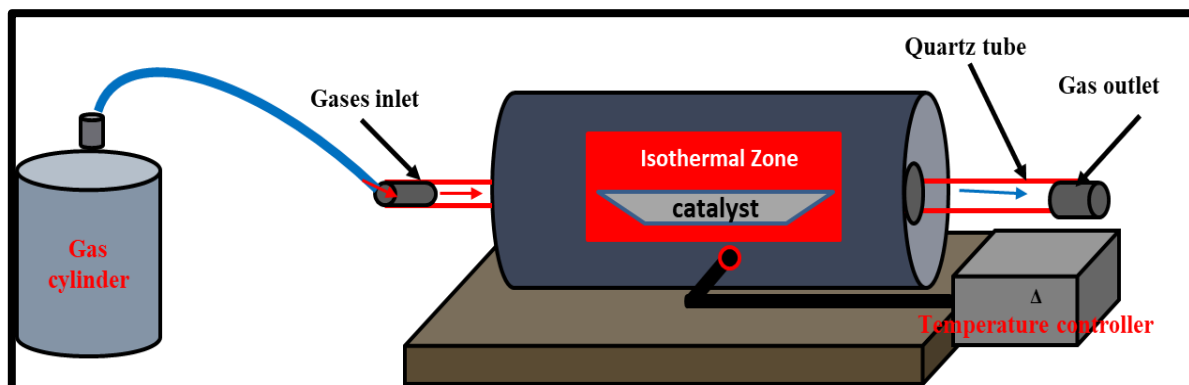


Figure 2. 4: Schematic representation of a horizontal CVD set-up.

2.1.3.2. Growth mechanism of carbon nanofibers

Carbon nanofibers are formed by the catalytic decomposition of hydrocarbons over a metal surface. The commonly used carbon precursors in this method include methane, acetylene, ethylene, carbon monoxide, toluene and short-chain alcohols [14, 24, 28, 33]. Two major growth mechanisms have been proposed in the literature for the synthesis of CNFs [13-14, 23, 29]. These are namely; a root-growth and a tip-growth mechanism [6-7, 30]. These mechanisms are distinguished by the way the metal interacts with the support material. The root-growth mechanism is observed when there is a strong metal-support interaction whereas a weak metal-support interaction results in tip-growth as illustrated in **figure 2.5**. Additionally, if there exists a very weak metal-support interaction, the catalyst may break from the support and growth may occur in both directions. It is believed that both these mechanisms can occur simultaneously since all interactions can coexist within the same catalyst.

In all the described mechanisms, the formation of CNFs involves adsorption of a hydrocarbon such as methane, onto a nanosized metal particle surface at high temperature and this leads to C-H bond breakage. These carbon atoms that are formed over the catalyst surface form metal carbides. The carbon can dissolve and diffuse through the bulk of the metal resulting in precipitation of carbon as a CNF. Typically but not always, the growth of the fiber occurs on only one side of the nanoparticle.

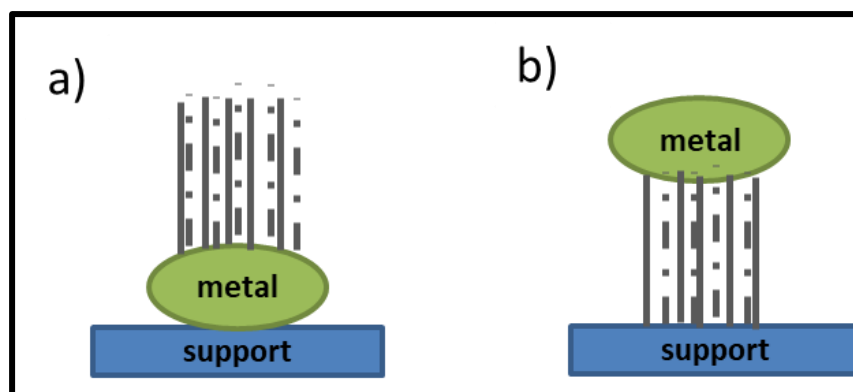


Figure 2. 5: Animated representations of the growth mechanisms of carbon nanofibers. (a) root-growth. (b) tip-growth.

Baker *et al.* [30] proposed that the mechanism of CNF formation on an unsupported catalyst is similar to that on a support. This involves firstly, the adsorption of the hydrocarbon and then the dissociation into carbon species over the surface of the metal catalyst and its dissolution into the catalyst particle [32]. One or more fiber can grow from the metal particle.

2.1.4. Catalysts used for the growth of CNFs

The growth of CNFs has been reported to be catalysed by traditional transition metals such as Ni [35], Fe [19], Cu [34], Co [46] catalysts and their alloys [27, 37-38]. These metals have been used as both bulk particles (size typically 100 nm) and supported particles (10-50 nm). The interaction of metals, either as a nanoparticle or a single crystal with a small hydrocarbon (e.g. CH₄, C₂H₂) have been studied to improve the performance of the catalyst. Early studies conducted by Motojima *et al.* [36] revealed that the addition of small amounts of thiophene as an impurity in a Ni-catalysed pyrolysis of acetylene resulted in the formation of carbon microcoils at temperatures between 350-750 °C. They observed that the carbon coils grew perpendicularly, pointing in the direction of the source gas inlet. Nitze *et al.* [21] demonstrated the growth of carbon nanotubes and helical carbon nanofibers by chemical vapour deposition on C₆₀ fullerene Pd nanoparticles at 550–800 °C.

Shaikjee *et al.* [27] reported that CNFs grown from a Cu catalyst could show symmetric growth of two carbon filaments from one metal nanoparticle (NP) whereas other metals showed fiber growth in one direction.

Herein, the synthesis of CNFs was undertaken using a Ni catalyst. Nickel is a well-established metal for the growth of carbon nanomaterials; it is cheap, abundant and can give growth of two or more carbon strands [26].

2.1.4.1. Use of nickel as a catalyst to grow CNFs

The ability of nickel metal/nanoparticle to catalyze the formation of carbon nanofibers has been reported in the literature [26, 35-36, 41, 45]. Studies have shown that carbon nanofibers can be grown from different nickel catalysts systems; for example, nickel foam [41], pure Ni powder, unsupported (alloys or bulk Ni particle) and supported Ni nanoparticles [26, 36, 79]. Some of the studies where Ni was used to grow CNFs are illustrated in **figure 2.6**.

2.1.4.1.1. Unsupported Ni catalysts

The preparation of coiled carbon fibers using a Ni catalyst was reported by Motojima *et al.* [39]. The coiled carbon fibers were prepared by pyrolysis of acetylene using a Ni catalyst and small amounts of impurities (sulfur or phosphorus compounds at 600-800 °C).

Chen *et al.* [41] reported on the preparation of carbon microcoils (CMC) by the catalytic decomposition of acetylene at 973-1073K on commercial nickel foam. They observed that there was a reconstruction of Ni grains from spherical to rhombohedral shape during CMC growth and no CMCs were formed without the sulfur promoter.

Studies by Jian *et al.* [45] revealed the formation of straight carbon nanofibers and three kinds of carbon coils (single-helix, carbon nanocoils, single-helix carbon microcoils and twinning double-helix carbon microcoils) with coil diameters ranging from 150 nm to 3 µm using Ni nanoparticles (depicted in **figure 26e**).

Chen *et al.* [35] reported on the formation of circular and flat carbon coils during the pyrolysis of acetylene over a Ni catalyst at 750 °C. They found that during the early growth stage, the circular coils formed and as the reaction progressed, the flat coils started forming. They ascribed this to the change in catalyst shape from a cubic to a slender form.

Preparations of CNFs by alloy-catalysed decomposition of hydrocarbons have also been studied. Yu *et al.* [44] prepared coiled carbon nanofibers by pyrolysis of acetylene over Cu-Ni alloy nanoparticles prepared by a hydrogen-arc plasma method. They observed the formation of coiled fibers at a low temperature of 241 °C.

More recently, Maubane and co-workers [26] reported on the synthesis of carbon nanofibers on an unsupported nickel catalyst. They observed that at high temperatures (350-750 °C), the nickel nanoparticles coalesce, and this modified their size and shape. They also observed the formation of a wide range of carbon nanofiber structures with typically larger diameters at

elevated temperatures. Also, it was found that the growth of the synthesized CNFs was difficult to control.

From all the studies described above, it is however noted that not only does the metal particle catalyze the dissociation of the hydrocarbon to form elementary carbon, but it also affects the structure of the CNFs. The CNFs grown can grow to any diameter and length as a result of metal agglomeration that affects the size and morphology of the catalyst. Consequently, this affects the morphology of the carbon nanofibers.

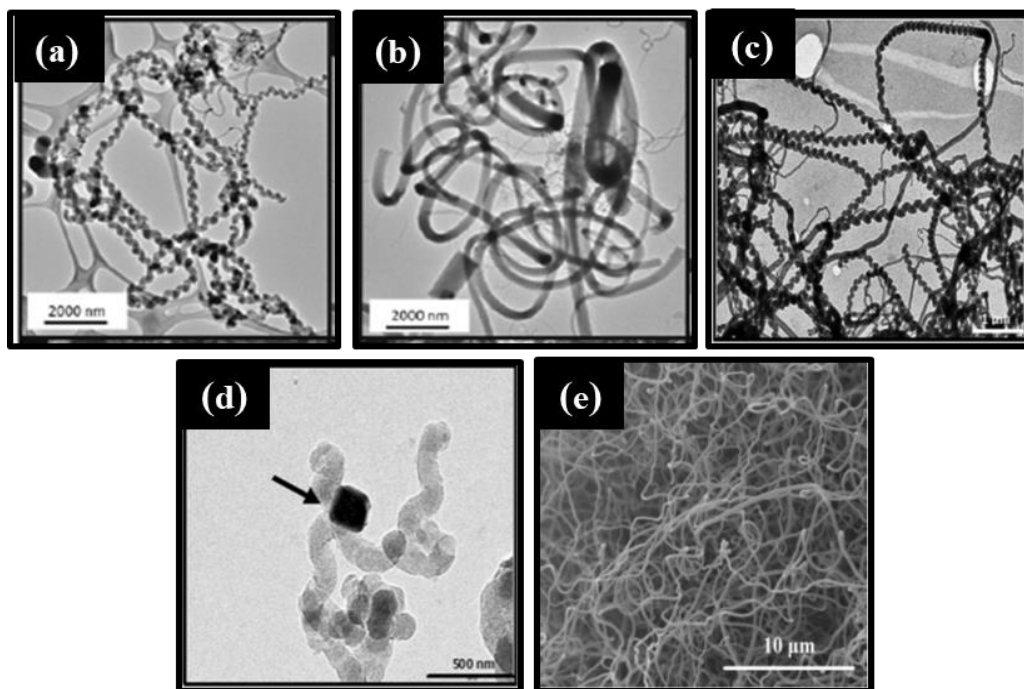


Figure 2. 6: TEM images of CNFs synthesized using (a) C_2H_2 , (b) C_2H_2/TCE [26] (c) HCNFs along with planar CNFs with a yield of $\sim 90\%$ and $\sim 10\%$ respectively (d) reveals that HCNF grown from the polygonal Ni nanoparticle (indicated by arrow) [48] and (e) SEM image of linear CNFs synthesized by CCVD at $660^\circ C$ for 3 min using Ni particles when the gas flow rate of C_2H_2 , H_2 , and N_2 was 20, 60 and 140 mL/min, respectively [45].

2.1.4.1.2. Supported metal catalysts

Attempts to make a stable catalyst system and impede the formation of larger catalyst clusters at high temperatures and grow CNFs in a more controllable manner usually require the use of a support for the metal catalyst particle. Many studies have been conducted by placing metal nanoparticles on traditional supports such as Al_2O_3 , SiO_2 , MgO TiO_2 and carbon-based materials for the growth of CNFs [37, 49-52]. Ahmed and co-workers [40] conducted a study on the synthesis of CNFs through nickel ion impregnated on powdered activated carbon (PAC).

Takenaka *et al.* [46] reported on the catalytic performance of cobalt catalysts supported on traditional supports (MgO , Al_2O_3 , SiO_2 , and TiO_2), for the preparation of carbon nanofibers and nanotubes by the pyrolysis of methane. They found that the catalytic activity of $\text{Co}/\text{Al}_2\text{O}_3$ and Co/MgO were more effective than Co/SiO_2 and Co/TiO_2 . Also, the CNFs had relatively uniform diameters although the Co crystallite sizes varied. The carbon nanotubes that formed exhibited a helically coiled and bamboo-like morphology.

Studies by Ren *et al.* [42] on the synthesis of helical carbon fibers over supported copper catalysts (Cu/MgO , $\text{Cu}/\text{Al}_2\text{O}_3$, Cu/SiO_2 , and Cu/TiO_2) revealed formation of helical carbon fibers at relatively low temperatures (lower than 250°C). They found that the CNFs varied in diameters from 80-100 nm. Also, the CNFs grown were of varying lengths.

Bhoware *et al.* [37] also demonstrated the growth of CNFs using both $\text{Cu}@/\text{SiO}_2$ and Cu/SiO_2 catalyst (**figure 2.7b, c**). They observed the sintering of Cu nanoparticles and a variety of morphologies of the CNFs (helical and straight fibers). They also noted that the surface (and bulk) properties of the CNFs were modified by the variation of the synthesis procedures used to make CNFs.

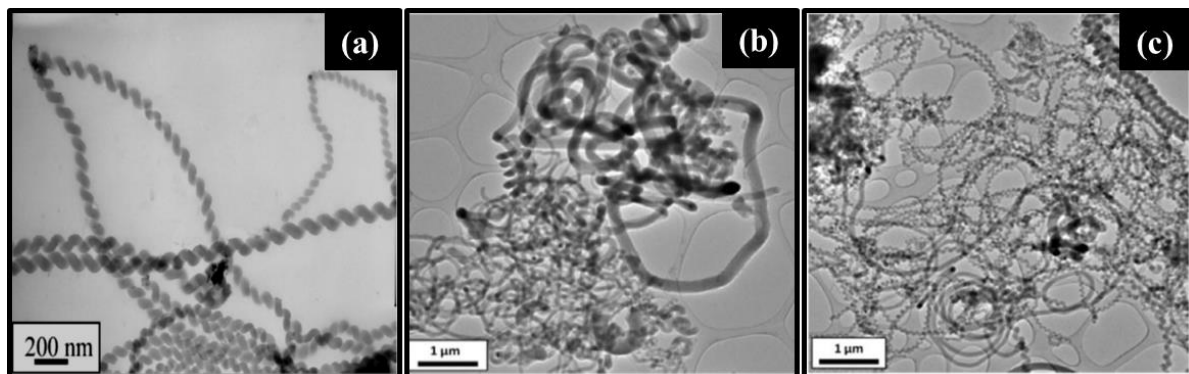


Figure 2. 7: TEM image of CNFs prepared from different catalyst supports (a) Cu/MgO [42], (b) $\text{Cu}@/\text{SiO}_2$ and (c) Cu/SiO_2 [37].

All these studies (from unsupported (**figure 2.6**) and supported (**figure 2.7**) catalyst) indicated that the shape and size of the catalyst influence the morphology of the CNFs that were formed. To control the sintering of metal NPs, it is therefore proposed that the design and fabrication of the encapsulation of metal NPs inside hollow carbon spheres can be used to prevent metal agglomeration control the catalytic activity of the catalyst to form CNFs and also control the length of CNFs.

2.2. Hollow carbon spheres

Hollow carbon spheres (HCSs) are hollow structured carbon materials that range from millimeters to nanometres in size as shown in **figure 2.8b**. Recently, these materials are of interest owing to their unique properties such as controllable permeability, encapsulation ability, surface functionality, etc. [54]. They also have excellent chemical and thermal stabilities [53-54]. The HCSs offer added advantages compared to other forms of carbon due to the ability to control their shell thickness, surface area and to vary their subsequent reactivity, compressive strength, pore structure, and variable cavity space. Depending on the desired hollow structure, different synthetic technologies such as hydrothermal carbonization (HTC), chemical vapour deposition (CVD), arc-discharge, laser ablation, etc. can be employed in their synthesis [53, 61 - 62].

2.2.1. Synthesis of the HCSs

Hollow carbon spheres are commonly prepared through three distinct synthetic methods (hard template, soft template, and template free) [61]. The first method uses a hard template that makes use of “rigid” materials as templates. The second method uses a soft template that involves the use of liquid droplets or micelles. Lastly, the template-free method allows the materials to self-assemble into the desired structures [62]. However, of these methods, hard and soft templating methods are the most commonly used methods since they provide ease in defining the shape and size of the desired hollow carbon material before synthesis. The self-assembly method, on the other hand, requires the material to assemble under ambient conditions. The templating methods are described in more detail below.

2.2.1.1. Hard templating strategy

The hard-templating approach has been widely adopted for the preparation of hollow carbon spheres since the method is straightforward and provides ease of controlling the size, shape, and structure of the HCSs. This method also provides opportunities for developing various carbon composite nanostructures such as rattle-type or yolk-shell nanostructures [63]. Generally, hollow carbon spheres are fabricated from a removable template material and the shell is made of a carbon layer as shown in **figure 2.8a**. The commonly used templating materials include silica spheres, polystyrene spheres (PSs) and metal nanoparticles [62]. This method involves coating the template with a carbon precursor such as toluene, or resorcinol formaldehyde on a template [61]. The template is then removed either by thermal treatment or a chemical agent (HF or NaOH) depending on the template employed to synthesize the HCSs

[54, 62]. Usually, the resulting hollow structure is similar to that of the template with well-defined and monodispersity morphology.

Although this method is powerful and widely employed, the method has some drawbacks which include a low product yield, a multistep synthetic process and the robustness of the shell that can be destroyed after etching [53-55, 62].

2.2.1.2. Soft templating strategy

A soft template method involves the formation of relatively flexible structures such as emulsion droplets, supramolecular micelles, and gas bubbles [61-62]. The method uses a surfactant and polymer as a directing agent. It involves self-assembly between the template and the polymer precursor. For example, glucose can be used as a carbon source [53]. Although this method offers ease of removal of the template, the morphology of the as-synthesized HCSs is usually poor.

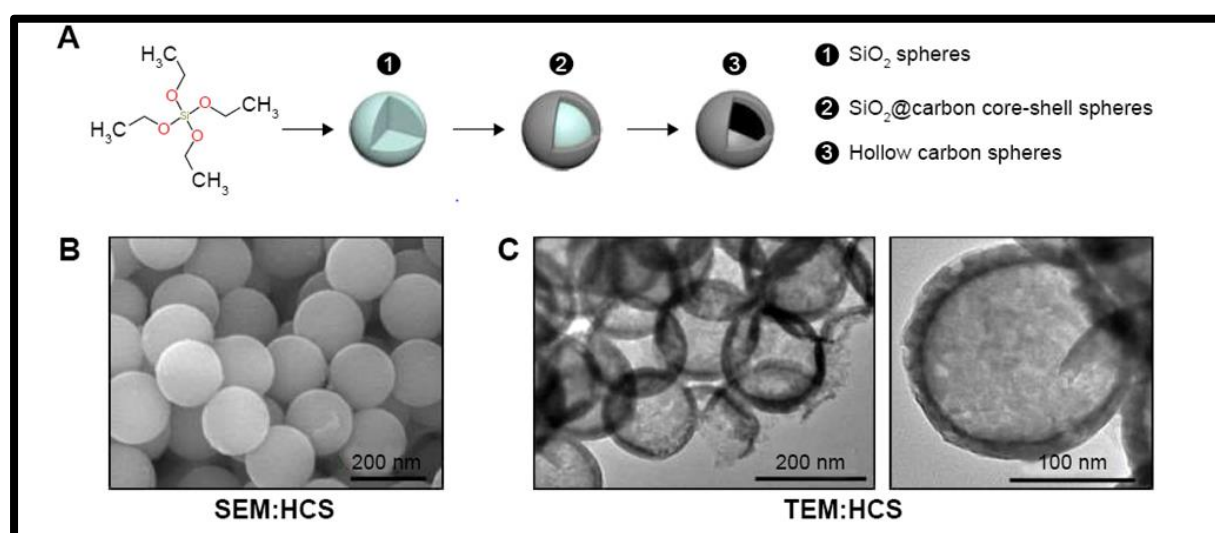


Figure 2. 8: The preparation and analysis of HCSs. (a) Schematic representation of HCSs synthesis. (b) SEM and TEM images of HCSs [55].

2.2.2. Applications of the HCSs

Hollow carbon spheres are currently playing an important role in a wide spectrum of fields due to their peculiar structural and chemical properties [57]. These materials have been used in catalysis as a supporting material [12, 80-81], in energy conversion and storage technologies (LIBs, fuel cells) and hydrogen storage [66-67].

2.2.2.1. Catalyst support

HCSs have been used as a support material for metal nanoparticles such as Sn [57], Au [61], Ru [51], to name a few, in catalysis to increase the activity of the metal catalysts. Phaahlamohlaka *et al.* [80] supported ruthenium nanoparticles on the HCSs for the FTS synthesis. Nongwe *et al.* [81] reported on the epoxidation of styrene using Co nanoparticles supported on nitrogen-doped hollow carbon spheres (Co/N-HCS) catalyst. The study revealed that Co/N-HCSs calcined at 300 °C resulted in excellent stability, activity (99% styrene conversion and 85% selectivity to styrene oxide), and recyclability. Chen *et al.* [82] observed enhanced catalytic activity and selectivity in the hydrogenation of nitrobenzene and oxidation of cinnamyl alcohol using Pd@HCSs catalyst compared with that of the conventional Pd/N-C and commercial Pd/C catalysts.

2.2.2.2. Energy storage

Lithium-ion batteries (LIBs) are one of the best energy storage technologies used in portable consumer electronics today due to their high energy density [61]. However, due to the development of electronic devices in the current era, there has been a high demand for developing new materials that can increase the energy density of the batteries and improve their performance [61, 65-67]. As such, hollow structured materials have been used as an electrode material due to their high surface area. They also provide short path lengths for Li transport [61]. A short Li path length reduces the overpotential and rapid capacity fading due to volume changes. This results in improved performance of the battery and allows better kinetics at the electrode surface.

Recently, metal encapsulated inside hollow carbon spheres has been used as anodes in LIBs. This is due to the good metal dispersion of metal oxides nanoparticles inside the carbon matrix. Carbon acts as a structural buffer and electrochemically active material in lithium insertion or extraction [57, 67]. Zhang and co-workers [66] synthesized tin (Sn) encapsulated inside hollow carbon spheres as an anode material in LIBs. They observed that tin particles do not form aggregates and all nanoparticles adhere to the inner surface of the carbon shell. They also observed high volume capacity, good cycle performance with a high specific capacity ($> 800 \text{ mA g}^{-1}$) in the initial 10 cycles. The author's ascribed this enhanced performance of the Sn@HCSs to the peculiar structure of the HCSs.

Chen *et al.* [83] prepared nitrogen-doped hollow mesoporous carbon spheres (N-HMCSs) for use in supercapacitors. The author's reported that the N-HMCSs exhibited a specific

capacitance of 170 F g^{-1} at a current density of 1.0 A g^{-1} and after 5000 cycles, the capacitance remained 94%. Additionally, HCSs has been used as a hydrogen storage material. Wu et al. [64] reported on electrochemical hydrogen storage experiments for their necklace-like hollow carbon nanospheres, which exhibited a capacity of 242 mAh g^{-1} at a current density of 200 mA g^{-1} , corresponding to hydrogen storage of 0.89 wt%.

2.2.2.3. Fuel cells

Fuel cells are one of the alternative energy conversion technologies that result in good power quality, high energy efficiencies, cleanliness, and low carbon dioxide emissions [63]. The performance of these cells depends on their electrode material. However, the conventional carbon-supported metal electrodes are too expensive for application and commercialization of fuel cells. Hollow nanospheres have been recognized as a potential electrode material due to their unique structure and inherent properties that provide enhanced surface-to-volume ratio and reduced transport lengths for both mass and charge transport [63].

Li *et al.* [67] reported on the viability of using hollow carbon spheres with germanium (Ge) (Ge@HCS) as an anode material for lithium ion batteries. The author's reported that the HCS minimized Ge agglomeration and maintained the structural integrity of the composite. They also observed that the Ge@HCS composite exhibited high performances as revealed by electrochemical studies. Studies by Bo *et al.* [84] and Hu *et al.* [85] showed that the Pt/HCSs and Pd/HCSs electrocatalysts, respectively, resulted in a higher catalytic activity in direct alcohol fuel cells compared with the commercial Vulcan XC-72 carbon. They ascribed this to the synergism of the hollow structure of the HCSs with micropores and channels.

2.2.3. Use of the HCSs as a nanoreactor

As discussed above, the HCSs possess a hollow cavity in which catalytic species can be incorporated in the voided space of the hollow nanostructures. These materials act as a nanoreactor or a reservoir whereas the shell provides a surface and a filter for the encapsulated substances [54, 56]. Studies have been carried out on the encapsulation of metal nanoparticles to make core-shell hollow carbon nanostructures in order to minimize the agglomeration of the encapsulated metal nanoparticles [51-57]. Various metal nanoparticles such as platinum, ruthenium, tin, gold and cobalt nanoparticles, to name a few have, been placed inside HCSs and studied [12, 51, 57,61, 66].

Not only can the HCSs function as a scaffold to hold encapsulated materials in place, but the hollow cavity can also be utilized to build structures (such as CNTs and CNFs) from the encapsulated metal. The research conducted by Yirka [68] demonstrated that it is possible to create building blocks inside of living cells. Since the HCSs possess a similar structure to that of the living cells, it can also be used to build structures inside the carbon framework. The porosity of the HCSs can be varied to allow nano-sized molecules to enter and exit the pores. The molecules can, therefore, penetrate through the pores and react with the encapsulated material. The larger units will remain embedded within the hollow cavity and small particles can exit the pores. This approach has similarities to the ‘ship-in the bottle’ philosophy used to make macro and microstructures in a constrained environment.

In this work, we wish to build nanostructured materials (CNFs) that are fully confined and have controlled dimensionality. The growth of materials inside the HCSs has rarely been explored. However, more recently, Gangatharan and co-workers [69] demonstrated the viability of building structures inside the HCSs using a Cu catalyst. The study revealed that the CNFs with a helical morphology were successfully prepared inside the HCSs as depicted in **figure 2.9**. They also observed that the HCSs provide ease control of the Cu nanoparticles and the growth of the CNFs. The physical separation of this material is not possible.

In light of this finding, to best of the author’s knowledge, the growth of carbon nanofibers from Ni encapsulated inside the HCSs has not been studied. Therefore, for the first time, this research focuses on the synthesis of Ni catalysts and growth of the CNFs inside HCSs using a Ni catalyst.

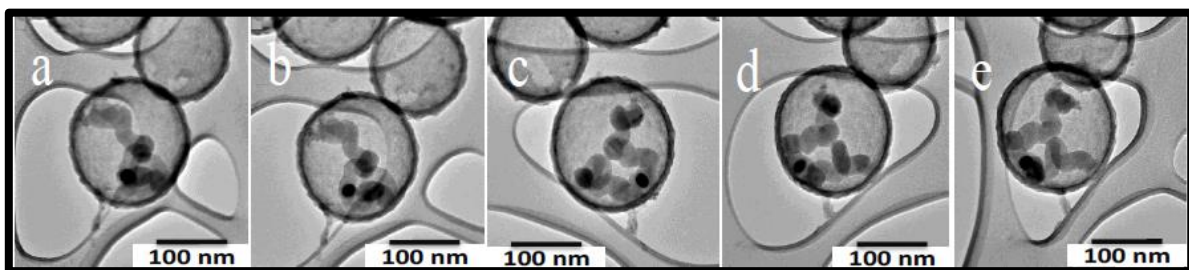


Figure 2. 9: TEM images of CNFs synthesized from CuO@HCSs catalyst as confirmed by tilting experiments. Image a-e show helix movement in an HCS as the tilting angle is varied, a) -60° b) -30° c) 0° d) +30° e) +60° [69].

References

1. P.S. Karthik, A.L. Himaja, S.P. Singh, *Carbon Letters*, 15 (4) (2014) 219-237.
2. B.T. Zhang, X. Zheng, H.F. Li, J.M. Lin, *Analytica Chimica Acta*, 784 (2013) 1-7.
3. K.S. Novoselov, A.K. Geim, S.V. Morozov, D. Jiang, Y. Zhang, S.V. Dubonos, I.V. Grigorieva, A.A. Firsov, *Science*, 306 (5696) (2004) 666-669.
4. H.W. Kroto, J.R. Heath, S.C. O'Brien, R.F. Curl, R.E. Smalley, *Nature*, 318 (1985) 162-163.
5. S. Iijima, *Nature*, 354 (1991) 56-58.
6. M.J. O'Connell, *Carbon nanotubes: Properties and Applications*, Taylor & Francis Group, LLC, (2006) 360.
7. Y. Li, Z. Liu, Y. Jiang, B. de Glee, D. Li, J. Zeng, *Material Science*, 53 (1) (2018) 479-491.
8. Y.A. Kim, T. Hayashi, M. Endo, M.S. Dresselhaus, *Carbon nanofibers, Handbook of Springer Nanomaterials*, Springer-Verlag, (2013) 233-262.
9. T. Chen, L. Dai, *Materials Today*, 16 (2013) 1369-7021.
10. A. Bianco, K. Kostarelos, M. Prato, *Expert Opinion on Drug Delivery*, 5(3) (2008) 331-342.
11. M. Antonietti, K. Müllen, *Chemical Synthesis and Applications of Graphene and Carbon Materials*, Wiley-VCH Verlag GmbH & Co. KGaA, (2017) 272.
12. T.N. Phaahlamohlaka, D.O. Kumi, M.W. Dlamini, R. Forbes, L.L. Jewell, D.G. Billing, N.J. Coville, *ACS Catalysis*, 7 (3) (2017) 1568-1578.
13. K.P. de Jong, J.W. Geus, *Catalysis Reviews-Science & Engineering*, 42 (4) (2000) 481-510.
14. N.J. Coville, S.D. Mhlanga, E.D. Nxumalo, A. Shaikjee, *South African Journal of Science*, 107 (3/4) (2011) 1-15.
15. L. Feng, N. Xie, J. Zhong, *Materials*, 7 (5) (2014) 3919-3945.
16. K.B.K. Teo, C. Singh, M. Chhowalla, W.I. Milne, *Encyclopedia of Nanoscience and Technology*, (2013) 1-22.
17. F. Salman, C. Park, R.T.K. Baker, *Catalysis Today*, 53 (3) (1999) 385-394.
18. E. Hammel, M. Tang, T. Schmitt, K. Mauthner, A. Eder, P. Pötschke, *Carbon*, 42 (2004) 1153-1158.
19. S. Yang, X. Chen, S. Motojima, M. Ichihara, *Carbon*, 43 (2005) 827-834.

20. Y. Gogotsi, V. Presser, *Carbon nanomaterials*, Taylor & Francis Group, LLC, (2014) 300.
21. F. Nitze, E. Abou-Hamad, T. Wägberg, *Carbon*, 49 (2011) 1101-1107.
22. K. Mondal, N.J. Coville, *Encyclopedia of Nanoscience and Nanotechnology*, 14 (2011) 161-203.
23. N.M. Rodriguez, *Journal of Materials Research Society*, 8 (12) (1993) 3233-3248.
24. B.K. Mutuma, *Synthesis and characterization of Solid, Hollow, Core-shell and worm-like carbon nanostructures for Application in Organic Photovoltaic Devices and Chemical Sensors*, Ph.D. thesis, University of the Witwatersrand, Johannesburg, (2016).
25. T.N. Phaahlamohlaka, *Synthesis of Carbon nanofibers and their subsequent use as catalyst supports for Fischer-Tropsch synthesis*, MSc Dissertation, University of the Witwatersrand, Johannesburg, (2013).
26. M.S. Maubane, S.S. Bhoware, A. Shaikjee, N.J. Coville, *Diamond & Related Materials*, 72 (2017) 53-60.
27. A. Shaikjee, N.J. Coville, *Carbon*, 50 (2012) 1099-1108.
28. J.P. Tessonnier, D.S. Su, *ChemSus Chem*, 4 (2011) 824-847.
29. R.T.K. Baker, *Carbon fibers, Filaments and composites*, NATO ASI series, Kluwer, Dordrecht, (1990) 405.
30. R.T.K. Baker, M.S. Kim, C. Chamber, C. Park, N.M. Rodriguez, *Studies Surf. Science catal*, (1997) 111.
31. J.-H. Zhou, Z.-J. Sui, P. Li, D. Chen, Y.-C. Dai, W.-K. Yuan, *Carbon*, 44 (2006) 3255-3262.
32. M.S. Maubane, *Nickel and copper catalysed synthesis of carbon fibers*, Ph.D. thesis, University of the Witwatersrand, Johannesburg, (2013).
33. Y. Liu, C. Pan, J. Wang, *Materials Science*, 39 (2004) 1091-1094.
34. X. Jian, M. Jiang, Z. Zhou, M. Yang, J. Lu, S. Hu, Y. Wang, D. Hui, *Carbon*, 48 (2010) 4535-4541.
35. D. Chen, K.O. Christensen, E. Ochoa-Fernández, Z. Yu, B. Tøtdal, N. Latorre, A. Monzón, A. Holmen, *Journal of Catalysis*, 229 (2005) 82-96.
36. S. Motojima, I. Hasegawa, S. Kagiya, M. Momiyama, *Applied Physical Letters*, 62 (1993) 2322.
37. S. Bhoware, M.S. Maubane, T. Phaahlamohlaka, A. Shaikjee, N.J. Coville, *Chemical Physics Letters*, 577 (2013) 71-75.

38. L. Feng, N. Xie, J. Zhong, *Materials*, 7 (5) (2014) 3919-3945.
39. S. Motojima, Q. Chen, *Journal of Applied Physics*, 85 (7) (1999) 3919.
40. Y.M. Ahmed, A. Al-Mamun, A.T. Jameel, M.F.R. AlKhatib, M.K. Amosa, M.A. AlSaadi, *Nanotechnology*, (2016) 10.
41. Y. Chen, C. Liu, J.-H. Du, H.-M. Cheng, *Carbon*, 43 (2005) 1874-1878.
42. X. Ren, H. Zhand, Z. Cui, *Materials Research Bulletin*, 42 (2007) 2202-2210.
43. L. Pan, M. Zhang, Y. Nakayama Y, *Journal of Applied Physics*, 91 (12) (2002) 10058.
44. L. Yu, Y. Qin, Z. Cui, *Materials Letters*, 59 (2005) 459-462.
45. X. Jian, D. Wang, H. Liu, M. Jiang, Z. Zhou, J. Lu, X. Xu, Y. Wang, L. Wang, Z. Gong, M. Yang, J. Gou, D. Hui, *Composites: Part B*, 61 (2014) 350-357.
46. S. Takenaka, M. Ishida, M. Serizawa, E. Tanabe, K. Otsuka, *Journal of Physical Chemistry*, 108 (2008) 11464-11472.
47. I. Martin-Gullon, J. Vera, J.A. Conesa, J.L. González, C. Merino, *Carbon*, 44 (2006) 1572-1580.
48. H. Raghubanshi, M.S. Hudson, O.N. Srivastava, *International Journal of Hydrogen Energy*, 36 (2011) 4482-4490.
49. Kun –H.J, Yura H, Young –H.P, Chang S.L, *Nanoscience and Nanotechnology*, 17 (11) (2017) 8500-8505.
50. A. Shaikjee, P.J. Franklyn, N.J. Coville, *Carbon*, 49 (2011) 2950-2959.
51. M.M. Titirici, M. Antonietti, A. Thomas, *Chemistry Materials*, 18 (2006) 3808-3812.
52. J. Wang, P. Hao, R. Shi, L. Yang, S. Liu, J. Zhao, J. Ren, Z. Li, *Nanoscale Research Letters*, 12 (2017) 481.
53. S. Li, A. Pasc, V. Fierro, A. Celzard, *Materials Chemistry A*, 4 (2016) 12684-12713.
54. B.I. Nongwe, *N-Doped, B-Doped carbon materials and yolk-carbon shell nanostructures: synthesis, characterization, and application for heterogeneous catalysis*, Ph.D. thesis, University of the Witwatersrand, Johannesburg, (2014).
55. L. Zhang, M. Yao, W. Yan, X. Liu, B. Jiang, Z. Qian, Y. Gao, X.J. Lu, X. Chen, Q. Wang, *International Journal of Nanomedicine*, 12 (2017) 6759-6769.
56. D.G. Lee, S.M. Kim, H. Jeong, J. Kim, I.S. Lee, *ACS Nano*, 8 (5) (2014) 4510-4511.
57. K.T. Lee, Y.S. Jung, S.M. Oh, *American Chemical Society*, 125 (19) (2003) 5652-5653.
58. M.L. Toebes, F.F. Prinsloo, J.H. Bitter, A.J. van Dillen, K.P. de Jong, *Journal of Catalysis*, 214 (2003) 78-87.
59. G.L. Bezemer, P.B. Radstake, V. Koot, A.J. van Dillen, J.W. Geus, K.P. de Jong, *Journal of Catalysis*, 237 (2006) 291-302.

60. X. Huang, *Materials*, 2 (2009) 2369-2403.
61. R. Liu, S.M. Mahurin, C. Li, R.R. Unocic, J.C. Idrobo, H. Gao, S.J. Pennycook, S. Dai, *Angewandte Chemie International Edition*, 50 (2011) 6799-6802.
62. J. Hu, M. Chen, X. Fang, L. Wu, *Chemical Society Reviews*, 40 (2011) 5472-5491.
63. X. Lai, J.E. Halpert, D. Wang, *Energy and Environmental Science*, 5 (2012) 5604-5618.
64. C. Wu, C. Zhu, L. Ye, C. Ouyang, S. Hu, L. Lei, Y. Xie, *Inorganic Chemistry*, 45 (2006) 8543-8550.
65. H.-P. Liang, H.-M. Zhand, J.-S. Hu, Y.-G. Guo, L.-J. Wan, C.-L. Bai, *Angewandte Chemie International Edition*, 43 (12) (2004) 1540-1543.
66. W.-M. Zhang, J.-S. Hu, Y.-G. Guo, S.-F. Zheng, L.-S. Zhong, W.-G. Song, L.-J. Wan, *Advanced Materials*, 20 (2008) 1160-1165.
67. D. Li, C. Feng, H.K. Liu, Z. Guo, *Journal of Materials Chemistry A*, 3 (3) (2015) 978-981.
68. B. Yirka, *Researchers make synthetic polymers inside of living cells*, (22/04/2019), <https://phys.org/news/2019-04-synthetic-polymers-cells.html>, Accessed on 5/01/2020.
69. P.M. Gangatharan, M.S. Maubane, N.J. Coville, *Scientific Reports*, 9 (1) (2019) 1-7.
70. F. Salman, C. Park, R.T.K. Baker, *Catalysis Today*, 53 (3) (1999) 385-394.
71. V. Barranco, M.A. Lillo-Rodena, A. Linare-Solano, A. Oya, F. Pico, J. Ibanez, F. Agullo-Rueda, J.M. Amarilla, J.M. Rojo, *Journal of Physical Chemistry C*, 114 (22) (2010) 10302-10307.
72. Z. Zhou, X.-F. Wu, *Journal of Power Source*, 222 (2013) 410-416.
73. M. Aslam, P. Shafigh, M.Z. Jumaat, S.N.R. Shah, *Construction and Building Materials*, 82 (2015) 235-256.
74. T. Sayali, *Global carbon Fiber Reinforced Plastics (CFRP) Market Future Demand and Growth Analysis*, (23/03/2018), <https://www.coherentnews.com/global-carbon-fiber-reinforced-plastics-cfrp-market-future-desmand-and-growth-analysis/>, Accessed on 11/07/ 2018.
75. R. Usamentiaga, C. Ibara-Castanedo, M. Klein, X. Maldague, J. Peeters, A. Sanchez-Beato, *Sensors*, 17 (11) (2017) 2679.
76. S. Visal, S.U. Deokar, *International Journal of Innovative Research in Science & Technology*, 2 (12) (2016) 2349-6010.
77. R. Kussmaul, M. Zogg, L. Weiss, E. Relea, R. Jacomet, P. Ermanni, *Procedia CIRP*, 66 (2017) 10-15.

78. M.W. Lekota, K.P. Dimpe, P.N. Nomngongo, *Journal of Analytical Science and Technology*, 25 (2019) 10.
79. S. Takenaka, H. Ogihara, K. Otsuka, *Journal of Catalysis*, 208 (2002) 54-63.
80. T.N. Phaahlamohlaka, D.O. Kumi, M.W. Dlamini, L.L. Jewell, N.J. Coville, *Catalysis Today*, 275 (2016) 76-78.
81. I. Nongwe, V.Ravat, R. Meijboom, N.J. Coville, *Applied Catalysis A: General*, 466 (2013) 1-8.
82. L. Chen, L. Zhang, Z. Chen, H. Liu, R. Luque, Y. Li, *Chemical Science*, 7 (2006) 6015-6020.
83. A. Chen, Y. Li, Y. Yu, S. Ren, Y. Wang, K. Xia, S. Li, *Journal of Alloys and Compounds*, 688 (2016) 878-884.
84. X. Bo, J. Bai, J. Ju, L. Guo, *Journal of Power Sources*, 196 (2011) 8360-8365.
85. F.P. Hu, Z. Wang, Y. Li, C. Li, X. Zhang, P.K. Shen, *Journal of Power Sources*, 177 (2008) 61-66.

CHAPTER 3

Synthesis and characterization of Ni nanoparticles encapsulated inside hollow carbon spheres.

3.1. Introduction

The interest in nanostructured materials continues to intensify in the nanoscience and nanotechnology fields due to their unusual and fascinating properties and their noteworthy applications [1]. Among the various nanomaterials, metal oxides made of, for example, Cu, Fe, and Ni have steadily been explored for the development of this class of materials. These nanomaterials have been shown to exhibit exceptional optical, magnetic, electrical, and catalytic properties [1-4]. As such, these metal nanoparticles find potential applications in fields such as gas sensors [2], fuel cells, battery cathode material, pigments, surface-enhanced Raman scattering (SERS) materials, etc. [1,3-5]. In general, metal oxides have been prepared through a variety of methods which include ultrasonic spray pyrolysis, liquid-control-precipitation, electro-deposition, chemical vapour deposition (CVD), the sol-gel route, reduction of metallic salts followed by oxidation of metallic species and pulsed laser ablation [2-5, 24-27].

Metal nanoparticles (NPs) are also used in heterogeneous catalytic processes such as hydrogenation [9], C-C coupling reactions [8], carbonylation [7], oxidation [11], and methanol-reforming [7] to name a few. However, as a result of high active surface atoms, metal NPs become intrinsically unstable under conditions of high temperature and pressure. Consequently, these materials tend to aggregate forming large clusters that become catalytically inactive limiting the industrial application of the catalyst. As such, different routes involving capping agents and solid supports have been explored to improve the thermal stability of metal NPs. Capping agents such as organic and inorganic ligands, surfactants or micelles and polymers bind weakly to the surface of the metal NPs and can limit metal NPs agglomeration [10]. However, these capping agents block the active sites through substituent coverage, consequently decreasing the catalytic activity of the catalyst [11]. Moreover, several studies have been conducted on metal NPs dispersion on solid supports such as TiO₂, ZrO₂, CeO₂, Al₂O₃, Fe₃O₄, SiO₂ [7], and solid carbon spheres to stabilize metal NPs at elevated temperatures. However, these supports are not completely effective in improving the thermal

stability of metal nanoparticles since metal NPs aggregation is still observed at elevated temperatures [19]. The metal also reacts with metal oxide supports forming spinels, which reduces the amount of active metal. Thus, there has been a great devotion to developing new strategies/approaches to circumvent this sintering problem and to fabricate catalytically stable systems. Recently, metal NPs confinement within carbon nanotubes (CNTs) and hollow carbon spheres (HCSs) have been explored. It has been observed that these approaches confine the NPs and minimize metal support interactions due to the chemically inert carbon [16-19].

The HCSs also offers added advantages over traditional solid supports due to their combined high surface area and large pore volume with good chemical inertness and mechanical stability [18]. The HCSs exhibit a hollow cavity that can act as a nanoreactor or a reservoir to encapsulate various nanomaterials even at nanometre sizes. The filling of nanomaterials inside HCSs can enhance the catalytic performance of the catalyst because the carbon shell can act as a barrier that prevents their coalescence behaviour compared to those loaded on the outer surface.

Previously, several studies have been conducted on the encapsulation of various metal nanoparticles such as platinum [18], ruthenium [19], tin, and cobalt [19] nanoparticles inside HCSs. However, only a few studies have been done on nickel, iron and copper nanoparticles since these materials are easily oxidized. To the best of the author's knowledge, the encapsulation of nickel inside the hollow carbon spheres has rarely been studied.

Herein, we report on the confinement of nickel nanoparticles in HCSs that relies on the hard template method described in **chapter 2** (section 2.2.) using monodispersed polystyrene spheres as the template. In this study, the CVD technique was employed to synthesize the HCSs, NiO/HCSs, and NiO@HCSs catalysts. We also demonstrate the efficacy of nickel encapsulation inside the HCSs compared to depositing nickel outside the HCSs.

3.2. Experimental procedure

3.2.1. Materials

The chemical reagents, styrene (Sigma Aldrich), polyvinylpyrrolidone (PVP, MW 40000, Sigma Aldrich), ammonia solution (25%; Fluka), ethanol (absolute, 99%; MK Chemical), ethanol (96%, MK Chemical), nickel acetate tetrahydrate ($\text{Ni}(\text{CH}_3\text{CO}_2)_2 \cdot 4\text{H}_2\text{O}$, Aldrich), hydrazine monohydrate (98%, Sigma Aldrich), resorcinol (Sigma Aldrich), formaldehyde solution (≥ 34.5 wt%; Sigma Aldrich), hexadecyltrimethylammonium bromide (CTAB, ≥ 98

%, Sigma Aldrich) were used as received. Deionized water was used for the preparation of all aqueous solutions.

3.2.2. Synthesis of polystyrene spheres (PSs)

The monodispersed polystyrene spheres were prepared by dispersing styrene (16 mL) and PVP (MW 40000, 0.2 g) in 250 mL water/ethanol solution (50 mL water and 200 mL ethanol) by sonication and then the mixture was stirred for 15 min [19]. A solution of potassium persulfate (0.3 g) dissolved in 20 mL water was added slowly while stirring and then the solution was stirred for a further 15 min. The mixture was then refluxed at 80 °C while stirring for 24 h. The final product was then centrifuged at 18000 rpm for 15 min and washed repeatedly with ethanol and then water. The resulting product was dried at 60 °C for 1 h and labelled **PSs** (~10 g yield).

3.2.3. Loading of Ni on the polystyrene spheres (NiO/PSs)

PSs (3 g) was dispersed in 150 mL water and 75 mL ethanol by ultra-sonication for 30 min. To this solution, nickel acetate tetrahydrate (0.5 wt%, 5 wt%, and 10 wt%) was added while stirring until the Ni salt completely dissolved. The Ni was deposited on the PSs by slow addition of hydrazine (2 M, 50-60%; different volumes were used depending on the Ni wt% loading used). The solution was left stirring at room temperature for 12 h for complete deposition of Ni nanoparticles. The final product was then filtered and washed using ethanol and dried at 60 °C for 12 h. The composites were labelled **NiO/PSs** at different metal loadings e.g. 0.5 wt% NiO/PSs (i.e. using the theoretical 0.5 wt% loading onto the PSs).

3.2.4. Synthesis of Ni inside hollow carbon sphere (NiO@HCSs)

Typically, NiO/PSs (different Ni loadings) or PSs (2 g) and ammonia solution (25%, 3 mL) were dispersed in a water/ethanol solution (water 33 mL and 100 mL ethanol) by ultrasonication for 30 min. A solution containing formaldehyde (37%, 3 mL), resorcinol (1 g), CTAB (1.5 g) and ethanol (75 mL) was added slowly to the latter and the resultant solution was stirred for 12 h at room temperature to form a resorcinol-formaldehyde (RF) polymer around the Ni/PSs or PSs composites. The resulting composite (NiO/PSs@RF or PSs@RF) was then placed in an oil bath and heated at 80 °C for 24 h to ensure complete polymerization of RF around the spheres. The resulting products were filtered and washed repeatedly with water followed by drying at 60 °C for 12 hours. The dry composite (NiO/PSs@RF or PSs@RF) was then heated inside a horizontal tube furnace in a one-step process to remove the template and carbonize the materials. This was achieved by heating the composites under nitrogen flow (80 ml/min) at a heating rate of 5 °C/min at 350 °C for 70 min to decompose the PSs followed

by annealing of carbon spheres at 600 °C for 1 h. The resultant products were labelled NiO@HCSs (0.5 wt% NiO@HCSs, 5 wt% NiO@HCSs, and 10 wt% NiO@HCSs) and HCSs.

3.2.5. Loading of Ni outside HCSs (NiO/HCSs)

Decoration of Ni nanoparticles outside the HCSs was achieved by a homogeneous deposition precipitation (HDP) procedure using hydrazine [19]. The HCSs (200 mg) were dispersed in 30 mL of water and 15 mL ethanol solution by ultra-sonication for 30 min. To this solution, nickel nitrate hexahydrate (5 wt%, only one loading was prepared) was added and the solution was stirred for 3 h. Hydrazine solution was then added slowly and the resulting solution was stirred for a further 12 h at room temperature to reduce the metal. The slurry solution was washed repeatedly with ethanol and filtered. The sample was then dried at 60 °C in an oven. The sample was labelled NiO/HCSs. In another reaction, NiO/HCSs (10 mg) material was annealed at 600 °C for 1 h to investigate the effect of annealing the material at high temperature when the metal is supported outside the HCSs.

3.2.6. Characterization techniques

Various characterization techniques such as TEM, SEM, Raman spectroscopy, TGA, BET, and PXRD were used to assess the physical and chemical properties of the synthesized materials.

3.2.6.1. Transmission electron microscopy (TEM)

The internal morphology of the materials was assessed using a FEI Tecnai Spirit G² TEM operating at 120 kV. A sample specimen was prepared by dispersing a small amount of the samples in ethanol by ultra-sonication for 30 min. A few drops of the resulting homogeneous solutions were deposited onto a carbon-coated copper grid and the solvent was dried in ambient air before sample analysis. The diameters of the samples obtained were measured using ImageJ 1.48v software.

3.2.6.2. Scanning electron microscopy (SEM)

The external surface morphology of the samples was determined using a FEI Nova Nanolab 600 FIB/SEM. Small amounts of the samples were evenly spread on a carbon tape mounted on a stub. Before introducing the samples into the instrument, the samples were coated with a thin layer of carbon and palladium/gold alloy to make the materials conductive. Thereafter, the stub was placed in the SEM, operating at 30 keV to obtain the images.

3.2.6.3. Temperature programmed reduction (TPR)

A Micromeritics AutoChem II instrument was used for the determination of the degree of reduction and reducibility of the catalysts. A sample of 50 mg was degassed at 150 °C for 30 minutes in the flow of helium gas (50 mL/min). TPR analysis measurements were performed using 5% H₂ gas in Ar (50 mL/min) at 1 bar pressure while the temperature was raised to 900 °C at a heating rate of 10 °C/min.

3.2.6.4. Raman spectroscopy

The degree of graphitization of the synthesized materials was analyzed using a Jobin-Yvon T64000 Raman spectrometer equipped with a laser excitation wavelength of 532 nm and a liquid N₂ cooled charge-coupled device detector. The data obtained were analyzed using Origin 8.50 software to measure the areas and intensities of the obtained Raman bands.

3.2.6.5. Thermal gravimetric analysis (TGA)

The thermal stability of the samples was investigated using a PerkinElmer STA6000 analyser. For each sample, about 10 mg of the sample was placed in a ceramic pan and then placed inside the furnace heated from 30 to 900 °C at a heating rate of 10 °C/min under air (20 mL/min). The thermogravimetric analysis with differential thermal gravimetry (TGA-DTG) profiles were recorded from 10 mg samples without any prior treatment.

3.2.6.6. Brunauer Emmet and Teller (BET) analysis

A Micromeritics Tristar 3000 instrument at 77 K was employed to determine the textural properties of the samples. Before sample analysis, the samples (~0.1 g) were degassed at 150 °C for 4 h in N₂ gas using a Micrometric flow Prep 060 sample degasser. The pore size distributions were evaluated from the desorption branches of the isotherms using the Barrett–Joyner–Halenda (BJH) method. The micropore surface area and volume were calculated using t-plot report data.

3.2.6.7. Powder X-ray diffraction (PXRD)

The bulk composition of the synthesized materials was analyzed using a Bruker D2 phaser equipped with a Lynxeye diffractometer using Cu-K α radiation at 30 kV and 10 mA. Before analysis, the samples were finely ground and placed on a sample holder ensuring a flat surface of the sample before analysis. The scan ranged from $10^\circ \leq 2\theta \leq 90^\circ$ in 0.0260 steps and the scans were carried out for 1 h. The phases present on the measured PXRD patterns were identified by a comparison with data stored in databases by using the EVA software package.

3.3. Results and Discussion

This chapter is divided into two sections. The first section **3.3.1** discusses the metal-supported outside the HCSs and the second section **3.3.2** addresses the efficiency of metal confinement inside the HCSs.

3.3.1. Characterization of NiO/HCSs catalyst

3.3.1.1. Morphology analysis: TEM

Transmission electron microscopy was used to reveal the morphology and the interior structure of the as-synthesized materials i.e. the polystyrene spheres (PSs) template, HCSs and nickel catalysts. **Figure 3.1** shows PSs and HCSs particles and their respective particle size distribution curves. The PSs illustrated in **figure 3.1a, b** possess a uniform spherical shape with a diameter of 498 ± 21 nm. After coating the template with a carbon layer in a solution containing RF, and oven drying, the material was placed in a CVD reactor to decompose PSs and form HCSs. The resulting HCSs kept the initial spherical morphology of the PSs. The HCSs represented in **figure 3.1c, d** reveal a hollow carbon structure support with a diameter of 433 ± 42 nm and a shell thickness of 55 ± 10 nm. It was observed that after PSs decomposition the diameter of the HCSs decreased. This is as a result of a possible shrinkage of the spheres during the removal of the PSs template. Similar results were reported in literature by Ravat *et al.* [38].

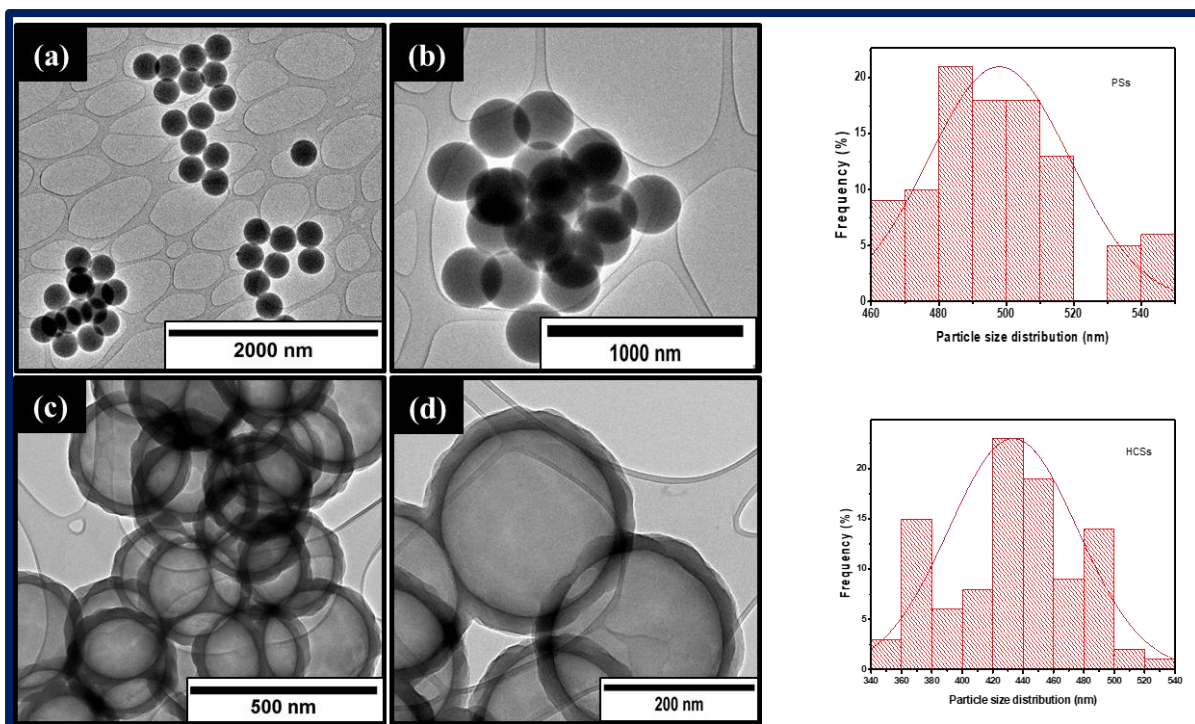


Figure 3. 1: TEM micrographs of PSs (a-b) and HCSs (c-d) and their corresponding particle size distribution curves, respectively.

The nickel salt (5 wt%) was loaded onto the surface of the HCSs to give a NiO/HCSs material using the homogeneous deposition precipitation (HDP) method [19]. **Figure 3.2** shows TEM images of NiO/HCSs and the annealed material at 600 °C. The material was annealed at 600 °C to demonstrate the effect of high-temperature treatment on the metal nanoparticles loaded outside as opposed to encapsulating metals inside the HCSs. The NiO/HCSs material depicted in **figure 3.2a, b** shows a uniform dispersion of nickel nanoparticles supported on HCSs before annealing with an average particle diameter of about 17 ± 8 nm. The HCSs retained their spherical morphology after the incorporation of Ni nanoparticles. After annealing at 600°C (10 °C/min heating rate), Ni nanoparticles formed large aggregates with a quasi-spherical morphology (**figure 3.2c, d** see arrow). The average particle size of the Ni nanoparticles after annealing was found to be 35 ± 11 nm as depicted on the particle size distribution curve. This was deduced by the high temperature (600 °C) treatment of the catalyst in the CVD reactor during the introduction of the N₂ gas (80 mL/min), which caused small crystallites to sinter and form bigger particles. Thus the number of particles present per sphere was also reduced (*ca.* < 10 particles). Similar results have been reported in [15, 38, 41]. Also, as a result of this high-temperature treatment, the nickel nanoparticles appear to have reacted with the carbon to form tubular-like structures ($d = \sim 25 \pm 6$ nm) that form a shell around the Ni particles (**figure 3.3,**

indicated by arrows). These structures are formed in high yield (*ca.* > 10%) and seem to be growing from nickel nanoparticles. They show a coiled morphology and are short in length.

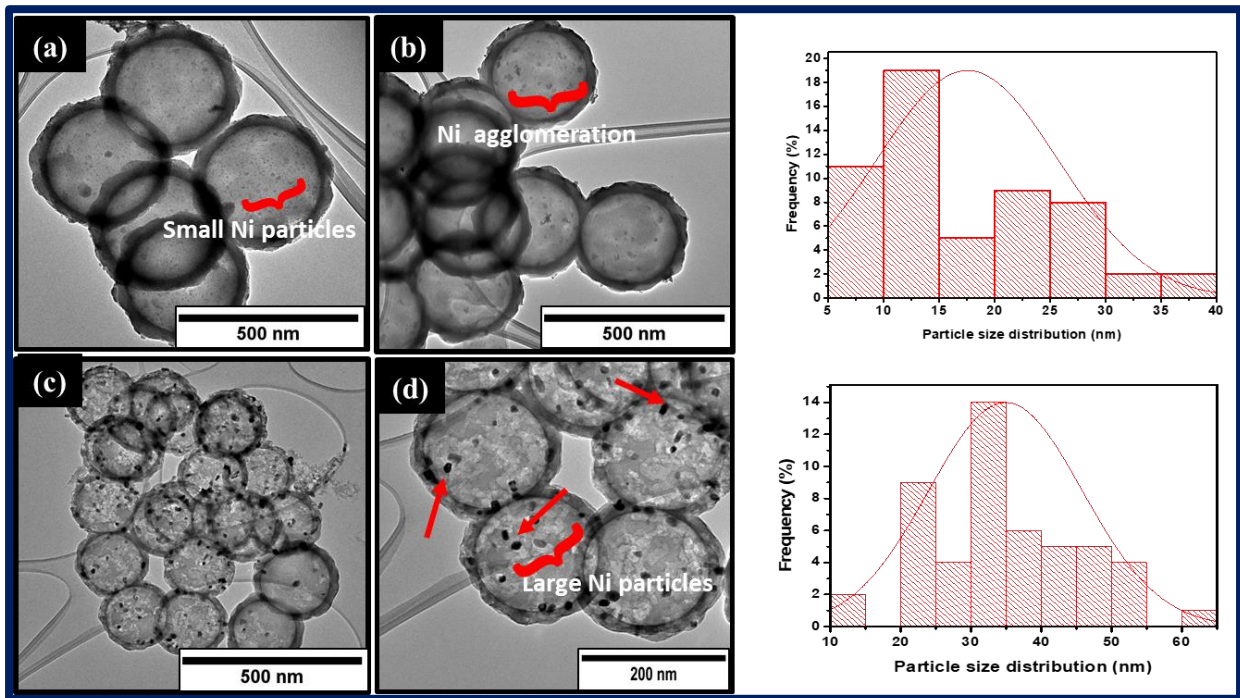


Figure 3. 2: TEM images of NiO/HCSs (a-b) and NiO/HCSs_annealed (c-d) and their corresponding particle distribution curves.

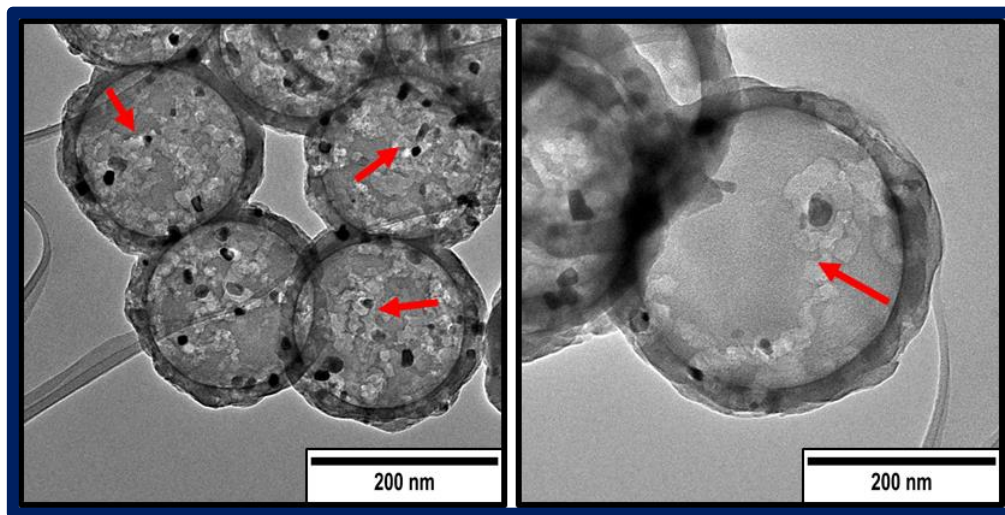


Figure 3. 3: TEM images of tubular-structures formed as a result of annealing at high magnification.

3.3.1.2. XRD analysis of NiO/HCSs catalyst

X-ray diffraction (XRD) analysis was done to identify the crystallinity of HCSs and Ni (**figure 3.4**). The HCSs and NiO/HCSs diffraction patterns show broad diffraction peaks at the Bragg angle range $20\text{--}30^\circ$ corresponding to the (002) plane of graphite. The HCSs peak was observed after annealing. NiO/HCSs showed three broad peaks at $2\theta = 37^\circ, 43^\circ$ and 63° corresponding to the (111), (200) and (220) planes of NiO after loading Ni onto the HCSs support. The presence of these peaks confirmed the loading of Ni onto HCSs support. After annealing, five notable diffraction peaks due to NiO crystallites and very small peaks due to Ni were observed at $2\theta = 37^\circ, 43^\circ, 44^\circ, 52^\circ, 63^\circ, 76^\circ$ and 80° corresponding to (111), (200), (111), (200), (220), (311) and (222) planes of the fcc structure of NiO/Ni crystallites, respectively. This data is in agreement with that of JCPDS card no. 47-1045 data [21]. The presence of Ni was a result of carbon reducing NiO species to Ni particles at high temperatures. Moreover, the observed sharp peaks of NiO correspond to the large particles observed from TEM images due to annealing.

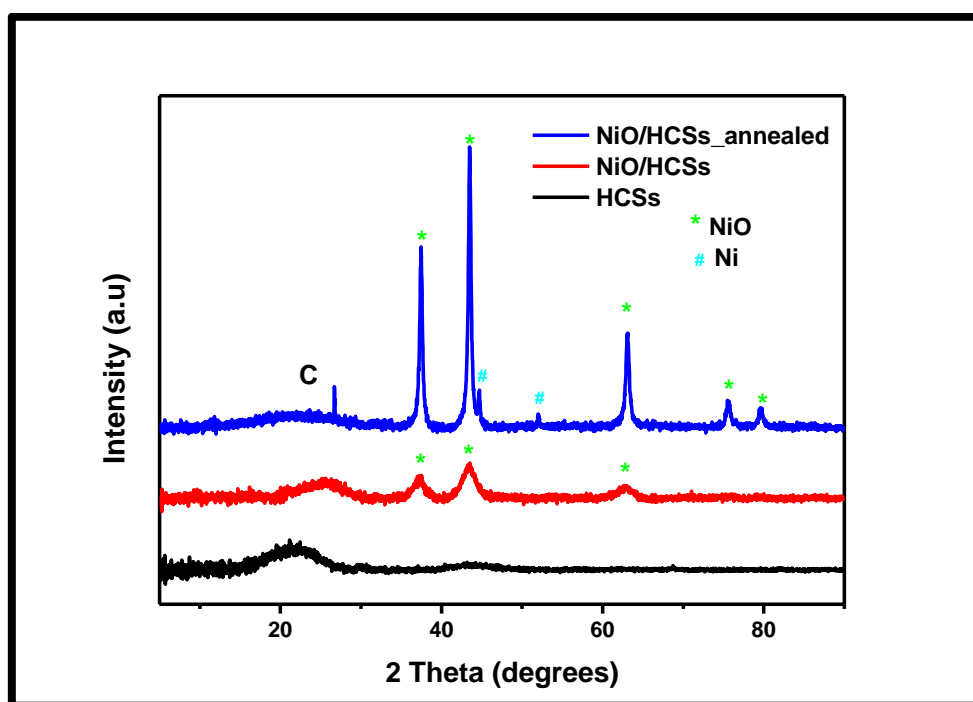


Figure 3. 4: XRD patterns of HCSs, NiO/HCSs, and NiO/HCSs_annealed.

The NiO and Ni crystallites size were estimated using the Scherrer equation [19].

$$\text{Scherrer Equation..... } D_{hkl} = \frac{K\lambda}{\beta \cos \theta}$$

where D_{hkl} is the crystallite size, K - Scherrer's constant ($K=0.89$), λ –X-ray wavelength (0.179 nm), β = line broadening of full width half maximum diffraction peak in radians and θ = Bragg's angle.

The most intense diffraction peaks of NiO/HCSs and NiO/HCSs_annealed characterized by the (200) plane at $2\theta = 43^\circ$, were used to estimate the average crystallite size of nanoparticles. Assuming that the Ni nanoparticles are spherical, the crystallite size of NiO using Scherrer equation was estimated to be 11 nm and 29 nm NiO/HCSs and NiO/HCSs_annealed, respectively. The calculated crystallite sizes obtained are slightly lower than the data obtained from TEM analysis. The reason for the difference could be that Scherrer equation applies to particles size with ranges up to 100-200 nm which may be made up by large particles of NiO [19, 37,42] and also the calculations were done only considering the (200) plane although the materials consist of several polycrystalline particles exposed on the surface of the HCSs. The size of the Ni particles was not determined.

3.3.1.3. TPR analysis of the NiO/HCSs catalyst

Temperature programmed reduction (TPR) was employed to assess the reduction temperature of the NiO/HCSs catalyst. **Figure 3.5** presents a TPR profile of the Ni nanoparticles supported outside the HCSs. The TPR profile showed one peak at 224 °C which indicates a one-step reduction of NiO_x to Ni in the as-prepared sample. This data correlates with the data observed in the literature for the reduction of NiO to metallic Ni species, which indicates only one peak for this conversion [36]. The TPR result corroborates the XRD data acquired which revealed only one NiO phase.

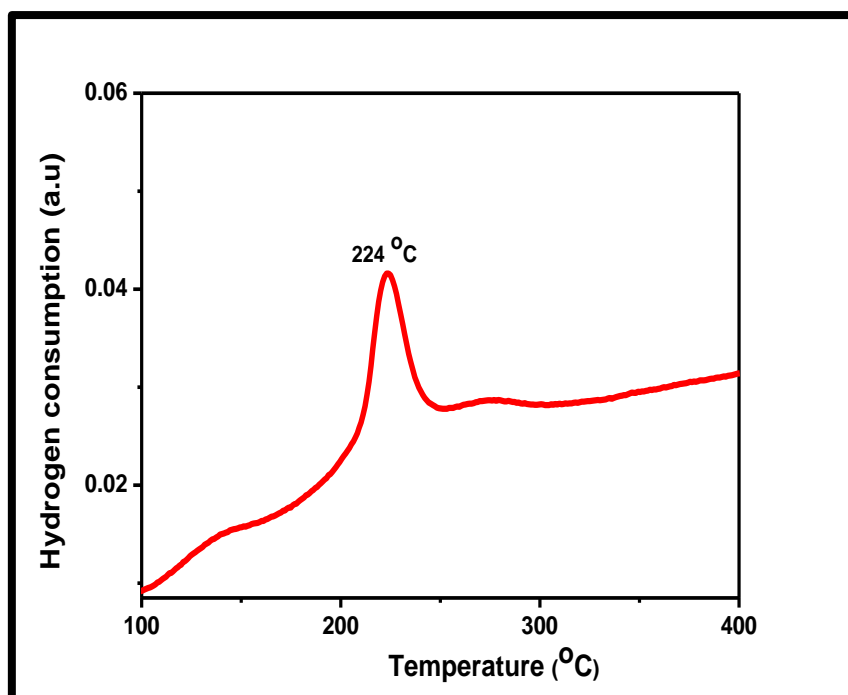


Figure 3. 5: TPR profile of NiO/HCSs catalyst.

3.3.1.4. BET analysis of HCSs and NiO/HCSs catalyst

To understand the surface properties of the HCSs and NiO/HCSs catalysts, the Brunauer-Emmet-Teller (BET) method was used to determine their surface area and porosity characteristics. **Figure 3.6** shows the N₂ adsorption-desorption isotherms of the obtained HCSs and NiO/HCSs and their corresponding pore distribution curves. Both HCSs and NiO/HCSs isotherms exhibit a hysteresis loop with a type III shape according to the IUPAC nomenclature [42]. The BET surface area of the HCSs and NiO/HCSs were found to be 395 m²/g and 402 m²/g (**Table 3.1**), respectively. The increase in surface area in the NiO/HCSs suggests no apparent blockage of the pores by Ni nanoparticles. The observed pore diameters also have similar values. This suggests little or no blockage of the pores. The pore distribution curves show that HCSs and NiO/HCSs have mesopores with a pore size ranging from 3-4 nm.

Table 3. 1: Textural properties of the as-synthesized HCSs and NiO/HCSs catalyst

Type of sample	BET Surface Area (m ² /g)	Pore volume (cm ³ /g)	Pore diameter (nm)
HCSs	395	0.22	3.5
Ni/HCSs	402	0.20	3.4

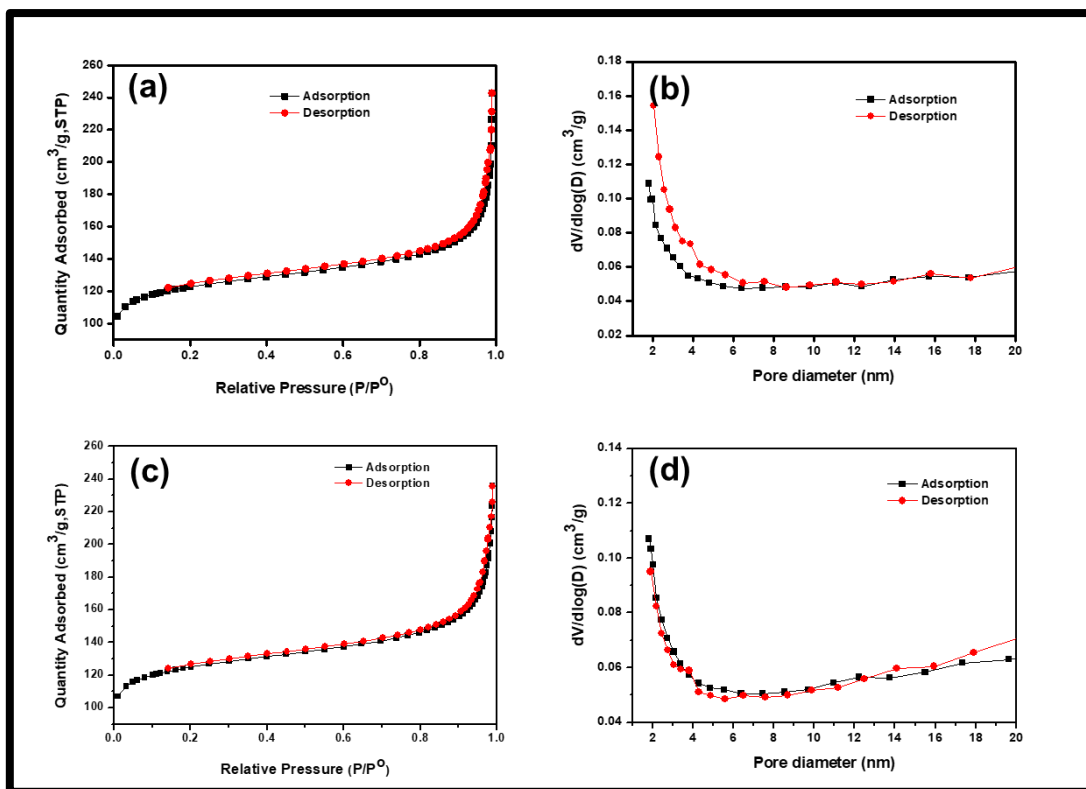


Figure 3. 6: Typical N₂ adsorption-desorption of (a, b) HCSs and (c, d) NiO/HCSs and their corresponding pore size distribution curves.

3.3.1.5. TGA analysis of HCSs and NiO/HCSs catalyst

Thermogravimetric analysis was conducted to assess the thermal stability of the as-prepared materials. Thermogravimetric curves and differential thermal gravimetric (DTG) profiles of HCSs and NiO/HCSs are shown in **figure 3.7**. **Figure 3.7a** shows the weight loss of various components of the HCSs as a function of temperature. After oxidation at 900 °C, the HCSs gave no residues (0 wt%), indicating complete removal of the PSs template and high purity of the HCSs. The NiO/HCSs catalyst gave 4.8 wt% mass residue attributed to the presence of nickel oxide particles on HCSs. This gives a Ni content of *ca.* 3.8 wt% loading.

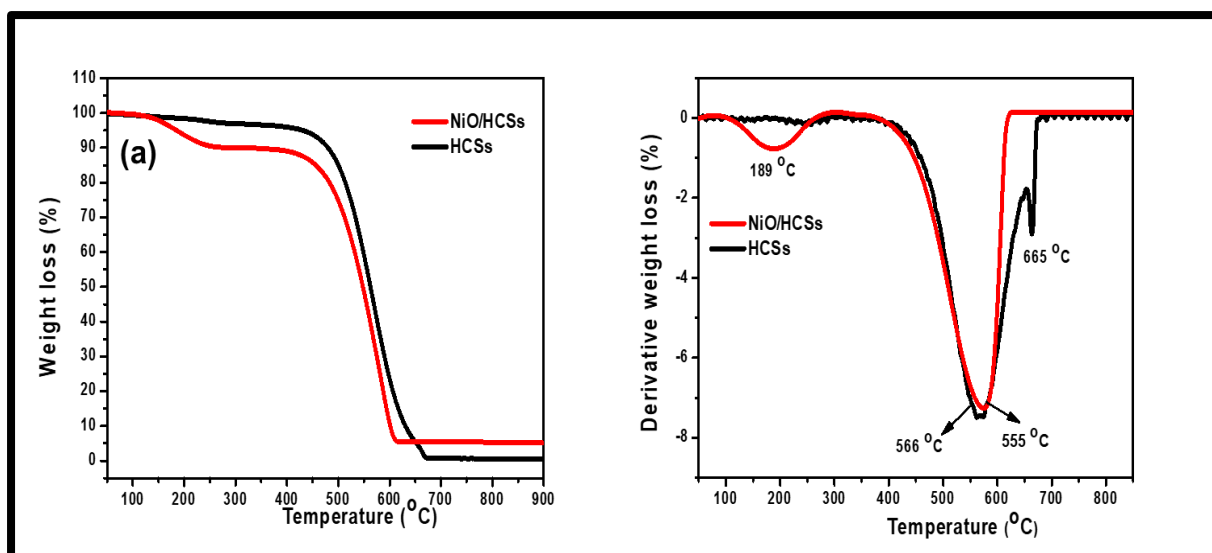


Figure 3. 7: Shows percentage weight loss of as-prepared materials as a function of temperature, (a) TGA and (b) DTG profiles of HCSs and NiO/HCSs catalyst.

DTG plots (**figure 3.7b**) allowed for the identification of maximum temperatures where carbon decomposition occurred. The DTG plot of HCSs shows a broad peak at 566 °C and a small peak at 665 °C, which is attributed to the decomposition of graphitic carbon. Two notable decomposition peaks were observed for NiO/HCSs catalyst. The first decomposition peak at 189 °C is attributed to trace amounts of nickel salt that remained after calcination and the peak at 555 °C is caused by a graphitic carbon. The thermal stabilities of the NiO/HCSs and HCSs are nearly the same, which indicates that the decomposition of HCSs is not affected by the Ni.

3.3.2. Characterization of NiO@HCSs catalyst

3.3.2.1. Morphology analysis of NiO@HCSs catalyst

3.3.2.1.1. Morphology analysis of the catalyst using a silica template

In our initial attempts to encapsulate Ni nanoparticles inside the HCSs, silica spheres were used as a template. The encapsulation of Ni using a silica template was firstly attempted by synthesizing silica spheres using the Stöber method [15, 20]. The nickel NPs were then loaded onto the pristine silica to obtain NiO@SiO₂. In another method, NiO@SiO₂ was coated with a second silica layer to form SiO₂@NiO@SiO₂. The synthesized materials were then placed in a CVD reactor for carbonization. Toluene was used as a carbon source to form a carbon layer on top of the silica to give SiO₂@C. The composite was then etched with HF to remove the silica template and form HCSs. The same procedure was performed to obtain NiO@HCSs-1 (from NiO@SiO₂ composite) and NiO@HCSs-2 (from SiO₂@NiO@SiO₂ composite).

Scanning electron microscopy (SEM) was used to assess the surface morphology of the as-prepared samples. **Figure 3.8a** shows monodispersed pristine silica spheres with an average diameter of 461 ± 18 nm. The pristine silica displays a spherical shape with smooth surface morphology. **Figure 3.8b** shows nickel decorated on the surface of silica with a flower-like morphology (diameter of 522 ± 22 nm). **Figure 3.8c** shows Ni encapsulated with a second layer of silica. The diameter of $\text{SiO}_2@\text{NiO}@\text{SiO}_2$ was found to be 221 ± 10 nm, which is lower than expected. The observed reduction in diameter after the second coating with silica was due to ammonia solution dissolving some nickel and silica from the Ni/SiO_2 resulting in a smaller and less regular spherical morphology.

Figure 3.8d-f shows the HCSs materials obtained after the removal of the silica template. An SEM image of the HCSs with a hollow structure is shown in figure 3.7d. After encapsulation of Ni inside the HCSs, the average diameter of HCSs was about 430 ± 11 nm and nickel nanoparticles had a diameter of 29 ± 12 nm. In addition, carbon nanofibers (CNFs) ($d = 74 \pm 5$ nm, inset in **figure 3.8e**) with a straight morphology were observed on some sites of the HCSs (see TEM image of this morphology in **Appendix A, figure S3.1**). **Figure 3.8f** shows hollow carbon spheres with a diameter of 215 ± 6 nm and spherical morphology.

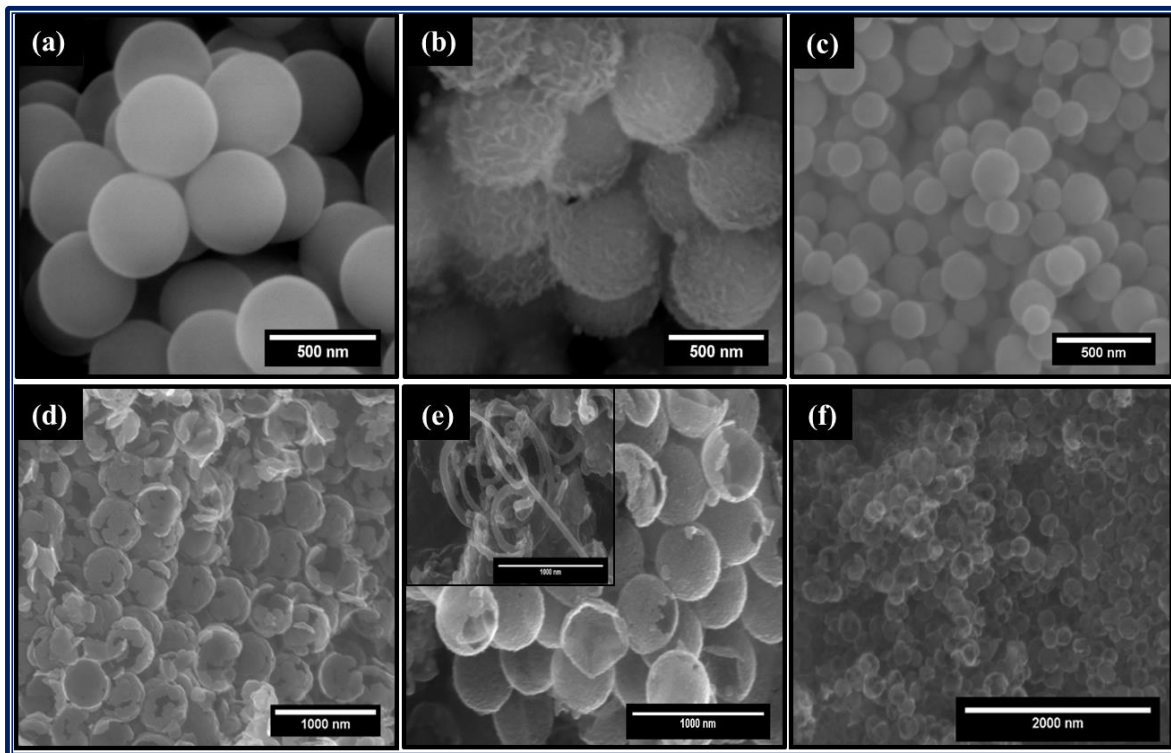


Figure 3. 8: SEM images of (a) pristine silica, (b) $\text{NiO}@\text{SiO}_2$, (c) $\text{SiO}_2@\text{NiO}@\text{SiO}_2$, (d) HCSs, (e) $\text{NiO}@\text{HCSs-1}$ and (f) $\text{NiO}@\text{HCSs-2}$.

The TGA data (shown in **Appendix A: figure S3.2**) revealed a Ni loading of < 5 wt% using the single layer of SiO₂ whilst the encapsulation of Ni with a second silica layer resulted in a low loading (< 2 wt%) of Ni nanoparticles. The BET analysis (shown in **Appendix A; Table S3.1**) also showed low surface areas after coating with a silica layer. The obtained surface areas were 166 ± 4 and 61 ± 1 m²/g for NiO@HCSs-1 and NiO@HCSs-2, respectively. The observed low loadings and surface areas are due to HF etching upon silica removal. Thus to avoid etching of Ni nanoparticles by HF and formation of carbon nanofibers after carbonization as a result of annealing, polystyrene spheres were used as a template.

3.3.2.1.2. Morphology analysis of the NiO@HCSs catalyst with different Ni loading using PSs template

The encapsulation of Ni inside HCSs was achieved by depositing Ni nanoparticles on the PSs template as shown in **figure 3.9**. The composite was then coated with a carbon layer of resorcinol formaldehyde (RF) and placed inside a CVD reactor to decompose the PSs template and to carbonize the carbon layer. A similar procedure was used in other studies for the preparation of metal encapsulation in HCSs [19-20, 29-31].

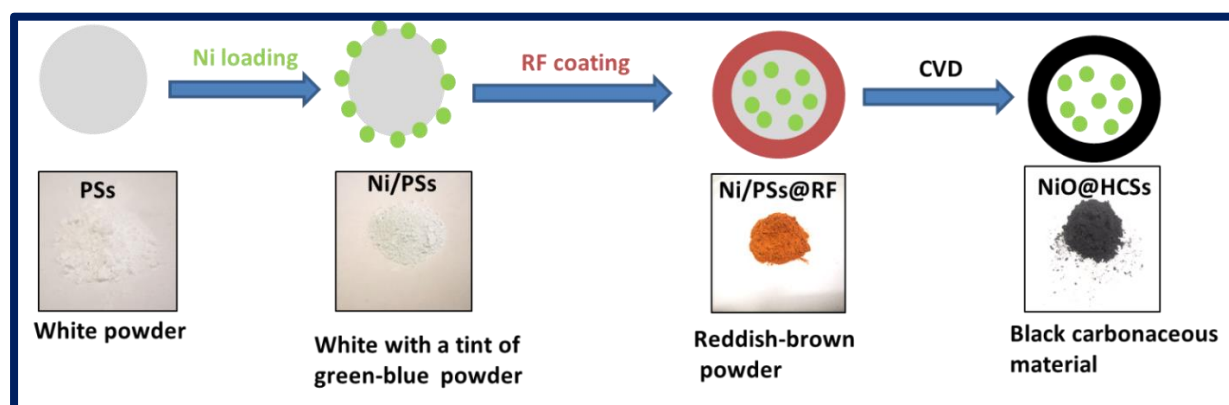


Figure 3. 9: Schematic representation of the synthesis of NiO@HCSs catalyst.

The representative TEM images of nickel nanoparticles encapsulated inside hollow carbon spheres (NiO@HCSs) with different Ni loadings (0.5 wt%, 5 wt%, and 10 wt%) are shown in **figure 3.10**. The TEM micrographs of the catalysts reveal the presence of nickel loaded inside the HCSs support with minimal Ni agglomeration compared to loading the metal outside HCSs after annealing (**see section 3.3.1**).

An attempt to load Ni inside HCSs at a higher loading (10 wt%) gave trace amounts of Ni nanoparticles on the exterior surface of the HCSs but very little Ni was seen inside the HCSs (**figure 3.10 a**, denoted as 10 wt% _trial). This resulted from a huge loss of the Ni during the

filtration due to poor interaction between the Ni and the PSs. To try to circumvent the filtering problem at a 10 wt% loading, the Ni compound was deposited on PSs for a longer time (3 h) before hydrazine addition (detailed procedure described under **section 3.2.3**). This method resulted in the formation of large quasi-spherical Ni nanoparticles inside the hollow cavity (**figure 3.10b**), which is attributed to possible sintering that occurred during the stirring of the sample for a longer time. As a result of this, we opted to reduce the loading to 0.5 wt% and 5 wt% loadings. The filtration problem still prevailed for a 5 wt% loading process although in this case the amount of Ni NPs deposited on the HCSs increased. At 5 wt% and 10 wt% Ni loadings, the Ni NPs were found to be deposited outside and inside the HCSs with average diameters of 51 ± 12 and 22 ± 5 nm for 10 wt% and 5 wt% Ni loadings, respectively. However, at 0.5 wt% loading, almost all Ni NPs reside inside the HCSs and have an average particle size diameter of 12 ± 8 nm. The TEM images (**figure 3.10 c, d**) indicate no significant change in the morphology of the HCSs occurred after Ni loading (see **Table 2.2**). In contrast, a change in the HCSs morphology occurred after 10 wt% loading, attributed to the large particles that formed before the carbon coating.

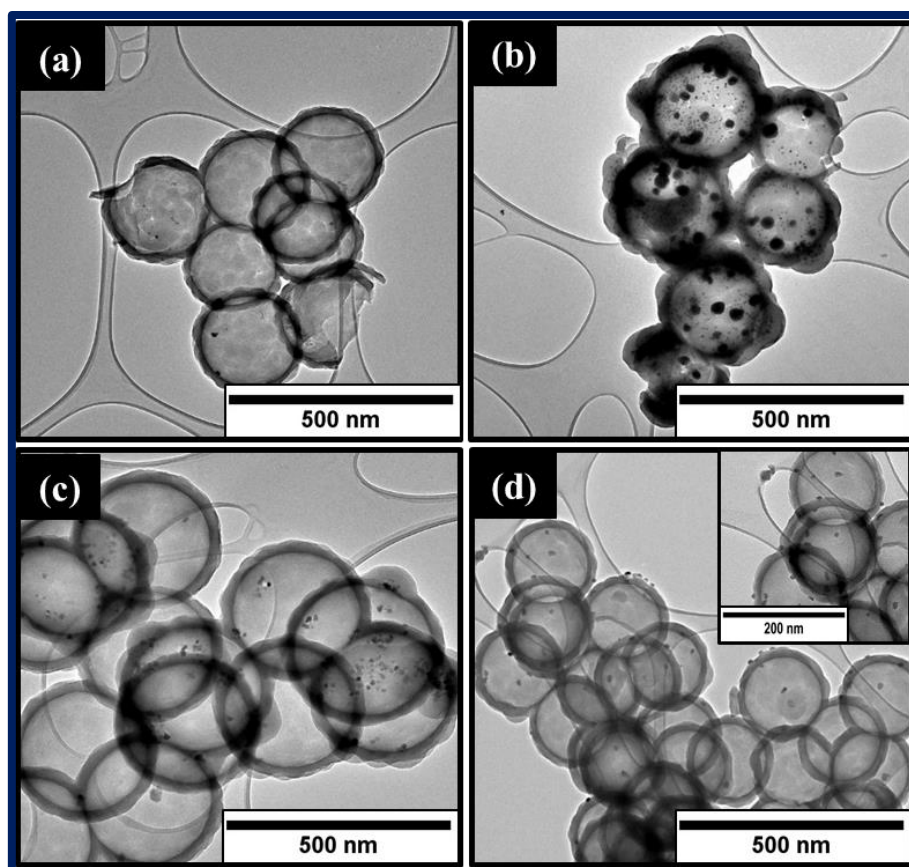


Figure 3. 10: TEM images of (a) 10 wt% NiO@HCSs , (b) 10 wt%, (c) 5 wt% and (d) 0.5 wt% NiO@HCSs catalysts.

Table 3. 2: Calculated particle sizes of the HCSs (shell thickness and inner diameter) and Ni nanoparticles

Sample	Shell thickness (nm)	Inner diameter (nm)	Crystallite size (nm)
HCSs	55 ± 10	433 ± 42	-
0.5 wt% NiO@HCSs	54 ± 12	438 ± 22	12 ± 8
5 wt% NiO@HCSs	55 ± 16	381 ± 121	22 ± 5
10 wt% NiO@HCSs	102 ± 31	478 ± 52	51 ± 12

3.3.2.2. XRD analysis of the NiO@HCSs catalysts

The crystallographic composition of the as-prepared NiO@HCSs catalysts was studied using X-ray diffraction (XRD). **Figure 3.11** shows the XRD patterns of NiO@HCSs with various nickel loadings inside the HCSs. The spectrum of the hollow carbon sphere support is shown in **figure 3.3** for reference. It was observed that upon loading Ni inside the HCSs, a slight shift in the carbon (002) diffraction peak to lower angles with an increase in nickel loading was observed. This is attributed to the disturbances that occurred in the support structure upon Ni loading. No obvious carbon peak was observed for 10 wt% NiO@HCSs, due to the large peak of the Ni particles overshadowing the carbon peak.

The 5 wt% NiO@HCSs diffraction spectrum revealed four small peaks at 37°, 43°, 44° and 63°, respectively. These were indexed as (111), (200), (111) and (220) planes of NiO/Ni crystallites with an fcc structure [34]. Similarly, NiO/Ni diffraction peaks were observed at the same peak position as described in **section 3.3** (NiO/HCSs_annealed sample XRD spectra) for 10 wt% NiO@HCSs. It is however noted that, as the metal loading increases, sharp and intense peaks are observed for Ni relative to the NiO peaks. This means that more NiO particles were converted to metallic Ni in the reaction. This presumably occurred when the Ni salt was reduced with hydrazine in the reduction step. Alternatively, the NiO formed inside the HCSs was reduced by the carbon (HCSs) which acted to limit the diffusion of air through the pores to reoxidize the Ni. Ravat *et al.* [39] suggested that at T > 400 °C, carbon support reacts with

the oxygen attached to the metal and releases it as CO₂, thereby reducing the metal into its metallic form. Similar results were also observed in [38, 40].

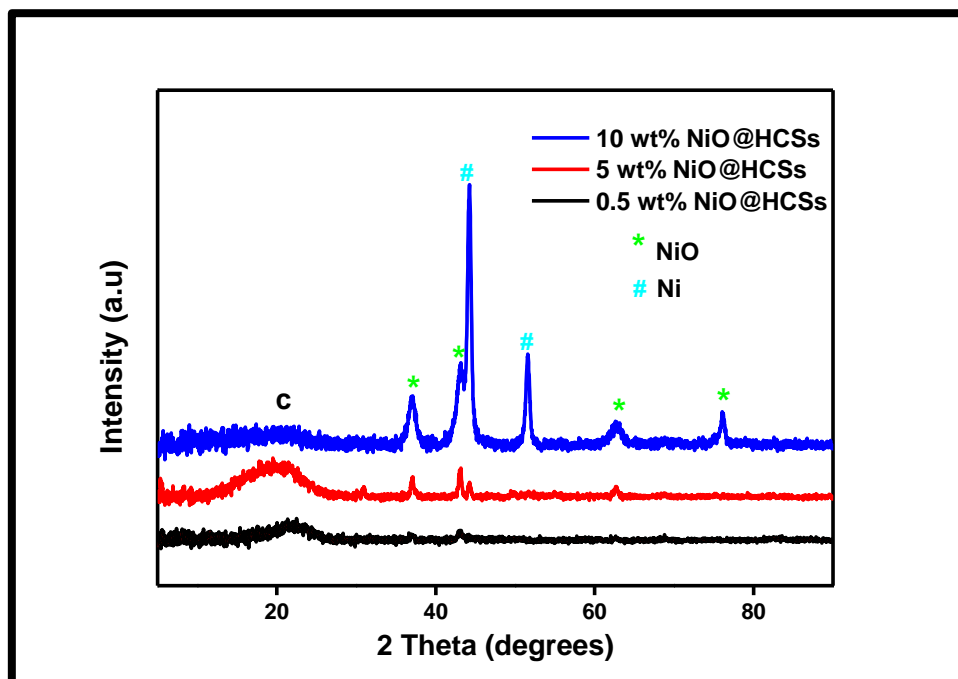


Figure 3. 11: XRD patterns of 0.5 wt%, 5 wt%, and 10 wt% NiO@HCSs catalysts.

The Ni crystallite sizes were determined using the Scherrer equation. The approximate crystallite sizes of NiO were found to be 9.8 nm, 20.2 nm and 25.1 nm for 0.5 wt%, 5 wt%, and 10 wt% loadings, respectively. This data is in agreement with the trend observed in the TEM data although the crystallite sizes measured by XRD were slightly smaller. The Ni crystallites observed were determined to be 3.4 nm and 34.3 nm for 5 wt% and 10 wt% loadings, respectively.

3.3.2.3. TPR studies of the NiO@HCSs catalysts

Temperature programmed reduction (TPR) was carried out on NiO@HCSs catalysts to further evaluate the effect of metal loading on the extent of interaction between nickel and the HCSs support. The TPR profiles of NiO@HCSs catalysts at different loadings are shown in **figure 3.12**. The reduction profile 0.5 wt% NiO@HCSs catalyst is not included as the nickel could not be detected by the instrument as a result of the low nickel loading. A broad reduction peak for 5 wt% NiO@HCSs was noted at 281 °C, attributed to a single-step conversion of NiO to metallic Ni as shown in equation 1 below. As the metal loading was increased to 10 wt%, two reduction peaks were observed at *155 °C and 269 °C. The presence of multiple peaks has been reported in the literature for the reduction studies of NiO at high loadings [34]. This was

attributed to the existence of different NiO species. However, the possibility of this explanation was disregarded in this study since the XRD data revealed no indication of other phases of NiO or Ni.

However, Zangouei *et al.* [35] suggested that the appearance of the low-temperature reduction peak is due to the reduction of bulk NiO species with different extent of interaction with the support.

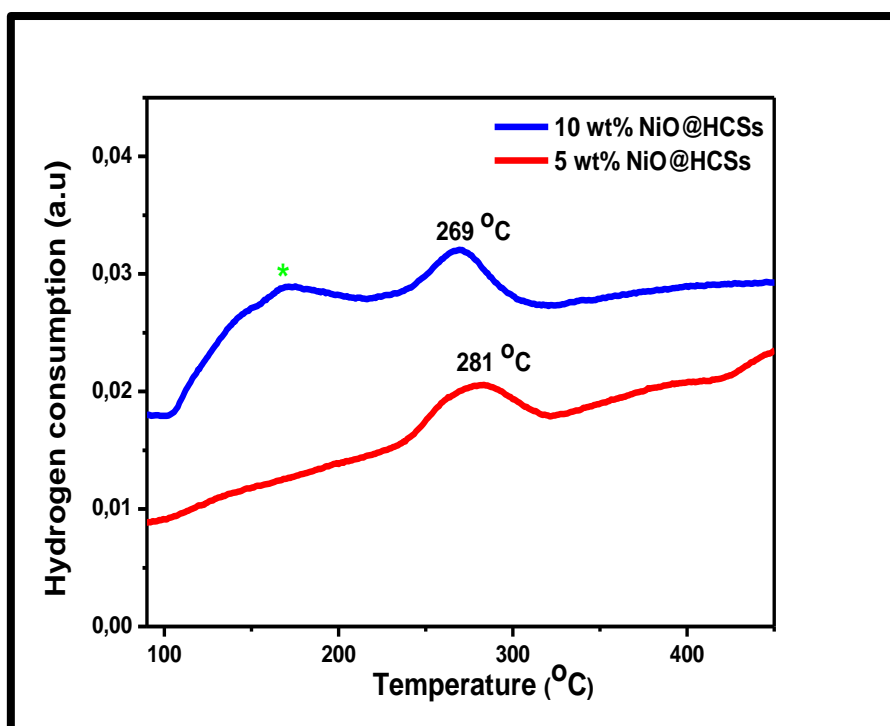


Figure 3. 12: TPR profiles of 5 wt% and 10 wt% NiO@HCSs catalysts.

Furthermore, it was observed that in our study, as the Ni content increased, the reduction peak shifted to a lower temperature. This could be attributed to possible weak interactions between the nickel nanoparticle and HCSs support as the carbon shell is covered with more Ni as the loading increased. Consequently, these result in an easier reduction of the metal. The decrease in the metal-support interactions as the metal loading increases has been reported in the literature [34, 36].

It was noted that Ni confinement inside HCSs increases the reducibility of the Ni particles compared to loading Ni outside the HCSs due to blockage of the HCSs pores by Ni particles.

The observed data corroborates the BET data obtained for both NiO/HCSs and NiO@HCSs catalysts.

3.3.2.4. BET analysis of the NiO@HCSs catalysts

To assess the effect of Ni encapsulation using different Ni loadings on the surface area and porosity of the HCSs, BET analysis was carried out. The N₂ adsorption-desorption isotherms of the NiO@HCSs catalysts are shown in **figure 3.13**. The isotherms exhibit a hysteresis loop with type II/IV isotherm behavior indicating the presence of both micropores and mesopores [42]. The surface area values obtained are summarised in **Table 3.3**. The surface area analysis revealed a slight change in the HCSs surface area after 0.5 wt% loading compared to the pristine HCSs (see **Table 3.1** for reference). The decreasing effect is rationalized by the closing of the micropores upon metal loading leading to a decrease in the pore volume of the HCSs. However, an increase in surface area was noted for 5 wt% NiO@HCSs catalyst. This was not expected, and no explanation can be given for this finding. The 10 wt% NiO@HCSs catalyst portrayed a sharp decrease in surface area. This could be due to metal nanoparticles blocking the pores of HCSs as the nickel loading is increased thereby resulting in the pores coverage and a reduced surface area. The BET data is consistent with the TEM results which indicated large particles of Ni which could block the mesopores.

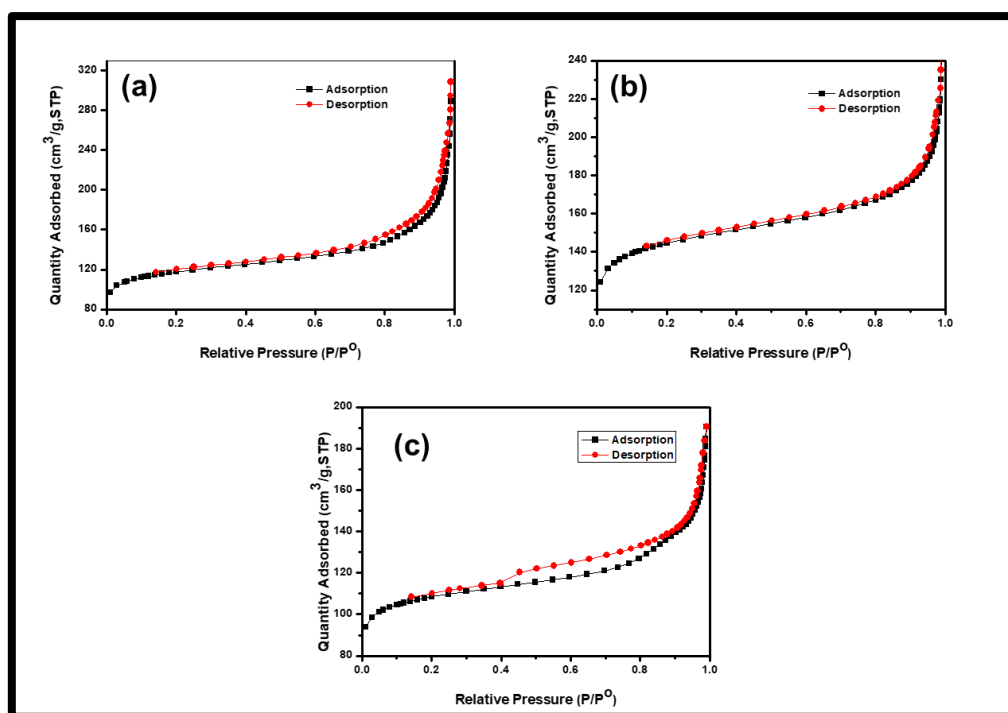


Figure 3. 13: N₂ adsorption-desorption isotherms of (a) 0.5 wt%, (b) 5 wt% and (c) 10 wt% NiO@HCSs catalysts.

The pore size distribution curves of the NiO@HCSs catalysts are shown in **figure 3.14** and pore sizes were calculated by the BJH method. From the distribution plots, it is observed that the as-synthesized catalyst exhibits a narrow pore size distribution with an average pore size between 3-5 nm indicating the mesoporous nature of the materials. Micropores were also observed which decreased in the amount on the addition of a larger amounts of Ni particles. The change in the pore volume reflected this effect.

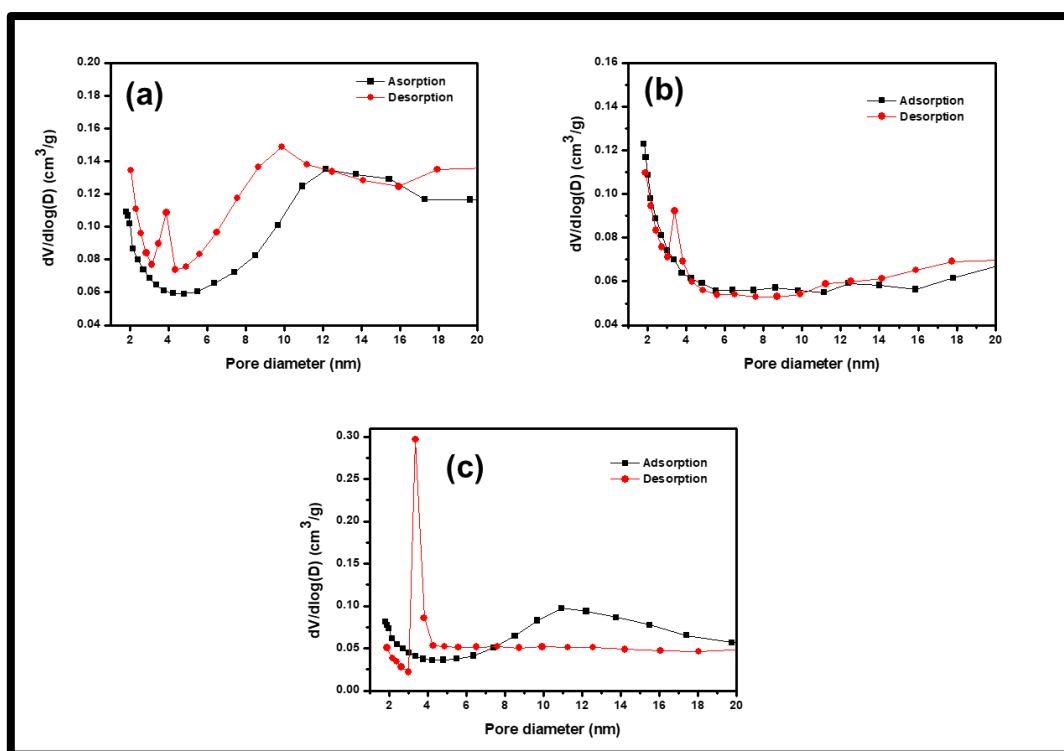


Figure 3. 14: Pore size distribution curves of (a) 0.5 wt%, (b) 5 wt% and (c) 10 wt% NiO@HCSs catalysts.

Table 3. 3: Textural properties of the as-synthesized NiO@HCSs catalysts

Type of sample	BET Surface Area (m ² /g)	Pore volume (cm ³ /g)	Pore diameter (nm)
0.5 wt% NiO@HCSs	381	0.33	4.7
5 wt% NiO@HCSs	464	0.19	3.1
10 wt% NiO@HCSs	348	0.15	3.3

3.3.2.5. TGA analysis of the NiO@HCSs catalysts

TGA analysis was done to assess the influence of metal loading on the thermal stability of HCSs and to confirm the Ni loading on the as-synthesized NiO@HCSs catalysts. The TGA-DTG plots recorded for NiO@HCSs catalysts with different loadings are presented in **figure 3.15**. In **figure 3.15a**, the NiO@HCSs catalysts gave residual masses of 0.3 wt%, 4.6 wt% and 6.2 wt% for 0.5 wt% NiO@HCSs, 5 wt% NiO@HCSs and 10 wt% NiO@HCSs catalysts, respectively. This residue is attributed to NiO. The decrease in the percentage loading from the expected amount is due to the loss of Ni particles upon filtering of the NiO/PSs sample before carbonization. All three catalysts gave similar thermal stabilities.

The DTG plots in **Figure 3. 15b** indicates that the catalyst has a minor effect on the thermal decomposition of the HCSs. The decomposition temperatures of the NiO@HCSs are summarized in **Table 3.4**. A general decrease in the thermal stability of the HCSs support was observed after the incorporation of the Ni particles in the HCSs framework. The decomposition temperature of the HCSs was 592 °C to 560 °C and 548 °C for 0.5 wt% NiO@HCSs, 5 wt% NiO@HCSs and 10 wt% NiO@HCSs, respectively. The decrease in the thermal stabilities can be attributed to the ability of metal particles to act as a poor catalyst for the carbon oxidation reactions. Alternatively, due to the higher loading, the particles generate defects on the carbon shell and this results in compromised thermal stability.

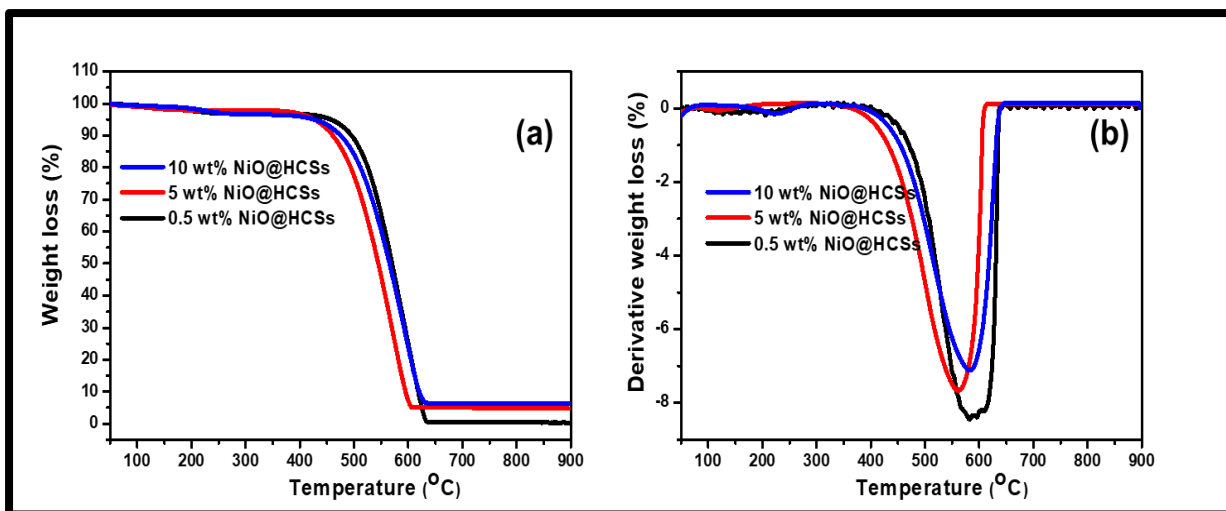


Figure 3. 15: Shows percentage weight loss of NiO@HCSs catalyst. (a) TGA plots of 0.5 wt%, 5 wt% and 10 wt% NiO@HCSs and (b) DTG plots of 0.5%, 5 wt% and 10 wt% NiO@HCSs.

Table 3. 4: Summarizes the decomposition temperature of NiO@HCSs catalysts

Sample	Decomposition Temperature (°C)
0.5 wt% NiO@HCSs	592
5 wt% NiO@HCSs	560
10 wt% NiO@HCSs	548

Conclusions

In this chapter, Ni was successfully deposited on both the outside and the inside of the HCSs by an HDP method. It was noted that annealing of the NiO/HCSs at 800°C resulted in Ni particle agglomeration whilst annealing the encapsulated Ni at 600°C revealed minimal agglomeration. It was observed that Ni does not catalyze the oxidation of carbon in the NiO/HCSs catalyst as observed from TGA data. Nickel in the NiO/HCSs catalyst is present as NiO and in the NiO@HCSs catalyst at high Ni loading appears mainly as Ni metal, as detected by XRD studies. However, some NiO formed inside the HCSs as seen by TPR studies and the XRD data for NiO@HCSs catalysts. The BET data for NiO/HCSs and NiO@HCSs revealed that the Ni does not have a major effect on the HCSs surface area and pore size. However, changes in the pore volume were observed as the Ni loading increased. Also, TPR revealed data revealed that as the metal loading increased, the reduction temperature of the Ni decreased, which is attributed to weak metal-support interactions.

References

1. N.T. Suramwar, S.R. Thakare, N.T. Khaty, *Synthesis and Reactivity in Inorganic, Metal-Organic and Nano-Metal Chemistry*, 43 (1) (2013) 57-62.
2. M. Kooti, L. Matouri, *Chemistry of Materials*, 2 (1) (2014) 37-42.
3. X. Wang, L. Li, Y. Zhang, S. Wang, Z. Zhang, L. Fei, Y. Qian, *Crystal Growth and design*, 6 (9) (2006) 2164-2165.
4. N.H. Idris, J. Wang, S. Chou, C. Zhong, M. Rahman, H. Liu, *Journal of Materials Research*, 26 (7) (2011) 860-866.
5. A. Rahdar, M. Aliahmad, Y. Azizi, *Journal of nanostructures*, 5 (2015) 145-151.
6. L. Xiang, X.Y. Deng, Y. Jin, *Scripta Materilia*, 47 (2002) 219-224.
7. D. Xu, H. Lv, B. Liu, *Frontiers in Chemistry*, 6 (550) (2018) 1-14.
8. G. Dyker, *Angewandte Chemie International Edition*, 38 (1999) 1698-1712.
9. J.F. Hartwig, *Angewandte Chemie International Edition*, 37 (1998) 2046-2067.
10. M.K. Corbierre, N.S. Cameron, M. Sutton, S.G. Mochirie, *American Chemical Society*, 123 (2001) 10411-10412.
11. M. Moreno-Manas, R. Pleixats, *Accounts of Chemical Research*, 36 (2003) 638-643.
12. J.M. Campelo, D. Luna, R. Luque, *ChemSusChem*, 2 (2009) 18-45.
13. L. Jin, B. Liu, S.S. Duay, J. He, *Catalysis*, 7 (44) (2017) 1-5.
14. R.M. Crooks, M. Zhao, V. Chechik, L.K. Yeung, *Accounts of Chemical Research*, 34 (2001) 181-190.
15. T.N. Phaahlamohlaka, D.O. Kumi, M.W. Dlamini, L.L. Jewell, N.J. Coville, *Catalysis Today*, 275 (2016) 76-78.
16. T.T. Nguyen, P. Serp, *ChemCatChem*, 5 (2013) 3595-3603,
17. E. Castillejos, P.J. Debouttiere, L. Roiban, *Angewandte Chemie International Edition*, 48 (2009) 2529-2533.

18. A.B. Fuertes, M. Sevilla, T. Valde-Solis, P. Tartaj, *Chemistry of Materials*, 19 (2007) 5418-5423.
19. T.N. Phaahlamohlaka, *Synthesis of Carbon nanofibers and their subsequent use as catalyst supports for Fischer-Tropsch synthesis*, MSc Dissertation, University of the Witwatersrand, Johannesburg, (2013).
20. B.K. Mutuma, *Synthesis and characterization of Solid, Hollow, Core-shell and worm-like carbon nanostructures for Application in Organic Photovoltaic Devices and Chemical Sensors*, Ph.D. Thesis, University of the Witwatersrand, Johannesburg, (2016).
21. L.A. Garcia-Cerda, *Journal of Nanomaterials*, 201 (2011) 1-6.
22. M.S. Maubane, M.A. Mamo, *Journal of Synthetic Materials*, 162 (2012) 2307-2315.
23. J.H. Kaufman, S. Metin, *Journal of American Physical Society*, 39 (1989) 13053-13059.
24. F. Ghaemi, L.C. Abdulla, P. Tahir, *Polymers*, 8 (2016) 381.
25. X. Wang, J. Zhuang, Q. Peng, Y. Li, *Nature*, 437 (2005) 121-124.
26. X. Wang, X. Li, X. Sun, F. Li, Q. Liu, Q. Wang, *Journal of Materials Research*, 21 (2011) 3571.
27. S.V. Ganarachi, R. Bhat, R. Deshpande, A. Venkataraman, *Research in Science and Technology*, 4 (4) (2012) 50-59.
28. J. Chattopadhyay, T.S. Pathak, R. Srivastava, A.C. Singh, *Electrochimica Acta*, 167 (2015) 429-438.
29. X. Bo, J. Bai, J. Ju, L. Guo, *Journal of Power Sources*, 196 (2011) 8360-8365.
30. C.P. Li, Y.-W. Chen, *Thermochimica Acta*, 256 (1995) 457-465.
31. Y. Hong, I.A Choi, W.S Seo, *Scientific Reports*, 8 (2018) 7469.
32. K. Wilgosz, X. Chen, K. Kierzek, J. Machnikowski, R.J. Kalenczuk, E. Mijowska, *Nanoscale Research Letters*, 7 (2012) 269.
33. F. Cheng, V. Duponta, M.V. Twigg, *Applied Catalysis A: General*, 527 (2016) 1-8.

34. S. Sajid, A.M. Elseman, D. Wei, J. Ji, S. Dou, H. Huang, P. Cui, M. Li, *Nano Energy*, 55 (2019) 470-476.
35. M. Zangouei, Z.A. Moghaddam, M. Arasteh, *Chemical Engineering Research Bulletin*, 14 (2010) 97-102.
36. A. Romero, A. Garrido, A. Nieto-Márquez, A.R. de la Osa, A. de Lucas, J.L. Valverde, *Applied Catalysis*, 319 (2007) 246-258.
37. U. Holzwarth, N. Gibson, *Nature Nanotechnology*, 6 (9) (2011) 534.
38. V. Ravat, I. Nongwe, R. Meijboom, G. Bepete, N.J. Coville, *Journal of Catalysis*, 305 (2013) 36-45.
39. V. Ravat, I. Nongwe, N.J. Coville, *ChemCatChem*, 4 (2012) 1930.
40. P.V. McKinney, J. Am, *American Chemical Society*, 54 (12) (1932) 4498-4504.
41. F.P. Hu, Z. Wang, Y. Li, C. Li, X. Zhang, P.K. Shen, *Journal of Power Sources*, 177 (2008) 61-66.
42. C. Weidenthaler, *Nanoscale*, 3 (2011) 792-810.

CHAPTER 4

Synthesis of CNFs over Ni/HCSs and Ni@HCSs catalysts using acetylene as a carbon source

4.1. Introduction

Among the members of structured nanocarbons, there has been an increasing thrust in carbon nanofibers (CNFs) in the research world [1]. The continuous interest in synthesis and study of these materials originates from their novel physiochemical properties such as having excellent mechanical strength, high resistance towards strong acids and bases and high electrical conductivity [2]. These peculiar properties render them diverse applications such as in fuel cells, sensors, and for the reinforcement of composites amongst others [1, 3]. The commonly used method to synthesize CNFs is the chemical vapour deposition (CVD) [3-7]. The synthesis of CNFs in a CVD reactor is achieved by the pyrolysis of a carbon-containing gas such as methane (CH_4) [2], ethylene (C_2H_4) [4], carbon monoxide (CO) [5], etc. that decomposes over a metal catalyst (such as Ni, Cu, and Fe) surface [6]. Among these well-documented carbon-containing gases, acetylene has also proven to be an ideal hydrocarbon for the growth of carbon nanofibers and has long been studied. Qin *et al.* [7] reported on the synthesis of helical carbon nanofibers (HCNFs) by the decomposition of acetylene over a copper catalyst and found that two helical symmetrical fibers (HCNFs) were formed over a single copper crystal. Studies by Shaikjee *et al.* [8] and Maubane *et al.* [9] also demonstrated the synthesis of HCNFs with different morphologies (linear and helical morphology) over NiO catalyst using acetylene. These studies were conducted using an unsupported Ni catalyst. The synthesis of CNFs from supported metal catalysts using acetylene has also been reviewed [4, 10]. Ren *at.al* [11] synthesized HCNFs by decomposition of acetylene over a copper catalyst supported on traditional supports (SiO_2 , TiO_2 , CuAl_2O_3 , MgO) to assess the effect of metal-support interaction (MSI) on the growth of CNFs. From all these studies, it was noted that the CNFs grown vary in length and diameter and generally this is related to the catalyst size and morphology of the metal catalyst [6-10]. As such, it is essential to have control over the catalyst size and morphology as this has a great impact on the morphology of the CNFs and their potential applications [8, 10]. It has been demonstrated that metal confinement in hollow carbon spheres (HCSs) (as described in Chapter 3) can assist in minimizing the sintering of

metal nanoparticles at high temperatures. It is, therefore, logical to assume that growing CNFs from an encapsulated metal catalyst in a restricted environment can limit their growth and provide control over their morphology. Most recently, Gangatharan *et al.* [12] reported on the concept of building structures from encapsulated metal inside hollow carbon spheres using a copper catalyst with controlled length and morphology. They found that CNFs, including HCNFs grew from the encapsulated copper catalyst. However, to date, no studies have been reported on the synthesis of CNFs inside hollow carbon spheres using a nickel catalyst.

In this present chapter, we report on the synthesis of CNFs inside the HCSs, viewed as a nanoreactor, to allow full confinement of the CNFs grown. The approach we have developed includes the use of a CVD for the synthesis of CNFs. The CNFs were synthesized using the as-prepared NiO@HCSs and NiO/HCSs catalysts (**described in Chapter 3**) for comparison purposes. Also, the influence of reaction parameters (such as temperature, flow rate and reaction time) on the growth of CNFs is discussed.

4.2. Experimental Procedure

4.2.1. Synthesis of NiO/HCSs or NiO@HCSs catalyst

The NiO/HCSs and NiO@HCSs catalysts were prepared as discussed in **Chapter 3** (Experimental section).

4.2.2. Synthesis of CNFs using NiO/HCSs or NiO@HCSs catalyst

CNFs were synthesized using a horizontal single-stage CVD reactor as depicted in **figure 4.1** [5-13]. Typically, 50 mg of the as-synthesized NiO/HCSs or NiO@HCSs were uniformly spread over a quartz boat and placed at the center of a quartz tube placed in a horizontal furnace. The furnace was heated at 10 °C/min under the flow of nitrogen gas (100 mL/min). Once the desired reduction temperature was reached (e.g. 450 °C), nitrogen flow was discontinued and hydrogen (100 mL/min) was then passed through the quartz tube for 30 min to activate the catalyst, i.e. from NiO to metallic Ni. The carbon source (C₂H₂) (100 mL/min) together with hydrogen (100 mL/min) were then introduced to the reaction chamber for 5 min. Acetylene flow was discontinued and the furnace was allowed to cool down to room temperature under hydrogen flow. The as-synthesized materials were then retrieved for further characterization. The synthesized materials were denoted as CNF_outside (from NiO/HCSs, 5 wt% Ni loading), CNF_0.5%, CNF_5% and CNF_10% (from NiO@HCSs catalysts with various Ni loadings).

The effect of reaction temperature, time and hydrogen flow rate for the growth of the CNFs was studied.

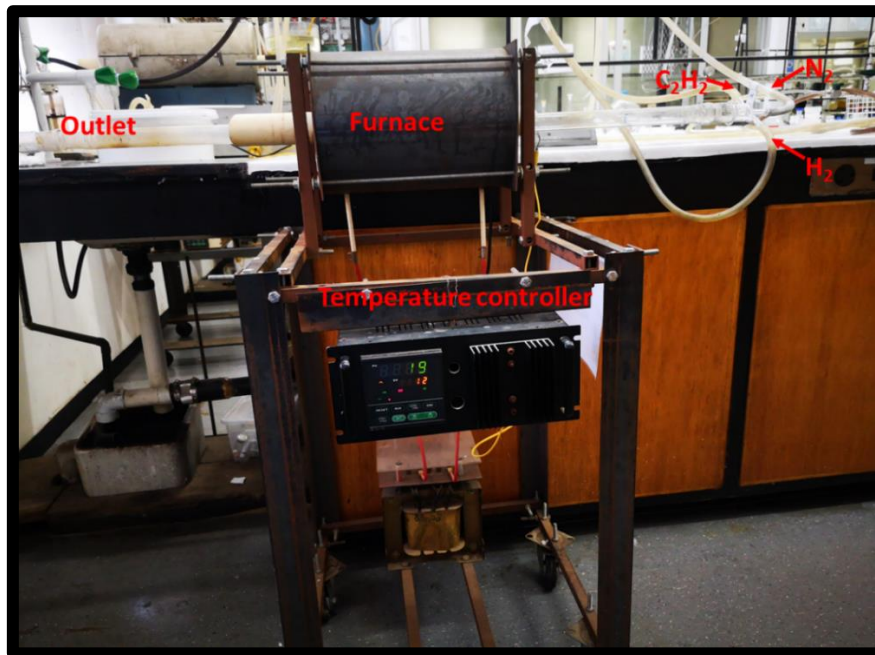


Figure 4. 1: CVD set-up for the synthesis of CNFs using acetylene as a carbon source.

4.2.3. Determination of carbon yield

The carbon percentage yield reported in this study was determined using equation 1 [13].

$$\text{Carbon yield \%} = \frac{(m_{\text{tot}} - m_{\text{cat}})}{m_{\text{cat}}} \times 100 \dots \dots \dots \text{equation 1}$$

where; m_{cat} – mass of the catalyst, and m_{tot} – total weight of the sample after reaction

4.2.4. Characterization techniques

To elucidate the morphology of the as-synthesized CNFs, transmission electron microscopy (TEM), using a FEI Tecnai G² Spirit electron microscope at 120 kV was used. The thermal stability of carbon materials was determined by thermo-gravimetric analysis (TGA) using a Perkin-Elmer STA6000 analyzer. The energy dispersive X-ray spectroscopy (EDS) was used to map out the composition of samples. Powder X-ray diffraction (XRD) was also used to determine the crystallinity of the CNFs. Raman analysis was used to determine the degree of the graphitization of the as-prepared materials.

4.3. Results and discussion

4.3.1. Characterization of CNFs using a NiO/HCSs catalyst: TEM and XRD analysis of the synthesized CNFs

To demonstrate the effect of growing CNFs outside compared to inside, the CNFs were grown from the as-synthesized NiO/HCSs catalyst. Carbon nanofibers were synthesized by catalytic decomposition of C_2H_2 (100 mL/min) at 450°C under H_2 (100 mL/min) over a NiO/HCSs catalyst. The reaction was carried out for 5 min.

TEM micrographs of CNFs grown over NiO/HCSs are shown in **figure 4.2**. The Ni particles after CNF growth revealed a spherical shape, with a disc-like and hexagonal morphology (**figure 4.2.c, d (zoom-in and inset)**). Overall, an enormous growth of CNFs outside the HCSs (*ca.* 105% yield) was observed. The CNFs grown exhibited a straight and helical morphology with variable diameters (ranging from 11-261 nm) and length (*ca.* > 220 nm). However, the dominant CNFs morphology formed could not be concluded as a result of the enormous growth of the CNFs. The observed variations in the fiber morphology and size are closely related to the morphology of the Ni particle. This phenomenon of the catalyst affecting the fiber morphology and size has been observed and discussed by Shaikjee *et al.* [4] and other authors [8, 11-13].

It was also noted that the CNFs grow to all dimensions and diameters due to the sintering of Ni particles at a high temperature, which resulted in the formation of large clusters of Ni agglomerates. As such, it was difficult to visualize and have control over the growth of the carbon nanofibers. CNFs grown outside the HCSs showed similar results with the fibers grown on traditional supports.

Further analysis on the CNF_outside sample was done to study the change in the crystalline structure of HCSs after fiber growth. XRD diffraction pattern (**figure 4.2**) obtained showed no notable peaks for Ni. This is a result of the high content of carbon made that overshadows the Ni content. The two notable diffraction peaks observed at 25° and 44° correspond to the (002) and (100) planes of carbon. The sharp and intense (002) peak can be attributed to the carbon introduced during CNF growth. This observation confirmed the growth of the CNFs.

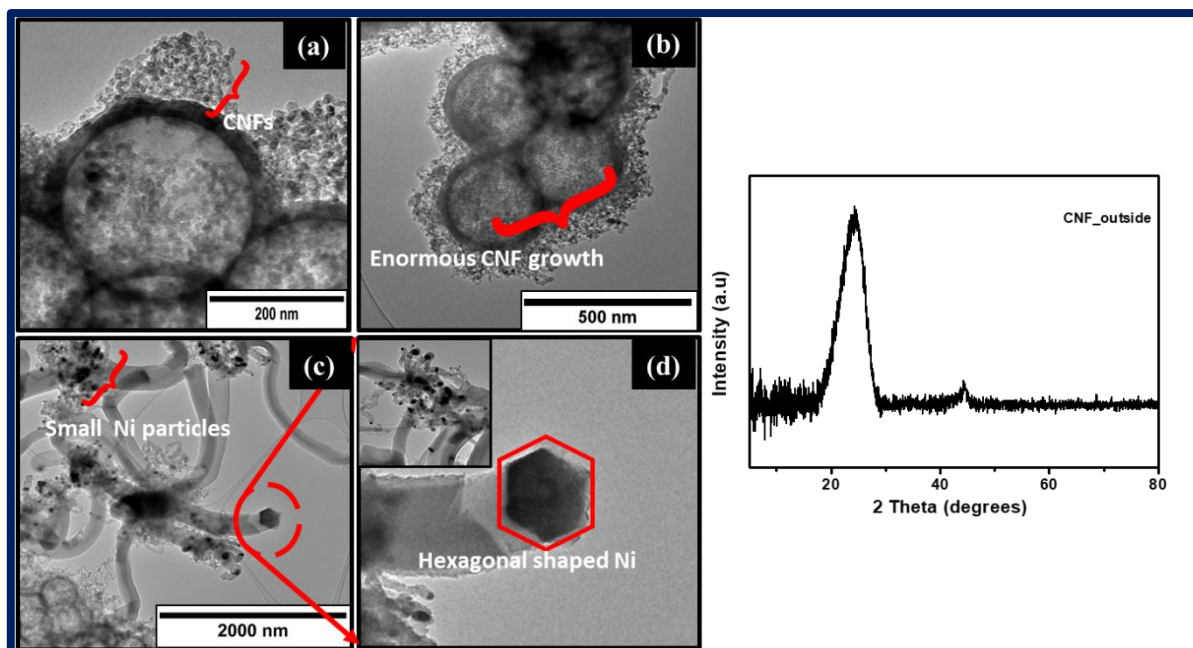


Figure 4. 2: TEM images of CNFs using acetylene over NiO/HCSs (a-d) (synthesized at 450 °C, $H_2/C_2H_2 = 100$ mL/min) and XRD pattern of CNFs.

4.3.2. Characterization of CNFs grown over NiO@HCSs catalyst

4.3.2.1. Synthesis of CNFs over NiO@HCSs catalyst: Effect of metal loading on CNFs growth.

In an attempt to minimize metal agglomeration during fiber growth and possibly control the fiber growth, catalysts were used to grow the CNFs inside the hollow carbon spheres. We, therefore, begin our discussion by first considering the effect of metal loading on the growth of CNFs from NiO@HCSs catalysts. The CNFs were synthesized by placing NiO@HCSs catalysts (0.5, 5, and 10 wt% Ni loadings) in a CVD reactor. Acetylene was passed over the catalyst to allow CNFs growth at 450 °C under the flow of hydrogen (100 mL/min). All reactions were performed for 5 min. During this time, the CNFs grew inside and outside the activated NiO@HCSs catalyst.

Figure 4.3 shows TEM images of CNFs synthesized using NiO@HCSs with different Ni loadings. At 10 wt% (**figure 4.3a**), an enormous growth of CNFs inside/outside the HCSs was observed overshadowing the hollow structure of the HCSs. This might have been as a result of the CNFs emerging from the pores of the HCSs (pore size = 3.5 nm). Also, due to the high loading of the catalyst, some of the Ni may be placed outside of the HCSs and growth on this Ni would have led to the images seen (Refer to **figure 3.10b**). At 5 wt% and 0.5 wt%, the

growth of CNFs seems to be contained inside the HCSs with a few CNF seen growing outside the HCSs. All catalysts produced predominantly two types of straight fibers. The CNFs grew from the tip of Ni catalyst (inset of **figure 4.3c**) while the bidirectional growth of CNFs from a Ni catalyst situated at the center of fiber was also observed. It was noted that, at lower loading, there is a more controlled growth of CNFs.

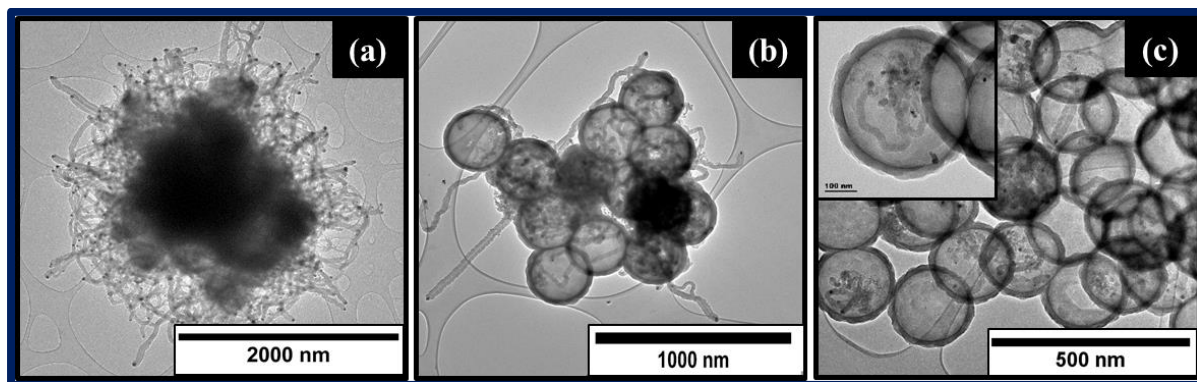


Figure 4.3: TEM images of CNFs using acetylene over NiO@HCSs catalyst, (a) CNF_10 wt%, (b) CNF_5 wt%, and (c) CNF_0.5 wt% (synthesized at 450 °C, H₂/C₂H₂ =100 mL/min, 5 min).

To visualize the CNF growth inside the HCSs, a series of higher magnification images were collected from the 0.5 wt% catalyst. **Figure 4.4** shows CNFs grown inside HCSs from different Ni particles with different sizes. Some HCSs contain Ni particles (average size 14 ± 4 nm) and the CNFs grown give single fiber growth (**figure 4.4.a**, see arrows). This was observed as the dominant growth mechanism of the fibers. However, some particles showed growth from both sides of Ni particle resulting in helical fiber growth (**figure 4.4b, c**). Formation of thinner fibers was also observed inside the HCSs and this was assumed to be a result of the presence of very small (*ca.* < 5 nm) Ni particles. Also, it was observed that some HCSs does not contain Ni particles or CNFs. This is ascribed to some of the Ni nanoparticles not deposited on PSs before carbonization.

Moreover, it was noted that the HCSs act as a barrier for the CNFs grown inside. As such, instead of the CNFs penetrating through the pores of HCSs, they bend along the walls of HCSs as they continue to grow.

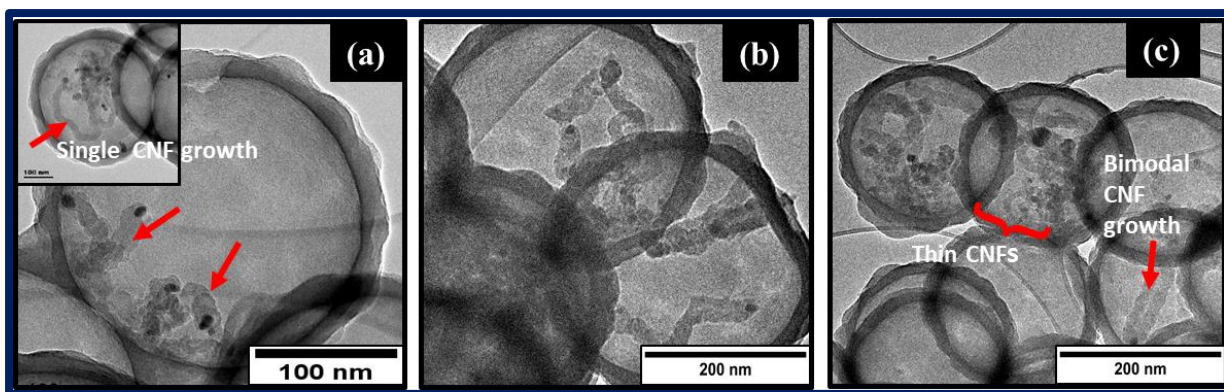


Figure 4. 4: High magnification TEM images of CNFs grown from 0.5 wt% NiO@HCSs catalyst (450 °C, H₂/C₂H₂ =100 mL/min, 5 min).

Although the CNFs appear to be confined inside HCSs (as seen in **figure 4.3 and 4.4**), TEM tilting experiments (**figure 4.5**) were conducted to obtain 3D images of the catalyst using a single axis tilting to confirm that indeed CNFs were grown inside the HCSs. The images from the higher (-) axis could not be attained as the copper grid interfered with the collection angles and only images of a small series of tilt angles were collected. The acquired images were recorded with a tilt series of between -45° to 55° angles. The TEM images obtained show that Ni nanoparticle and CNFs reside inside the HCSs as the tilting angle is varied (see arrows).

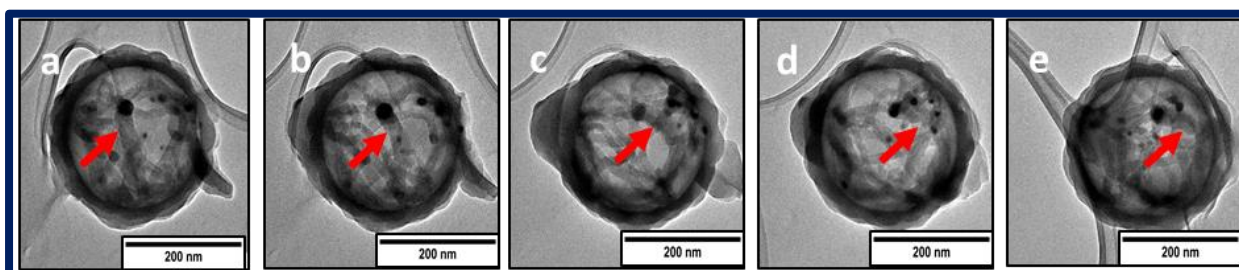


Figure 4. 5: TEM tilting experiment micrographs showing the helix movement in a HCSs nanoreactor, (a) -45° (b) -30° (c) 0° (d) +30° and (e) +55°.

In pursuit of studying the effect of reaction parameters (temperature, growth time and flow rate) on the growth of CNFs, the 0.5 wt% NiO@HCSs catalyst was chosen for further studies. This material revealed a better growth of CNFs compared to other catalysts with a higher loading (as can be seen from TEM micrographs in **figure 4.3**) and the changes in the growth of CNFs can be readily monitored.

4.3.2.2. Synthesis of CNFs over 0.5 wt% NiO@HCSs catalyst: Effect of growth temperature

The influence of the growth temperature on the CNFs growth was evaluated in this section. The CNFs were synthesized by decomposition of acetylene (C_2H_2 , 100 mL/min) over the encapsulated nickel catalyst at different temperatures (250, 300, 350, 400, 450, 500 and 600 °C) in the presence of H_2 (100 mL/min). CNFs were grown for 5 min. After the reactions, the black carbonaceous materials were retrieved and characterized. The products were labelled as CNF_250, CNF_300, CNF_350, CNF_450, CNF_500, and CNF_600 (labelled according to their reaction temperature).

4.3.2.2.1. Morphology analysis: TEM of CNFs grown at different reaction temperatures

The TEM images of CNFs synthesized at different reaction temperatures are shown in **figure 4.6** and **figure 4.7**. **Figure 4.6** shows the CNFs synthesized at low temperatures. At 250 °C, little or no apparent fiber growth is observed. When the temperature was increased to 300 °C, single (one-directional growth of CNF from a Ni NPs) and bilateral (bidirectional fiber) growth is observed (**figure 4.6b**, see arrows). Similar growth was observed at 350 °C. At this temperature, the yield was still low (as determined by the amount of fiber formed) and the fibers grown showed a straight morphology. As seen from the TPR data (**figure 3.12**), the complete conversion of NiO to Ni takes place at temperature ~ above 280 °C. This minimal fiber growth suggests that nickel is still in its oxide form, and Ni has very low activity towards acetylene at low temperatures. The inactivity of Ni catalyst at low temperature was also observed in studies reported on unsupported Ni catalysts by Shaikjee *et al.* [4] and Maubane *et al.* [6].

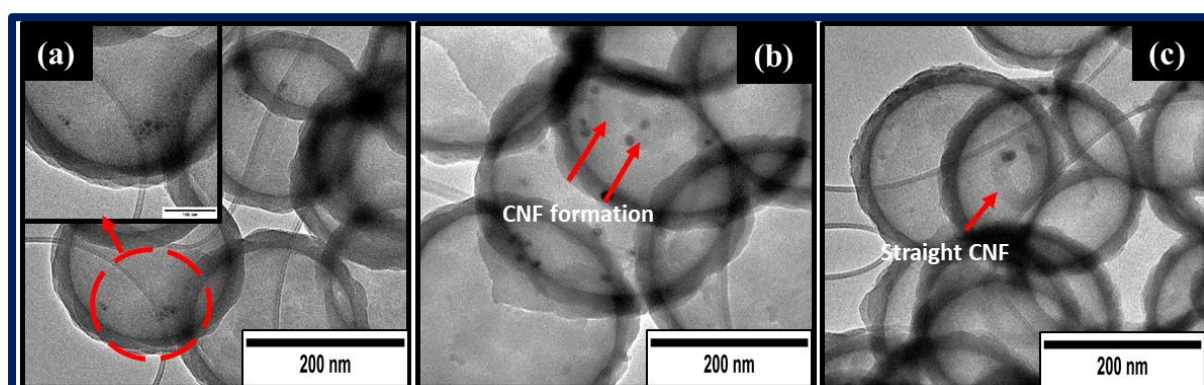


Figure 4. 6: TEM images of CNFs using acetylene over 0.5 wt% NiO@HCSs catalyst at (a) CNF_250, (b) CNF_300 and (c) CNF_350 ($H_2/C_2H_2 = 100$ mL/min, 5 min).

As the temperature was further increased to 450 °C, mono-directional fiber growth from a single Ni grain was dominantly observed. A mixture of both helical and straight fibers was observed. This suggests the presence of different sizes and morphology of the Ni particles upon carbon growth. Studies show that particle sizes of ~ 50 nm often results in the growth of helical morphology, whereas particles with sizes ~100-500 nm tend to form linear/straight CNFs [4, 17]. It should also be noted that, at this temperature, the formation of thin CNFs ($d = 10 \pm 4$ nm) (with a worm-like morphology) were also observed but in low yields (*ca.* 2%). The average diameter of the CNFs synthesized at this temperature was estimated to be 29 ± 7 nm. At 500 °C, a mixture of both thin and thick fibers were formed. This infers that the catalyst fractured into smaller particles and the CNFs ceased to form from these fractured particles. The average diameters were found to be 6 ± 1 nm for the thin and 20 ± 2 nm for the thick fibers. The CNFs synthesized at 600 °C gave a dominance of thinner CNFs with irregular morphology (with a narrow diameter distribution of 11 ± 3 nm). This indicates that, as the temperature was further increased to 600 °C, nickel nanoparticles continued to fracture into smaller particles instead of agglomeration to give much thinner CNFs. Similar observations were reported by Maubane *et al.* [15]. Also, it was evident from the TEM images that the diameter of CNFs is closely related to the diameter of the nickel catalyst.

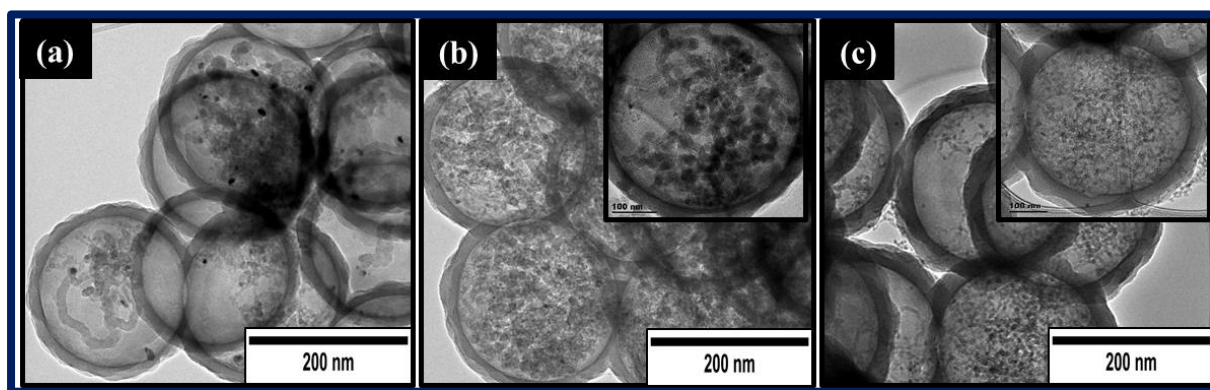


Figure 4. 7: TEM images of CNFs using acetylene over 0.5% Ni@HCSs catalyst at (a) CNF_450, (b) CNF_500 and (c) CNF_600 ($H_2/C_2H_2 = 100$ mL/min, 5 min).

The energy dispersive X-ray spectroscopy (EDS) was used to determine the composition of the as-prepared material (only one sample was used for this analysis as the material consist of the same composition). The EDS spectrum (**Appendix B, figure S4.1**) revealed peaks corresponding to C and Ni elements. This confirmed the presence of Ni in the HCSs.

Figure 4.8 shows the carbon yield as a function of temperature as determined by equation 1 (see section 4.2.3). The trend reveal that the carbon yield increased as the temperature increased. This suggests that as the temperature increases, there are more active Ni sites and thus more fiber growth. Although the maximum fiber yield was obtained at 600 °C, the temperature for the CNFs growth was chosen to be at 450 °C because fewer CNFs were grown at this temperature which allowed easier evaluation of the CNF structure by TEM analysis. This enabled a more facile visualization of the effect of other parameters on the fiber growth. Hence, studies were conducted at this temperature.

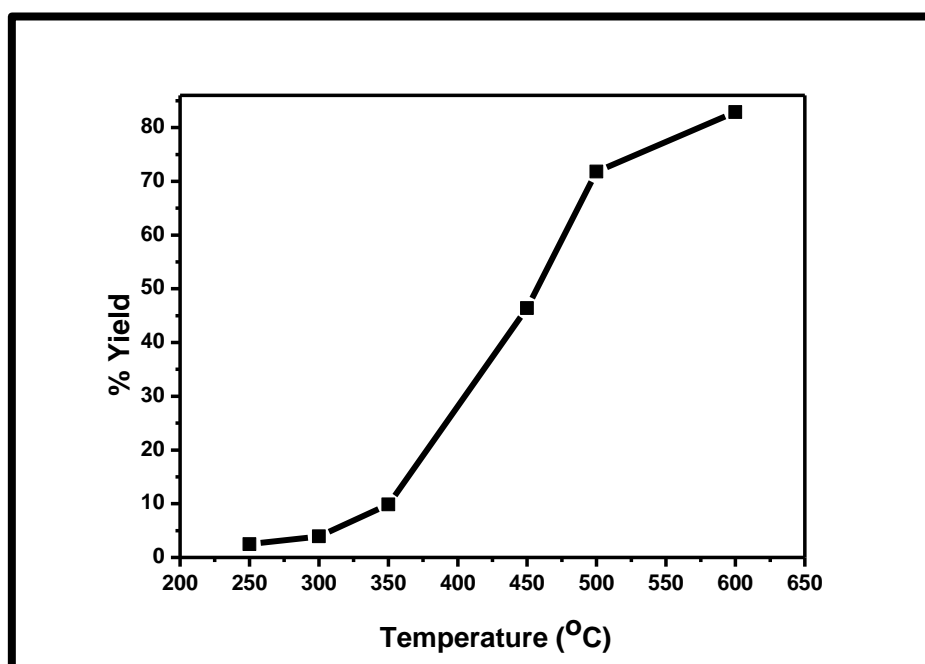


Figure 4. 8: Graph showing % yield of CNFs as the reaction temperature increased.

4.3.2.2.2. XRD of CNFs grown at different reaction temperatures

XRD studies were conducted to evaluate the effect of temperature on the crystallinity of the CNFs. The obtained XRD diffraction patterns are shown in **figure 4.9a and b**. All diffraction patterns show a broad peak in the Bragg angle range 18–28° corresponding to the (002) plane of carbon. As the temperature was increased, there is a slight shift of the carbon peak to the higher 2θ angles, which can be attributed to defects that occurred in the HCSs network as the CNFs growth increased. It is also noted that, as the temperature increased, the carbon peak became sharper and broader. This observation is in agreement with the % yield data which indicated that as the growth temperature increased, the carbon content also increased. Another small peak at $2\theta = 43^\circ$, corresponding to the (100) plane, was observed. This peak also

indicated the presence of CNFs as temperature increased. The Ni peaks were not observed due to low concentration of Ni.

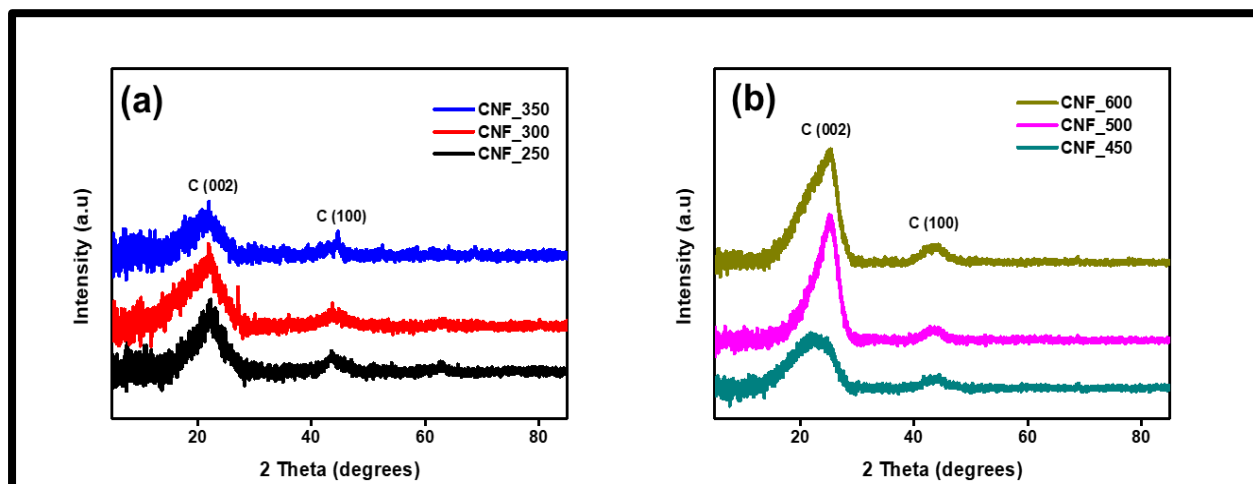


Figure 4. 9: XRD patterns of CNFs grown at different temperatures (reaction conditions: $H_2/C_2H_2 = 100$ mL/min, 5 min).

4.3.2.2.3. Raman analysis of CNFs grown at different reaction temperatures

Raman analysis was used to probe the degree of graphitization of the as-prepared CNFs at different temperatures. **Figure 4.10** shows Raman spectra revealing two broad peaks well-known as the D and the G bands centered at $1330 - 1360\text{ cm}^{-1}$ and $1580 - 1590\text{ cm}^{-1}$ [14]. The presence of the D band can be attributed to the breathing mode of sp^2 carbon atoms and defects in the carbon structure [15]. In addition, the G band is due to the vibration of sp^2 carbon atoms [16]. The ratio of the D and G bands (I_D/I_G) is used to elucidate the degree of order or disorder in the materials. The peak positions of both D and G bands are summarised in **Table 4.1**. The presence of CNFs was confirmed by a slight down-shifting of both the D and G band positions which is attributed to structural deformations and the presence of the disorder within the carbon lattice induced by the incorporated Ni NPs and CNFs in the core of the HCSs. The I_D/I_G of CNFs synthesized at 250, 300, 350 °C show similar crystalline structure with the I_D/I_G of ~ 0.8 . However, upon increasing the temperature to $T = 600$ °C, there is an increase in the I_D/I_G ratio (0.91) which indicates a more disordered carbon being formed. Thus, this suggests that as the temperature is increased the materials are becoming less crystalline.

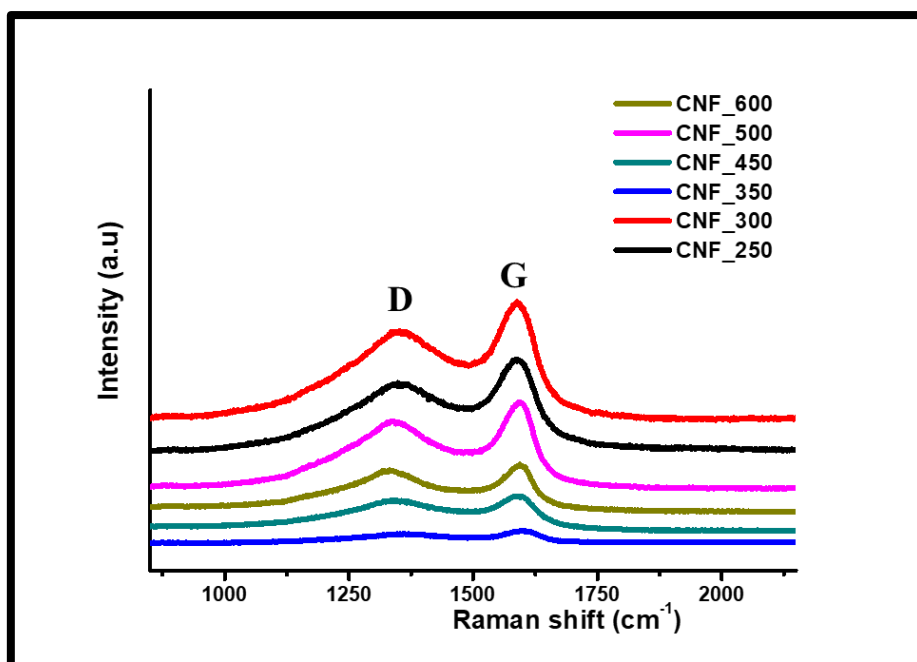


Figure 4. 10: Raman spectra of CNFs grown at different temperatures (H_2/C_2H_2 (100 mL/min, 5 min)).

Table 4. 1: The I_D/I_G ratios of D and G peaks of the obtained CNFs

Material	D band peak position (cm^{-1})	G band peak position (cm^{-1})	I_D / I_G ratio
CNF_250	1351	1584	0.76
CNF_300	1352	1585	0.79
CNF_350	1361	1595	0.76
CNF_450	1344	1585	0.81
CNF_500	1341	1588	0.85
CNF_600	1331	1588	0.91

4.3.2.2.4. TGA analysis of CNFs grown at different reaction temperatures

The CNFs were characterized using TGA analysis to evaluate the effect of growth temperature on the thermal stability of the as-synthesized CNFs. TGA and DTG profiles of CNFs synthesized at different temperatures (250–600 °C) are presented in **figure 4.11** and **figure 4.12**, respectively. The TGA plots (**figure 4.11**) show that the CNFs synthesized at 300 °C–450 °C are thermally stable up to *ca.* 450 °C before decomposition occurs. Similarly, the CNFs

synthesized at 500 °C and 600 °C were stable over the temperature regime 456-565 °C and start to decompose at $T > 570$ °C. In general, the data obtained shows that the thermal stability of the CNFs increased as the temperature increased. Also, it was noted that all samples decomposed completely (*ca.* 0 wt%), suggesting that as CNFs continue growing, the amount of Ni present become negligible.

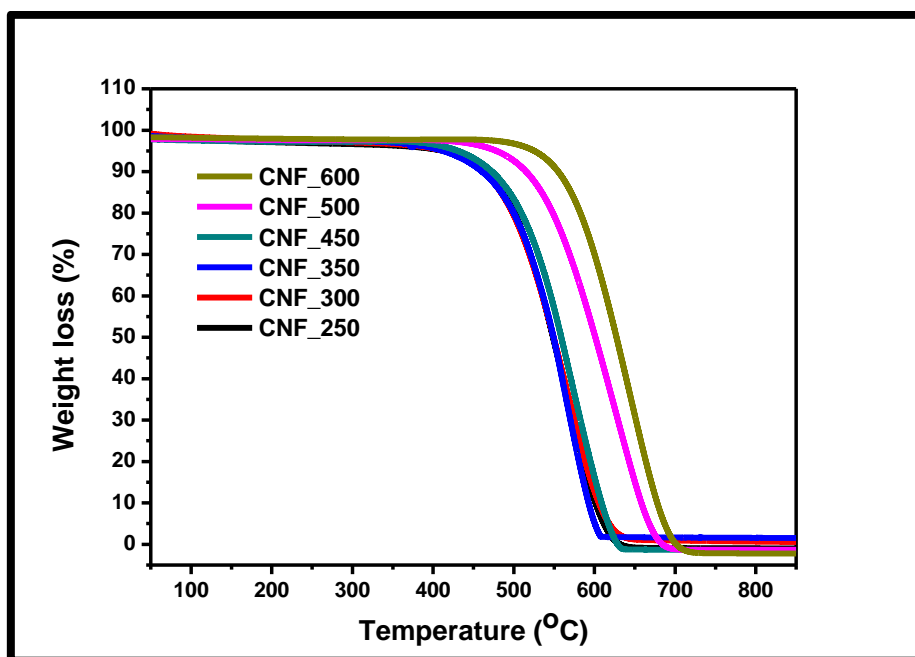


Figure 4. 11: TGA plots of CNFs synthesized at different temperatures (H_2/C_2H_2 (100 mL/min, 5 min)).

The DTG plots depicted in **figure 4.12** and decomposition temperatures are given in **Table 4.2**. **Figure 4.12** shows the oxidation decomposition temperatures of CNFs at different synthesis temperatures. At 300 °C, the DTG plot shows a broad decomposition peak at 565 °C. When the temperature was increased to 350 °C, a sharp and narrower peak was observed. It is suggested that this was due to an introduction of CNFs into the HCSs. It should be noted that this was the temperature where linear CNFs started to form. On further increase in the temperature to 450, 500 and 600 °C, the peak became broad which indicates the presence of defected carbon or carbon with varying dimensions as seen from the TEM data.

In comparison with the pristine HCSs, it was observed that the thermal stability increased from 566 °C (see **section 3.3.1.5** for reference) to ~ 650 °C upon CNFs growth. The broad peak is suggestive of two types of carbon with the higher temperature carbon now dominating and that the presence of CNFs increases the thermal stability of the carbon.

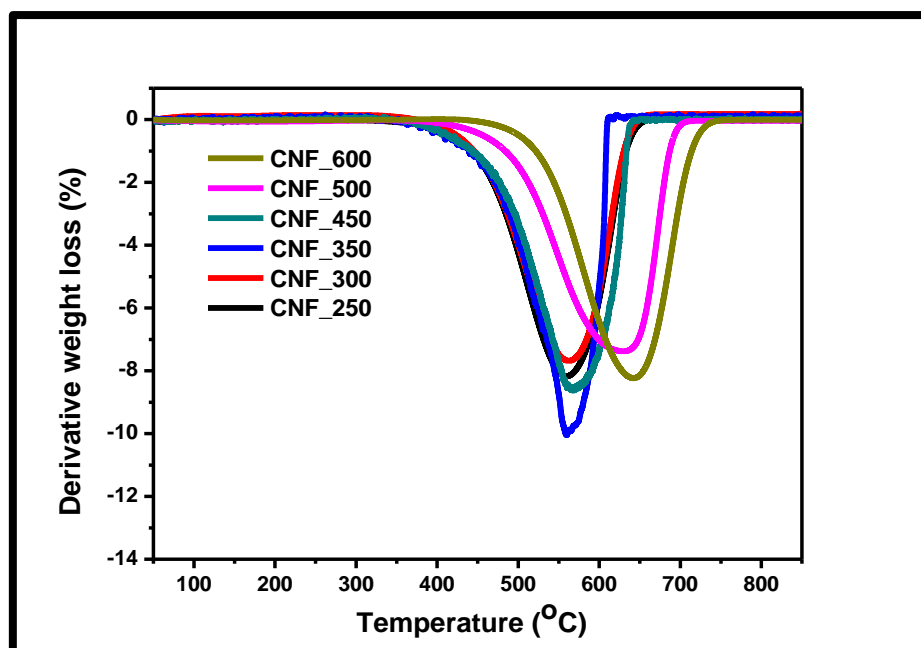


Figure 4. 12: DTG plots of CNFs synthesized at different temperatures ($H_2/C_2H_2 = 100$ mL/min, 5 min).

Table 4. 2: Summarizes decomposition temperature of CNFs at different temperatures

Sample	Decomposition Temperature (°C)
CNF_250	560
CNF_300	565
CNF_350	567
CNF_450	574
CNF_500	628
CNF_600	646

4.3.2.3. Synthesis of CNFs over NiO@HCSs catalyst: Effect of H₂ flow rate

The influence of H₂ on the growth of CNFs was assessed. The hydrogen flow rate was varied from 20 mL/min to 120 mL/min. To accurately assess the influence of the H₂ flow rate, the CNFs were synthesized by firstly passing N₂ (100 mL/min) over the Ni catalyst. Once the desired reaction temperature was reached, N₂ flow was stopped and hydrogen (at variable flow rates) was passed over the catalyst for 30 min. After catalyst activation, acetylene (100 mL/min) together with H₂ was passed over the Ni catalyst. All reactions were carried out for 5

min at 450 °C. The products collected were denoted as CNF_20, CNF_50, CNF_80, CNF_100, and CNF_120 (labelled according to H₂ flow rate used).

4.3.2.3.1. TEM analysis of CNFs grown at different H₂ flow rates

Figure 4.13 shows TEM micrographs of CNFs prepared at various H₂ flow rates. At 20 mL/min, the CNFs exhibited mostly bimodal growth with irregular morphology. In some instances, CNFs with very short lengths were observed. This indicates that at this flow rate, not all nickel particles are activated as the growth of CNFs is limited. When the flow rate was increased (50 mL/min), CNFs gave monomodal and bimodal fibers with a helical morphology (**figure 4.13b**; see inset). Upon a further increase to 80 and 100 mL/min, both straight and helical CNFs continued forming. However, the yield of CNFs with helical morphology decreased and more fibers were linear. At 120 mL/min, the TEM images revealed more fibers with a linear morphology and a monomodal growth mode (see inset, **figure 4.13e**). No bimodal growth mode was observed. The various morphologies observed indicate that there was a rapid reconstruction of the Ni particles as the H₂ flow rate was varied. The occurrence of metal catalyst reconstruction as reaction conditions are varied has been observed and discussed in the literature [6, 8, 13]. The CNFs are mostly seen growing at the node of a single Ni grain.

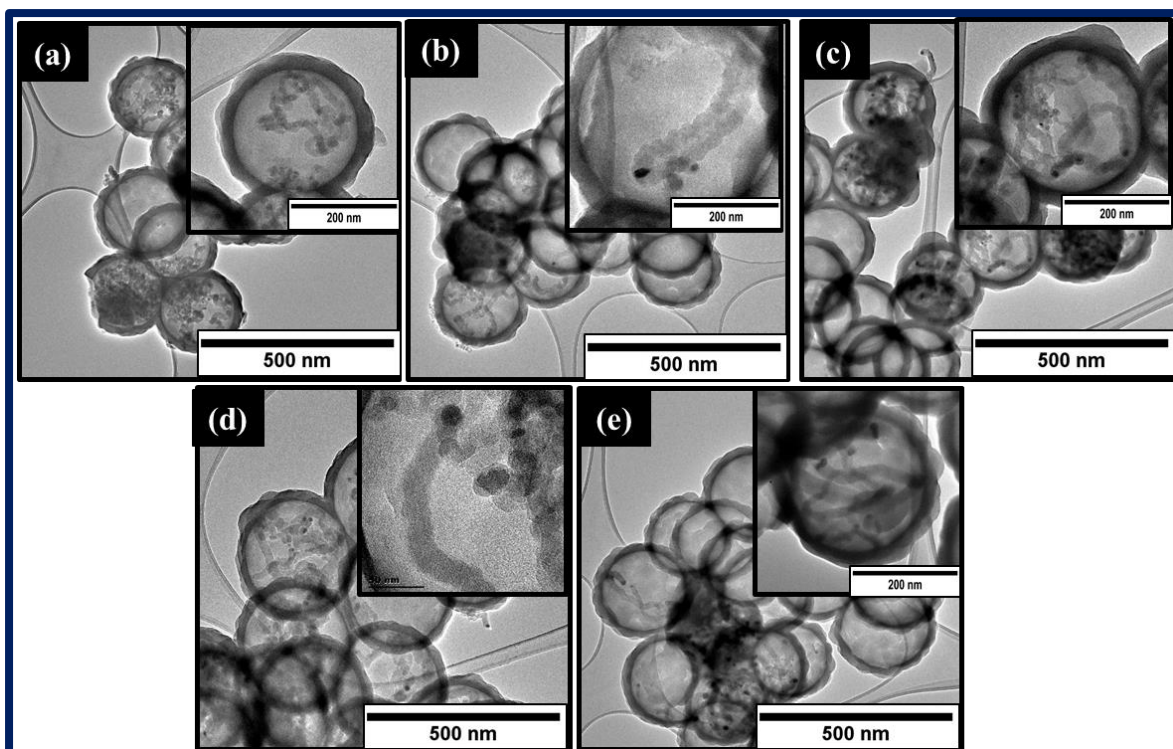


Figure 4. 13: TEM images of CNFs synthesized at different H₂ flow rate, (a) CNF_20, (b) CNF_50, (c) CNF_80, (d) CNF_100 (inset; HRTEM image showing clearly the mono-directional growth of CNF from a single nickel particle) and (e) CNF_120 mL/min.

The graph of % yield against the H₂ flow rate is shown in **figure 4.14**. The plot shows that as the flow rate was increased from 20 to 100 mL/min, the amount of carbon formed increased. Increasing the flow rate further to 120 mL/min resulted in a decrease in the carbon yield. The observed decrease in carbon yield is attributed to the formed carbon layer that covers the nickel particle at higher flow rates thereby deactivating the catalyst. Similar trends have been reported in other studies [13, 18, 19].

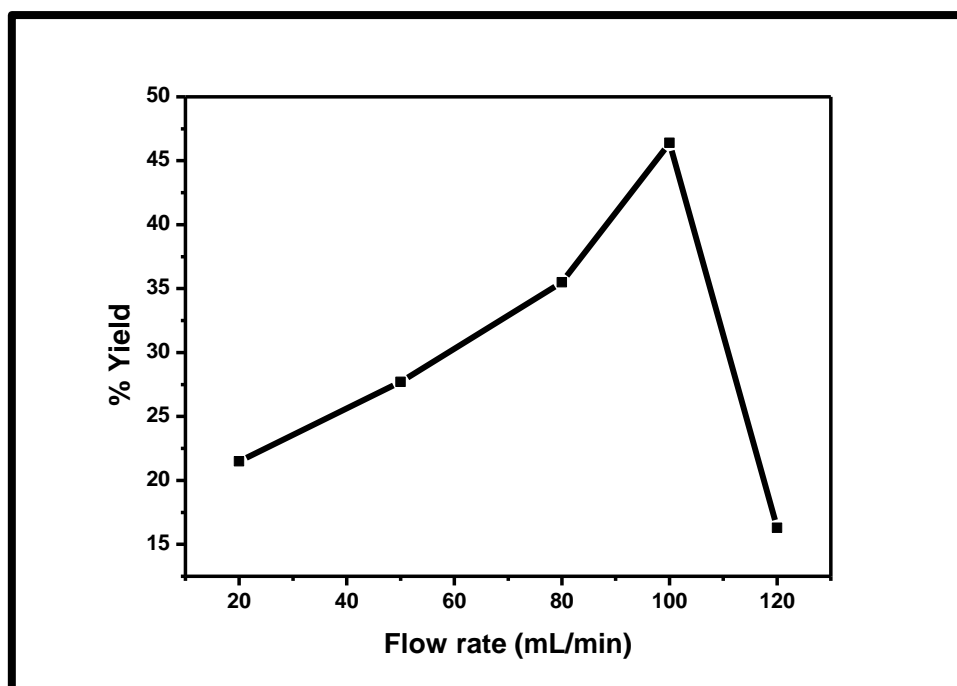


Figure 4. 14: Plot of carbon % yield obtained at different H₂ flow rates.

4.3.2.3.2. Raman analysis of CNFs synthesized at different H₂ flow rates

The structural properties of CNFs grown were studied using Raman spectroscopy to elucidate the effect of the H₂ flow rate on the CNFs. The Raman spectra obtained are shown in **figure 4.15** and the data acquired is summarized in **Table 4.3**. The Raman spectra revealed the presence of two well-defined peaks corresponding to the D (associated with the disorder and defects) and the G (associated with the ordered graphite) bands. The I_D/I_G values determined for TCE_20, TCE_50, TCE_80, TCE_100 and TCE_120, were found to be 0.82, 0.77, 0.81, 0.81 and 0.76, respectively. The results showed no direct trend in the I_D/I_G values. However, considering the extremes, the data suggests that the degree of graphitization increased from 20 mL/min to 120 mL/min.

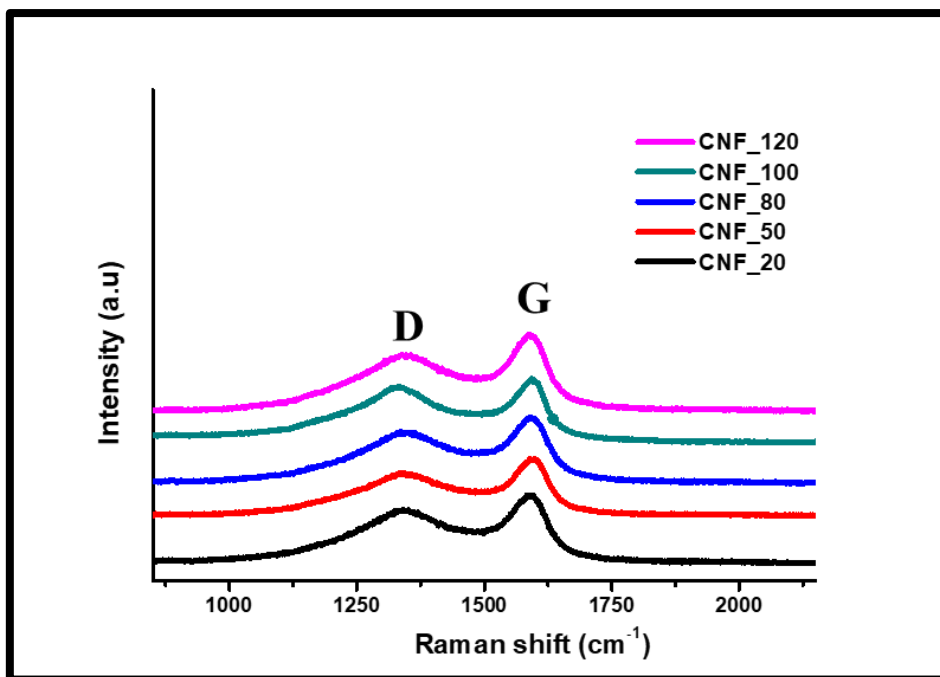


Figure 4. 15: Raman spectra of CNFs synthesized at different H₂ flow rates.

Table 4. 3: Summary of the Raman data of the obtained CNFs

Material	D band peak position (cm ⁻¹)	G band peak position (cm ⁻¹)	I _D / I _G ratio
CNF_20	1344	1585	0.82
CNF_50	1346	1590	0.77
CNF_100	1344	1585	0.81
CNF_80	1348	1587	0.81
CNF_120	1346	1586	0.76

4.3.2.3.3. TGA analysis of CNFs synthesized at different H₂ flow rates

To further ascertain the effect of the H₂ flow rate on the thermal stability of the CNFs, TGA analysis was conducted. The TGA and DTG profiles of CNFs synthesized at different H₂ flow rates are shown in **figure 4.16** and **figure 4.17**, respectively. The onset decomposition temperature of the CNFs synthesized was observed in the temperature range ~400–530 °C. All samples showed a 0 wt% residual as shown in **figure 4.17**.

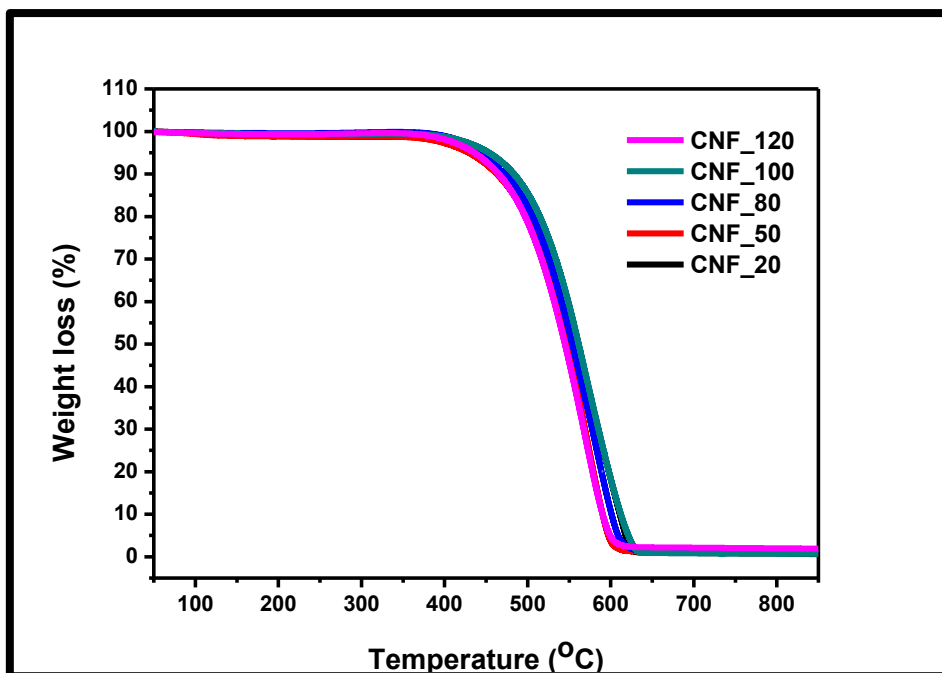


Figure 4. 16: TGA plots of CNFs synthesized at different H₂ flow rates.

DTG profiles show the maximum decomposition temperature of the as-prepared CNFs. The DTG data show no direct trend in the thermal stabilities. However, overall, a decrease in the thermal stability was observed from 574 to 560 °C (**Table 4.4**), which indicates that the thermal stability showed a small decrease with an increase in H₂ flow rate.

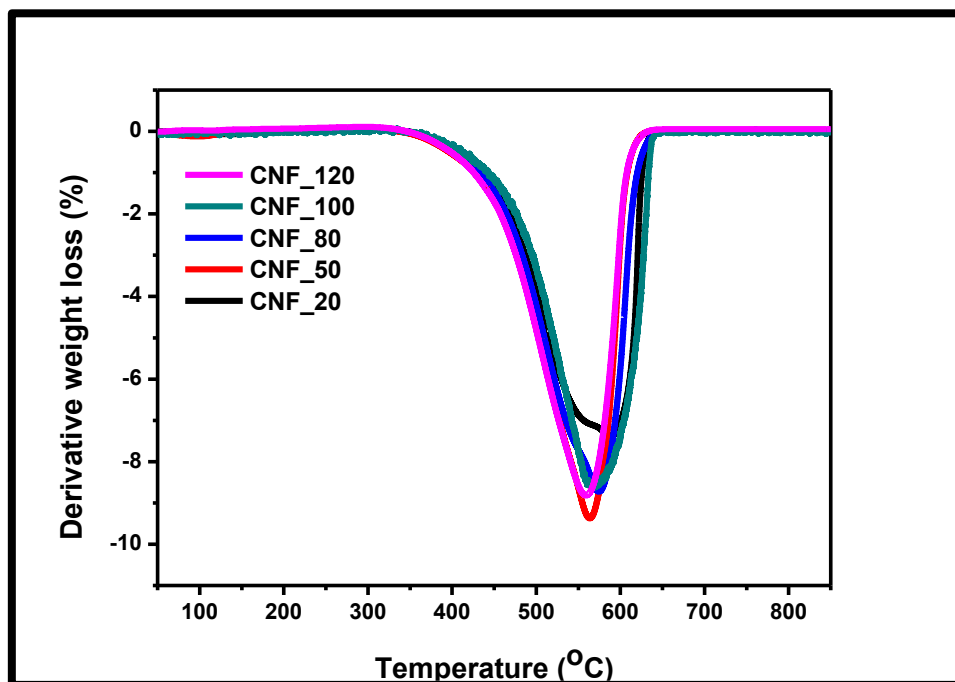


Figure 4. 17: CNFs synthesized at different H₂ flow rates.

Table 4. 4: Summarizes maximum decomposition temperatures of CNFs at different H₂ flow rates

Sample	Decomposition Temperature (°C)
CNF_20	574
CNF_50	563
CNF_80	577
CNF_100	570
CNF_120	560

4.3.2.4. Synthesis of CNFs over NiO@HCSs catalyst: Effect of reaction time

In this study, acetylene was passed over Ni catalyst at different times (5-90 min). Standard reaction conditions were used i.e. hydrogen, nitrogen and acetylene flow rates were all 100 mL/min. The reactions were carried out at 450 °C. The products collected were denoted as CNF_5, CNF_15, CNF_30, CNF_60 and CNF_90 min (labelled according to their reaction time).

4.3.2.4.1. TEM analysis of CNFs synthesized at different reaction times

TEM images of the CNFs synthesized at different reaction times are shown in **figure 4.18**. After passing acetylene over Ni catalyst, a mono-directional growth was mostly observed and few nickel nanoparticles broke into smaller particles to form thinner CNFs. Both mono- and bi-directional growth of straight fibers continued forming after 15 min. When the reaction was increased to 30 min, two types of morphologies were then observed; those with a straight and a helical morphology (**figure 4.18c; indicated by an arrow**). This implies that during the initial stage of CNF growth, a linear CNF grew and as the reaction time increased, the catalyst particle restructured, which later resulted in a helix. Similar results were reported by Shaikjee *et al.* [4]. However, these were formed in a low quantity (*ca.* < 5%). After 60 and 90 min, straight and helical fibers continued growing. In general, the length and diameter of CNFs grown varied depending on the nickel grain size. Also, it was observed that reaction time had a significant impact on the yield of CNFs, fiber length but not on the CNFs morphology. This

indicates that, for as long as there are active sites available on the Ni grains, the CNFs will continue growing in length. It was noted that the CNFs were contained within the HCSs even at longer reaction time (**figure 4.18e**). However, the observed CNFs outside the HCSs after 60 min may be due to broken HCS which exposes the catalyst and promote growth outside.

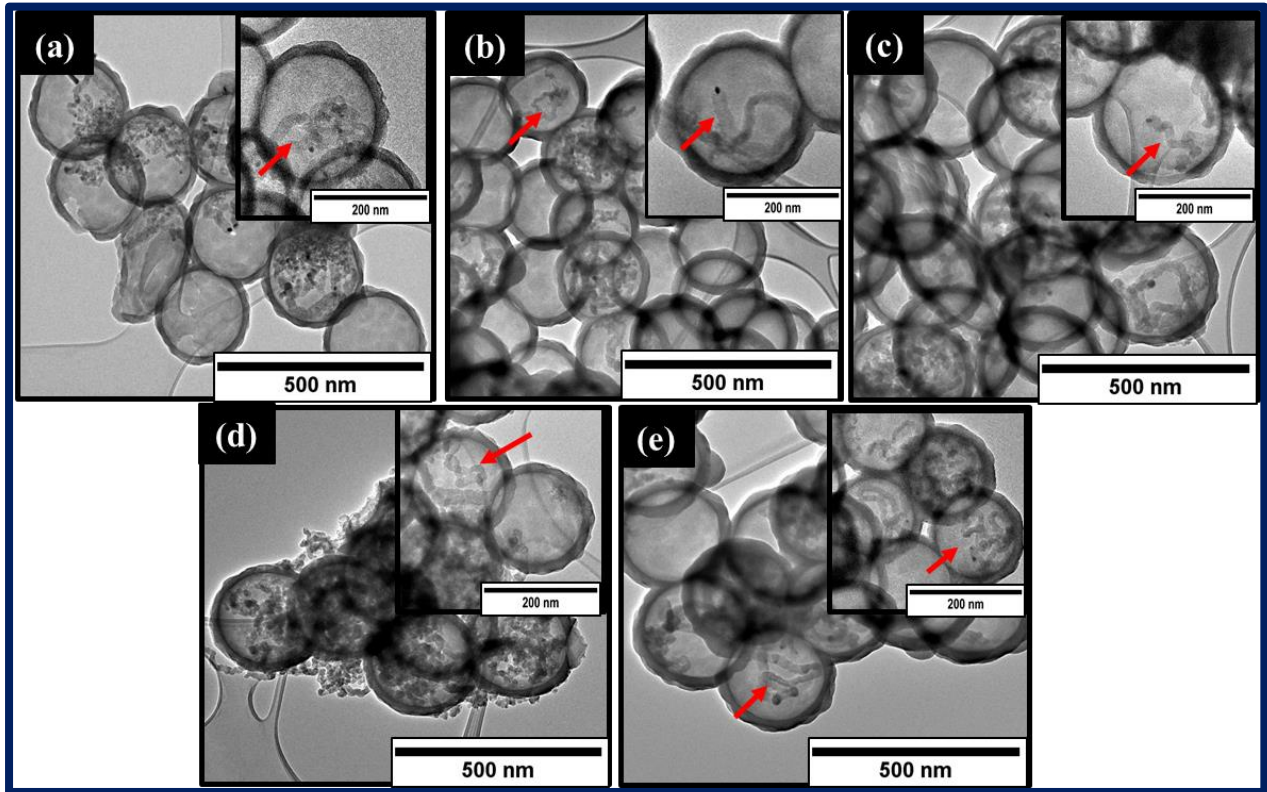


Figure 4. 18: TEM images of CNFs synthesized at reaction time, (a) CNF_5, (b) CNF_15, (c) CNF_30, (d) CNF_60 and (e) CNF_90 min.

Figure 4.19 shows a relationship between the CNFs and reaction time (yield determined using equation 1). It is observed that as reaction time increases, the CNFs yield increased as a result of available active sites on a nickel grain.

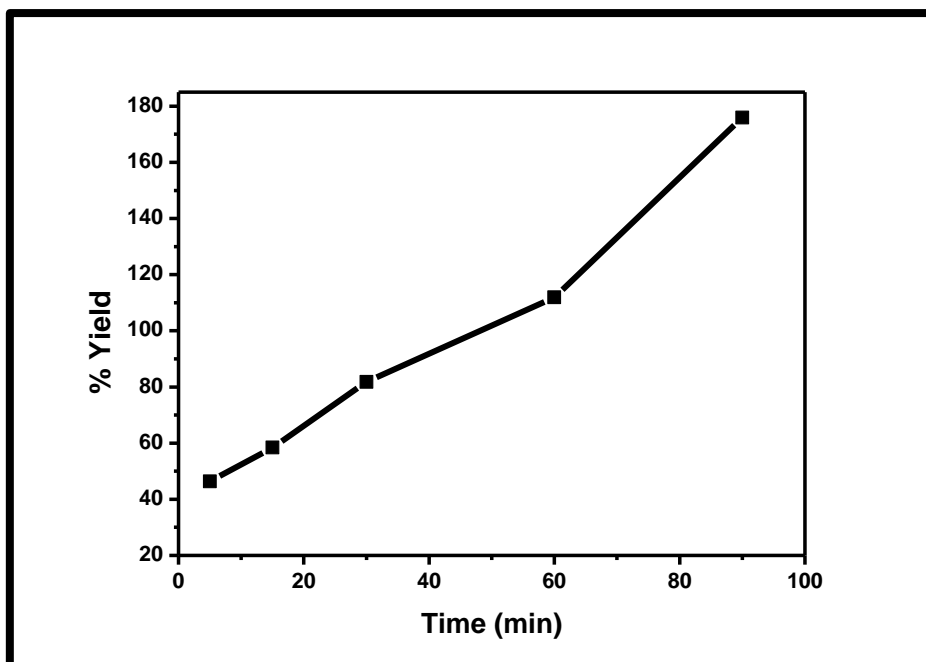


Figure 4. 19: Statistical plot of CNFs synthesized at different reaction times. A direct relationship between the % yield and reaction time was observed.

4.3.2.4.2. Raman analysis of CNFs synthesized at different reaction times

Raman plots of the synthesized CNFs at different reaction times are displayed in **figure 4.20**. The Raman data showed a decrease in the I_D/I_G ratio (**Table 4.5**) as reaction time increased. This indicates that as the reaction time increases the carbon material becomes more ordered.

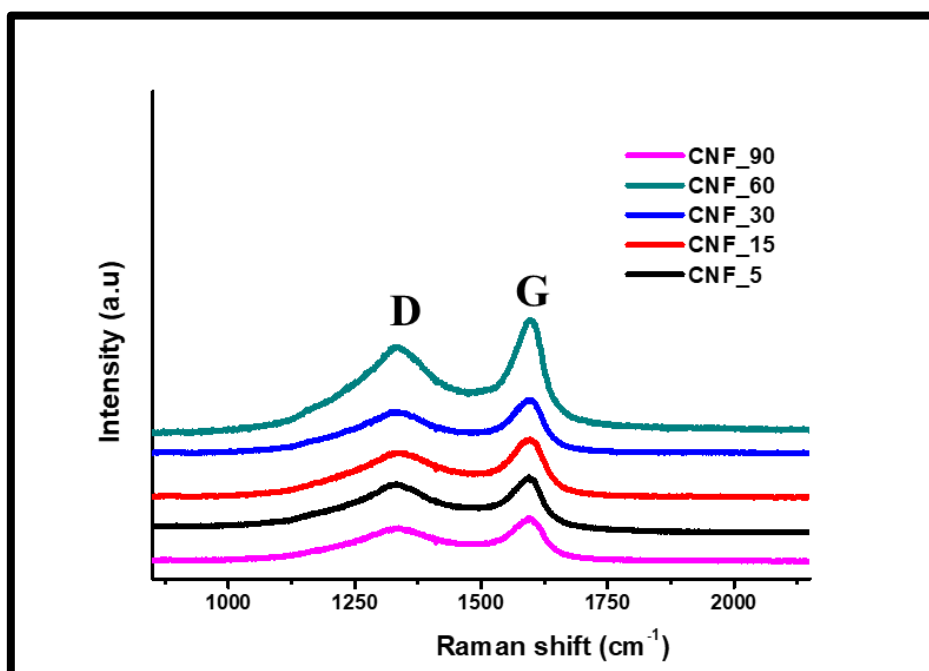


Figure 4. 20: Raman spectra of CNFs synthesized at different reaction times.

Table 4. 5: Summary of the Raman data of the obtained CNFs

Material	D band peak position (cm ⁻¹)	G band peak position (cm ⁻¹)	I _D /I _G ratio
CNF_5	1344	1585	0.81
CNF_15	1340	1589	0.80
CNF_30	1335	1589	0.79
CNF_60	1337	1592	0.76
CNF_90	1336	1589	0.76

4.3.2.4.3. TGA analysis of CNFs synthesized at different reaction times

TGA profiles of CNFs grown at different reaction times are shown in **figure 4.21**. TGA profiles revealed that CNFs synthesized for 60 min were thermally stable compared to CNFs synthesized at lower reaction times. In general, it is observed that the thermal stability increased as the reaction time increased. However, beyond 60 min the thermal stability decreased (at 90 minutes). This observation was not expected and thus could not be explained.

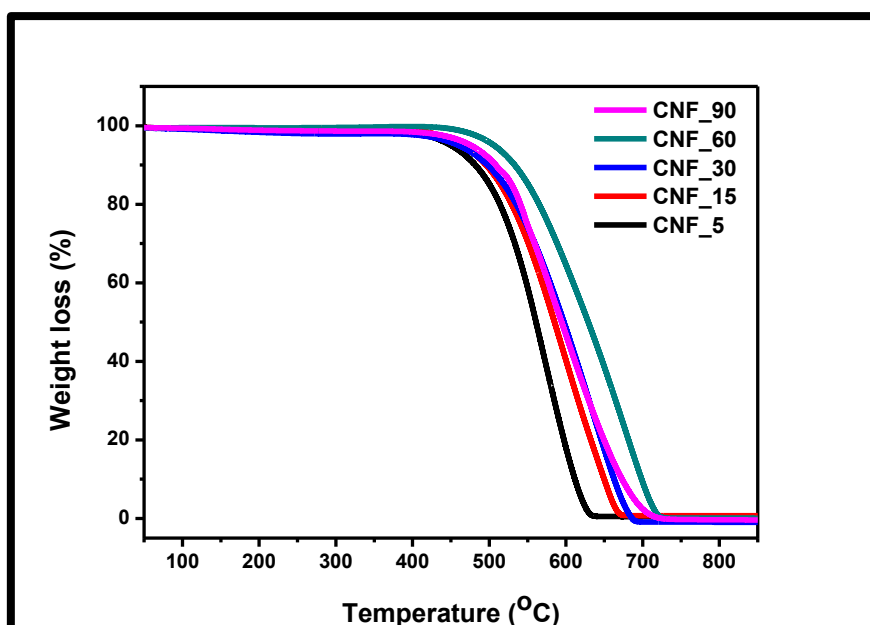


Figure 4. 21: TGA plots of CNFs synthesized at different reaction times.

DTG plots of CNFs synthesized at different reaction times are shown in **figure 4.22**. The obtained maximum decomposition temperatures of CNFs are summarised in **Table 4.6**. At 15 min, the DTG plot showed a broad shoulder peak at 592 °C on a major peak at 642 °C. CNFs synthesized at 30 and 60 min decomposed at a higher temperature. The shift in the peaks might be due to defects present in the material. At 90 min, CNFs decomposed at a lower temperature compared to the others. This observed data cannot be accurately be explained. However, the observed data showed that the inferred reaction time modified the thermal stability of CNFs. The observed increase in the thermal stability (5 min to 60 min) is in agreement with the Raman data which revealed that as reaction time increases the material becomes more ordered.

It was noted that from all the samples, the HCSs are less stable than the CNFs. As more CNFs form, the peak shifts to higher temperature. The FWHM of the HCSs + CNFs composite is larger (increased from 103-158) than the pure HCSs (119), which indicates that both HCSs and CNFs are present.

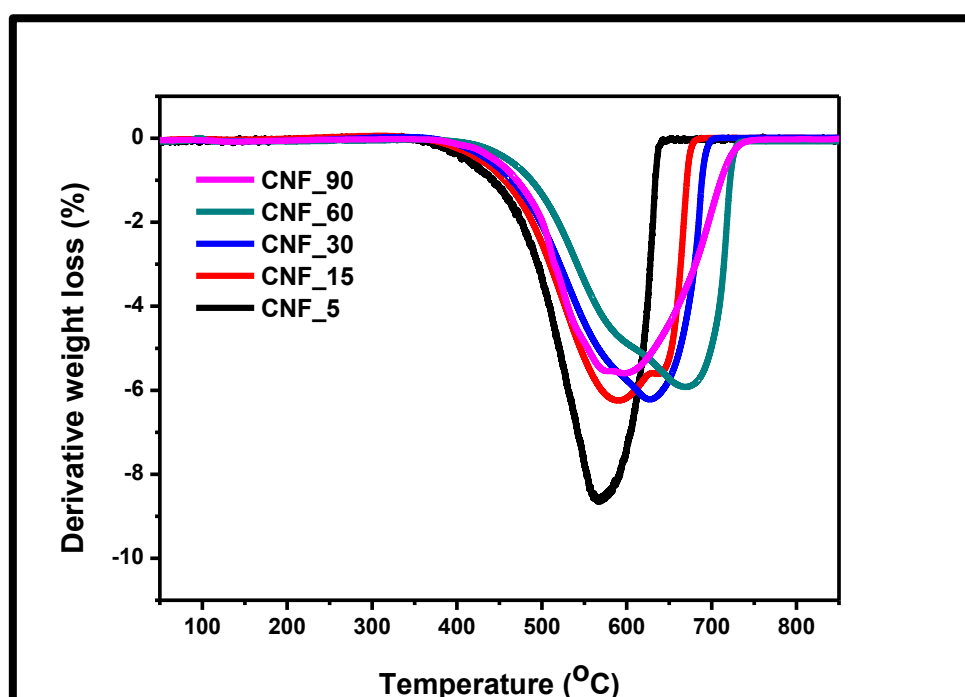


Figure 4. 22: TGA plots of CNFs synthesized at different reaction times.

Table 4. 6: Summarizes maximum decomposition temperatures of CNFs at different time intervals

Sample	Decomposition Temperature (°C)	
CNF_5	-	569
CNF_15	592	642
CNF_30	-	631
CNF_60	-	672
CNF_90	-	594

Conclusions

The synthesis of CNFs outside and inside the HCSs with straight and helical morphology was successful. The CNFs grown outside the HCSs revealed an enormous growth of the CNFs whilst a more controlled growth was observed for CNFs grown inside the HCSs. Ni agglomeration was observed for the NiO/HCSs catalyst upon CNF growth which resulted in CNFs with variable morphology and size. The CNFs grown from 5 wt% NiO@HCSs and NiO@HCSs showed a variation in their morphology, size, diameter and length. This was dominantly affected by the size, shape, and the number of Ni nanoparticles available outside/inside the HCSs. The CNFs grown at low Ni loading (0.5 wt%) formed CNFs with a more controllable growth.

The TEM tilting experiments confirmed the synthesis of CNFs inside the HCSs. The morphology of the CNF was affected by the temperature. Both mono and bi-directional growth of CNFs with straight and helical morphology were observed. The temperature study suggested that 450 °C was the ideal growth temperature for the CNFs. Also, it was noted that at high temperature (600 °C), Ni fragmentation prevailed, and this resulted in the formation of thin CNFs. The time study showed no significant impact on the morphology of the CNFs, and the hydrogen flow rate showed that higher H₂ flow rates results in CNFs with defined morphology. The TGA, XRD, and Raman studies confirmed the presence of CNFs in/on the HCSs network.

References

1. D. Chen, K.O Christensen, E. Ochoa-Fernández, Z. Yu, B. Tøtdal, N. Latorre, A. Monzón, A. Holmen, *Journal of Catalysis*, 229 (2005) 82-96.
2. L. Feng, N. Xie, J. Zhong, *Materials*, 7 (2014) 3919-3945.
3. Y. Li, Z. Liu, Y. Jiang, B. deGlee, D. Li, J. Zeng, *Journal of Mater Science*, 53 (2018), 479-491.
4. A. Shaikjee A, P.J. Franklyn P.J, N.J. Coville N.J, *Carbon*, 49 (2011) 2950-2959.
5. Y. Qin, Z. Zhang, Z. Cui, *Carbon*, 42 (2004) 1917-1922.
6. M.S. Maubane, S.S. Bhoware, A. Shaikjee, N.J. Coville, *Diamond & Related Materials*, 72 (2017) 53-60.
7. P.E. Anderson, N.M. Rodri'guez, *Chemistry of Matererials*, 12 (2000) 823-830.
8. S. Bhoware, M.S. Maubane, T. Phaahlamohlaka, A. Shaikjee, N.J. Coville, *Chemical Physics Letters*, 577 (2013) 71-75.
9. X. Ren, H. Zhang, Z. Cui, *Materials Research Bulletin*, 42 (2007) 2202-2210.
10. . J.-H. Zhou, Z.-J. Sui, P. Li, D. Chen, Y.-C. Dai, W.-K. Yuan, *Carbon*, 44 (2006) 3255-3262.
11. H. Raghubanshi, M.S. Hudson, O.N. Srivastava, *International Journal of Hydrogen Energy*, 36 (2011) 4482-4490.
12. P.M. Gangatharan, M.S. Maubane, N.J. Coville, *Scientific Reports*, 9 (1) (2019) 1-7.
13. M.S. Maubane, *Nickel and copper catalysed synthesis of carbon fibers*, Ph.D. Thesis, University of the Witwatersrand, Johannesburg, (2013).
14. Y. Wang, S. Serrano, J.J. Santiago-Avilès, *Synthetic Metals*, 138 (2003) 423-427.
15. M.S. Maubane, M.A. Mamo, E.N. Nxumalo, W.A.L. van Otterlo, N.J. Coville, *Synthetic Metals*, 162 (2012) 2307-2315.
16. J.H. Kaufman, S. Metin, D.D. Saperstein, *American Physical Society*, 39 (18) (1989) 13053-13060.
17. F. Li, J. Liu, Z. Guo, *Materials Research Bulletin*, 44 (1) (2009) 25-29.
18. Z. Yu, D. Chen, B. Tøtdal, A. Holmen, *Materials Chemistry and Physics*, 92 (2005) 71-81.
19. C. Pham-Huu, N. Keller, V.V. Roddatis, G. Mestl, R. Schlögl, M.J. Ledoux, *Physical Chemistry Chemical Physics*, 4 (2002) 514-521.

CHAPTER 5

Synthesis of carbon nanofibers over NiO@HCSs catalyst using trichloroethylene as a carbon precursor.

5.1. Introduction

The fabrication of structured carbon nanomaterials by decomposition of various hydrocarbons is now being widely studied [1-3, 9-12]. Previous studies have shown that both the choice of catalyst and carbon precursor influence the morphology of the carbon nanomaterial formed [3-5]. Carbon nanomaterials with a wide range of morphologies have been produced from a variety of hydrocarbons. Shaikjee *et al.* [6] illustrated the effect of substituted alkynes on the morphology of Ni catalysts and the subsequent carbon nanofiber morphology produced. From the study, they observed the formation of a wide range of morphologies from the substituted alkynes including Y-shaped, helical, linear, co-block and straight fibers. Although many chlorinated organic compounds are known for their high toxicity, these compounds have also been employed to produce structured carbon nanomaterials with unique and fascinating morphologies [14, 18]. Also, it has been reported that chlorine-containing compounds produce better yields of materials when compared to their equivalent non-chlorinated compounds [1-5]. Nieto-Marquez *et al.* [5] reported on the catalytic growth of structured carbon from various chlorinated hydrocarbon over a Ni/SiO₂ catalyst in the temperature regime 637-1073 K. Brichka *et al.* [3] and Lv *et al.* [8] reported on the synthesized carbon nanotubes (CNTs) from chlorine-containing hydrocarbons and observed the formation of closed packed CNTs, twisted CNTs, CNTs consisting of branches, parallel CNTs having a spiral form and multi-walled CNTs (MWCNTs), respectively. A study conducted by Mishakov *et al.* [1] revealed the formation of bidirectional and tetra-directional (four-sided) CNFs growth with disordered and inhomogeneous graphite layers from the decomposition of 1, 2-dichloroethane over Ni/Al₂O₃ and Co/Al₂O₃ catalysts. It was noted that the formation of these interesting morphologies is due to the presence of Cl in the reaction system, which exerts a significant influence on the morphology of the produced carbon material. It is also worth flagging the work from our research group on the synthesis of the tripod and multipod CNFs by decomposition of trichloroethylene (TCE) over Ni catalysts as reported in [3] and [14]. These studies triggered an interest in the use of TCE as a carbon source for the current study. To the best of the author's

knowledge, there are no documented reports on the synthesis of carbon nanofibers (CNFs) from encapsulated Ni catalyst using TCE as a carbon source.

As such, the present chapter is aimed at studying the effect of trichloroethylene on the peculiarities of the morphology and structure of CNFs resulting from the decomposition of trichloroethylene (TCE) over NiO@HCSs. We have also examined the effect of reaction parameters (temperature, time and flow rate) on the CNF growth. Lastly, a study on the effect of using different nickel compounds on the growth of CNFs was demonstrated.

5.2. Experimental Procedure

5.2.1. Synthesis NiO@HCSs catalyst

The NiO@HCSs catalysts using different nickel compounds (nickel acetate hexahydrate, nickel chloride hexahydrate, and nickel nitrate) were prepared as discussed in **Chapter 3** (Experimental section).

5.2.2. Synthesis of CNFs using 0.5 wt% NiO@HCSs catalyst

CNFs were synthesized using a horizontal single-stage CVD technique as illustrated in **Figure 5.1** [3, 14-15]. Typically, the as-synthesized 0.5 wt% NiO@HCSs catalyst (50 mg) was uniformly spread over a quartz boat and the boat was placed at the center of a quartz tube reactor placed at the center of a furnace to ensure controlled heating. The furnace was then heated at 10 °C/min under hydrogen flow at a flow rate of 100 mL/min. Once the desired growth temperature was reached, an inert gas (N₂) was introduced into the system and bubbled through TCE together with hydrogen also at a flow rate of 100 mL/min. The reaction was carried out for different time intervals (5-90 min). After the reaction, the TCE flow was stopped and the reaction was cooled down to room temperature under hydrogen flow.

In addition, other reactions were carried out using different nickel precursors (nickel acetate hexahydrate, nickel chloride hexahydrate, and nickel nitrate) to study the effect of using different nickel precursors on the growth of the CNFs. Similar reaction conditions as described above were used.

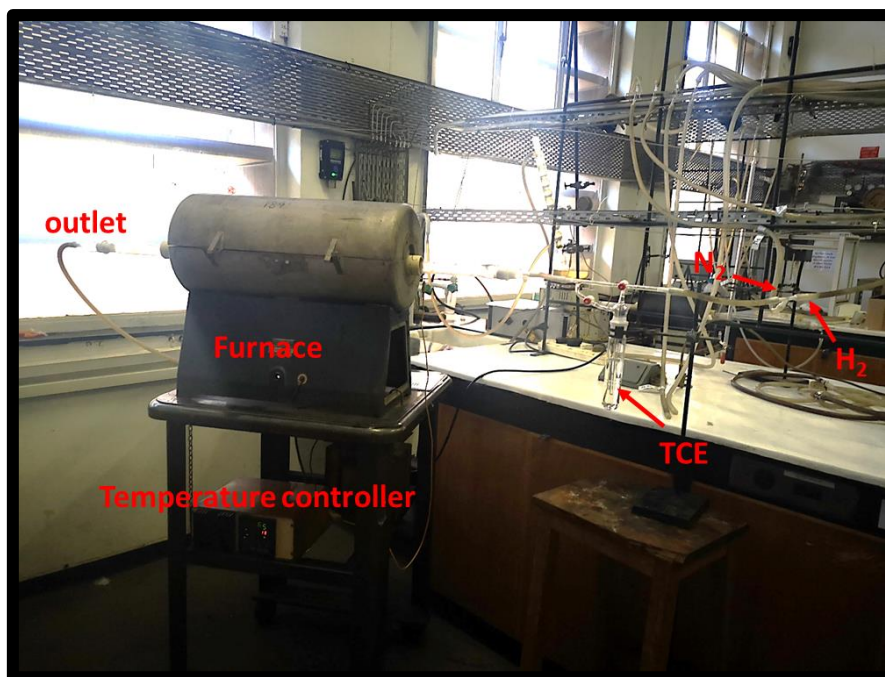


Figure 5. 1: CVD set-up for the synthesis of CNFs using TCE as a carbon source.

5.2.3. Determination of the carbon yield

The carbon percentage yield reported in this study was determined using equation 1 [13].

$$\text{Carbon yield \%} = \frac{(m_{\text{tot}} - m_{\text{cat}})}{m_{\text{cat}}} \times 100 \dots \dots \dots \text{equation 1}$$

where; m_{cat} – the mass of the catalyst, and m_{tot} - total weight of the sample after reaction

5.2.4. Characterization techniques

The morphology features of the synthesized CNFs were ascertained by transmission electron microscopy (TEM), using an FEI Tecnai G2 Spirit electron microscope at 120 kV. The energy dispersive X-ray spectroscopy (EDS) was used to determine the distribution of elements on the surface of the samples. The structural features were assessed by Raman spectroscopy using a Jobin-Yvon T6400 micro-Raman spectrometer and X-ray diffraction (XRD) on a Bruker D2 phaser equipped with Cu-K α radiation. The thermal stabilities of the carbon materials were carried out in air using thermo-gravimetric analysis (TGA) technique on a Perkin-Elmer STA6000 analyzer.

5.3. Results and discussion

5.3.1. Synthesis of CNFs using 0.5 wt% NiO@HCSs catalysts (nickel acetate hexahydrate precursor).

5.3.1.1. The influence of reaction temperature on CNFs growth.

The synthesis of CNFs was achieved by pyrolysis of trichloroethylene (TCE) over 0.5 wt% NiO@HCSs catalyst. To investigate the optimum temperature at which the CNFs grew, a temperature study was conducted. The influence of the temperature on the growth of CNFs has been reviewed [3-4, 11, 14]. In this study, the CNFs were grown using standard conditions but at different temperatures (350, 450, 500 and 600 °C) using TCE as a carbon source. The flow rate of hydrogen and nitrogen was kept constant (100 mL/min) and all reactions were carried out for 5 min. The retrieved products were denoted as TCE_350, TCE_450, TCE_500, and TCE_600 (labelled according to their reaction temperatures).

5.3.1.1.1. Morphology analysis: TEM analysis

Figure 5.2 presents the TEM micrographs of CNFs synthesized at different temperature regimes. The TEM micrographs show that temperature affects the morphology of the CNFs. At 350 °C, carbon growth was observed that appeared to be covering the Ni particle (**see arrow in figure 5.2a**). CNFs were also observed and the fiber length was estimated to be 30 nm. This infers the slow decomposition of TCE over the surface of Ni particles. When the temperature was increased to 450 °C and 500 °C, irregular shaped Ni crystallites with a diameter of *ca.* 19 nm and 22 nm, respectively were observed (**see EDS spectra in Appendix C, figure S5.1 for confirmation of Ni**). The CNFs formed from these particles showed monomodal fiber growth from a single Ni grain (**see arrows in figure 5.2b, c**). The CNFs exhibited an irregular morphology with a narrow diameter distribution of 27 ± 5 nm and 29 ± 4 nm at 450°C and 500 °C, respectively. At 600 °C, the CNFs revealed a flower-like morphology (this was in low yield *ca.* < 2%) and an abundance of a linear morphology that appeared to have a hollow channel ($d = 31 \pm 11$ nm) (**figure 5.2d, see the arrows**). This indicates that as the temperature increased, the Ni catalyst underwent reconstruction to yield the observed morphologies. In contrast to the current findings, previous studies revealed the formation of CNFs with a bamboo-like and tripod-like morphology from the decomposition of trichloroethylene over Ni/SiO₂ and unsupported Ni catalyst at 400-750 °C [3-5, 14]. However, the CNFs with a hollow central core using chlorinated hydrocarbon have been reported under different conditions [5, 18].

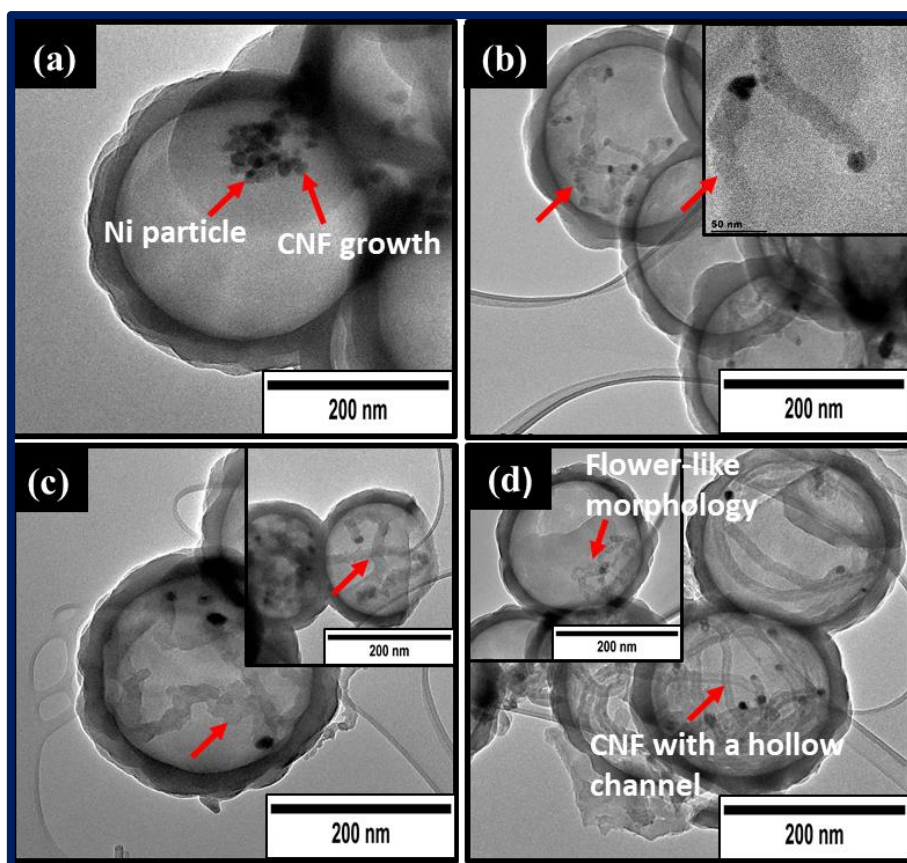


Figure 5. 2: TEM images of CNFs using TCE over 0.5 wt% NiO@HCSs catalyst at (a) TCE _350, (b) TCE _450 (inset, HRTEM showing monomodal growth of CNFs with irregular morphology), (c) TCE _500 and (d) TCE_600.

The statistical plot showing the relationship between carbon yield and the growth temperature (determined by equation 1) is shown in **figure 5.3**. It is observed that as the temperature was increased the yield of CNFs increased. Nieto *et al.* [5] suggested that the increase of carbon yield from CNFs grown from the chlorinated compound is due to the presence of Cl which serves to enhance carbon deposition. Based on the TEM study, the optimum temperature for the CNFs growth with monomodal growth mode was found to be at 450 °C. Thus, this was chosen as an ideal temperature to study CNFs growth in further experiments to assess the influence of other reaction parameters on fiber growth.

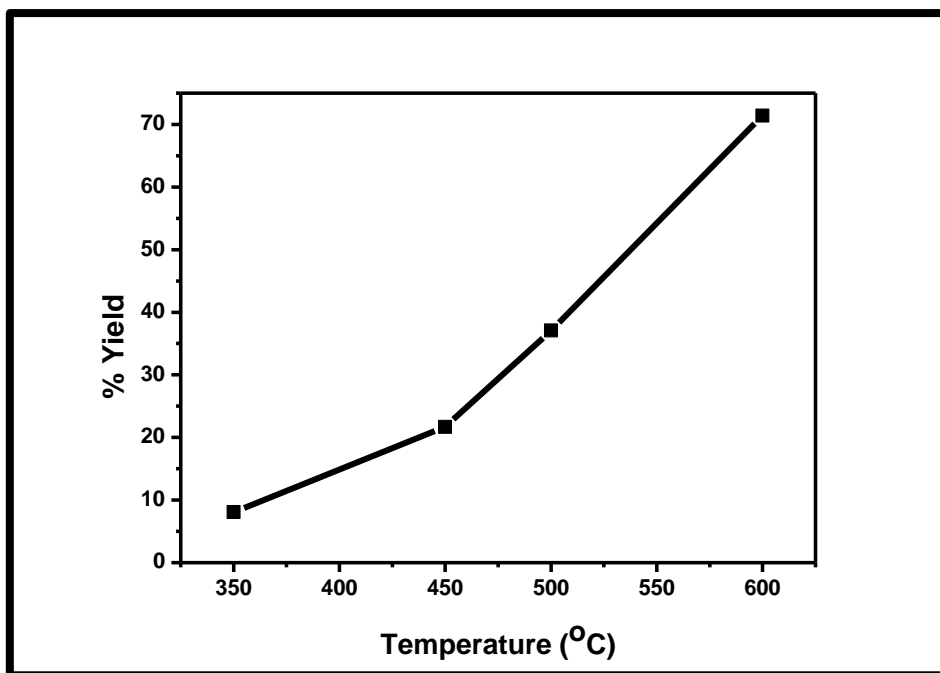


Figure 5. 3: Graph showing % yield of CNFs as the reaction temperature increases.

5.3.1.1.2. Raman analysis of CNFs synthesized at different growth temperatures.

Raman spectroscopy was used to provide information on the degree of graphitization of the as-prepared carbon nanofibers in response to the change in the reaction temperature. The Raman spectra show two main peaks; the D and G bands which are characteristic of carbon materials [15, 16,]. The observed D band is known as the disorder-induced phonon mode and the G band is associated with a high degree of symmetry and order of carbon materials [17]. The relative intensity value (I_D/I_G) parameter provides information on the amount of order and disorder of the carbon material. A small I_D/I_G value corresponds to a highly ordered material. **Figure 5.4** illustrates the Raman spectra of the CNFs synthesized at different temperatures and **Table 5.1** summarizes the differences in the parameters. It is noted from **Table 5.1** that as the temperature increased (450-600 °C), the I_D/I_G ratio decreased which is related to the formation of more CNFs. This suggests that as the temperature increases, the carbon crystal structure becomes more ordered.

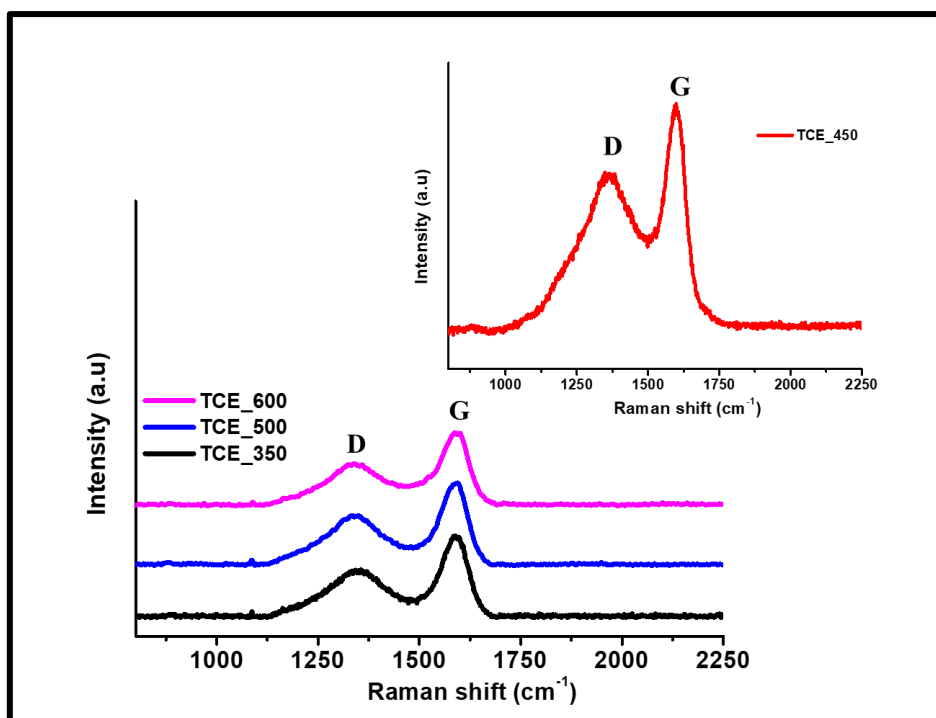


Figure 5. 4: Raman plots of CNFs synthesized at different temperatures.

Table 5. 1: The I_D/I_G ratios of D and G peaks of the obtained CNFs

Material	D band peak position (cm^{-1})	G band peak position (cm^{-1})	I_D / I_G ratio
TCE_350	1345	1587	0.57
TCE_450	1362	1595	0.72
TCE_500	1339	1585	0.59
TCE_600	1339	1584	0.55

5.3.1.1.3. Thermal gravimetric analysis (TGA) analysis of CNFs grown at different reaction temperatures

TGA analysis is a common tool used to evaluate the thermal properties of materials. In this study, TGA studies were conducted to assess the thermal stabilities of the CNFs prepared at different temperatures. The TGA and DTG measurements were done under a continuous flow of air (20 mL/min) at a heating rate of 10 °C/min. **Figure 5.5** and **Figure 5.6** show TGA and DTG profiles of the CNFs synthesized at 350-600 °C. TGA profiles (**figure 5.5**) showed that the oxidation of CNFs synthesized at 350-500 °C starts at $T < 200$ °C, which is attributed to the presence of amorphous carbon. The complete oxidation is observed above 450 °C. The CNFs synthesized at 600 °C are stable in this temperature range and only start decomposing at $T > 500$ °C. The residual weight loss of CNFs after combustion was found to be 0.3 wt% for TCE_350 and 0 wt% for TCE_450, TCE_500, and TCE_600 samples. The small amounts of Ni residue detected was due to the large amount of carbon that formed.

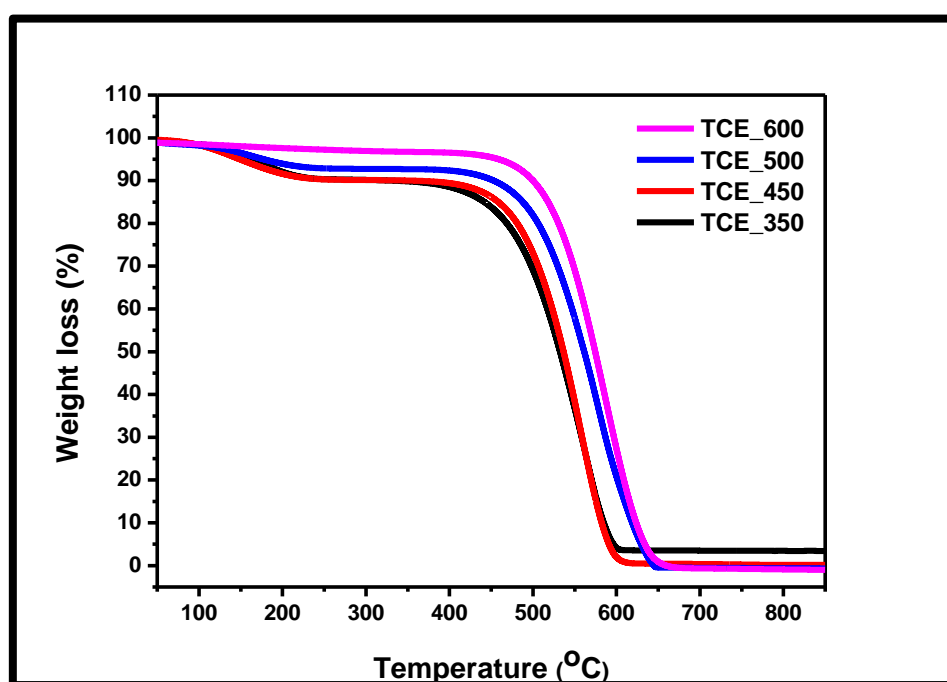


Figure 5. 5: TGA plots of CNFs synthesized at different temperatures.

The DTG plots help to identify the maximum decomposition temperature of the CNFs in air. The DTG profiles are shown in **figure 5.6** and the decomposition temperatures are summarized in **Table 5.2** The maximum decomposition temperatures of the CNFs synthesized at 350, 450, 500 and 600 °C were observed at 537, 544, 565, and 579 °C, respectively. The DTG plot shows a broad peak at *ca.* 200 °C (presumably due to Cl containing material) and as the temperature increased, the peaks became sharper. The narrow decomposition peak observed at high

temperature (450-600 °C) is attributed to the presence of large amounts of CNFs with almost similar dimensions (as can be seen from TEM data). In general, the thermal stability increased as the growth temperature increased. This suggests that as the growth temperature increased, the carbon material became more ordered as suggested by the Raman data.

In comparison with the decomposition temperatures of the pristine HCSs (566 °C, see **chapter 3**), it is noted that the HCS + CNFs composite decomposed at a higher temperature. This indicates that the presence of CNFs grown using TCE increased the thermal stability of the carbon.

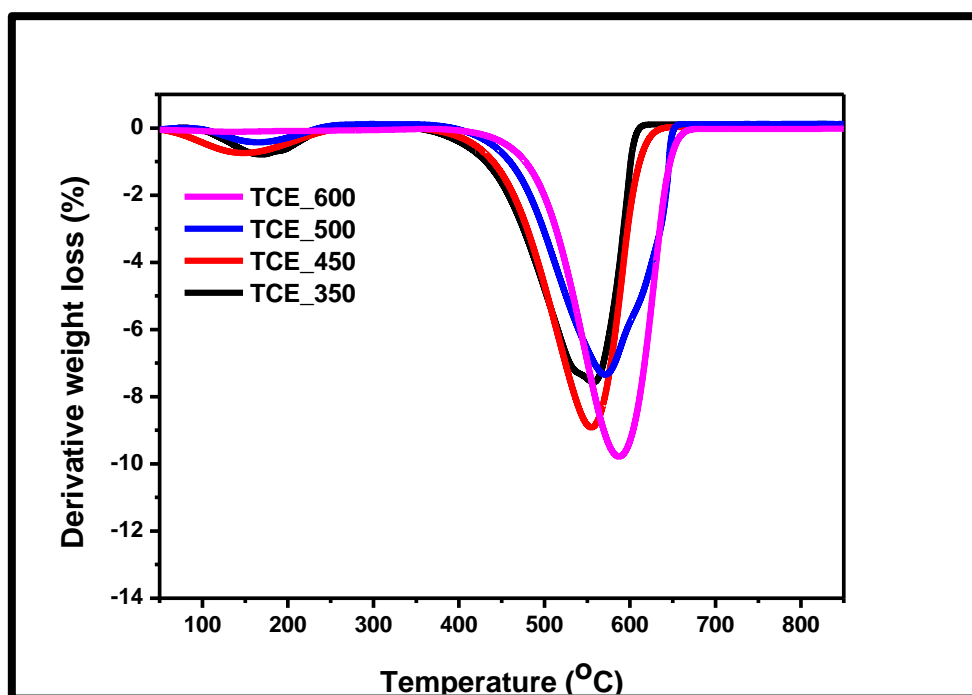


Figure 5. 6: DTG plots of CNFs synthesized at different temperatures.

Table 5. 2: Summarizes the decomposition temperature of CNFs synthesized at different temperatures

Sample	Decomposition Temperature (°C)	
TCE_350	170	537
TCE_450	151	544
TCE_500	164	565
TCE_600	-	579

5.3.1.2. The influence of H₂ flow rate on the synthesis of CNFs using TCE.

Different experiments were carried out to study the influence of the H₂ flow rate (20-120 mL/min) on the formation of CNFs using TCE. The flow rate of H₂ was varied from 20 to 120 mL/min during the CNFs synthesis over the 0.5 wt% NiO@HCSs catalyst and keeping the N₂ flow rate constant (100 mL/min). The reactions were carried out for 5 min at 450 °C. The resulting products were labelled as TCE_20, TCE_50, TCE_80, TCE_100 and TCE_120 (named after the H₂ flow rate used).

5.3.1.2.1. TEM analysis of CNFs grown at different H₂ flow rates

The influence of having both H₂ and N₂ (as carrier gas) in the reaction chamber for the synthesis of CNFs was investigated. In the first experiment, the CNFs were synthesized by bubbling N₂ through TCE in the absence of H₂. TEM images obtained (**figure 5.7a, b**) shows the formation of a flat irregular shaped sheet structure with the HCSs morphology completely diminished. In the second experiment, CNFs were synthesized by bubbling H₂ through TCE in the absence of N₂. This resulted in the formation of spherical shaped carbon (**figure 5.7c, d**) that appeared as solid clusters, as well as chain-like structures with an average diameter of *ca.* 35 ± 6 nm. The hollow structure of the HCSs could not be detected. From both experiments, no fiber growth was observed. Thus, this indicated that the presence of both H₂ and N₂ gases is crucial for the synthesis of CNFs.

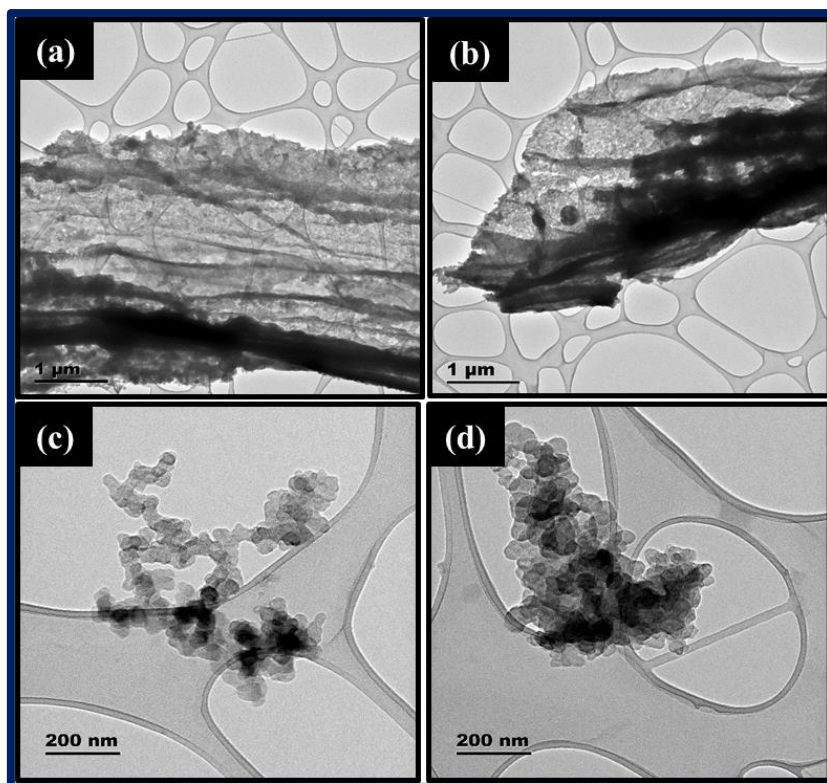


Figure 5. 7: TEM images of Ni catalysts; (a), (b) TCE deposited in the absence of H₂ and (c), (d) TCE deposited in the absence of N₂ (synthesized at 450 °C for 5 min).

To evaluate the influence of H₂ flow rate on the CNFs synthesis, the flow rate of N₂ (100mL/min) was maintained constant in all experiments. **Figure 5.8** shows TEM micrographs of CNFs as H₂ flow rate was varied. CNFs with different morphologies were observed as the flow rate was varied. At 20 mL/min, the CNFs formed a tripod-like morphology (**figure 5.8a**, indicated by an arrow) and few monomodal fibers were also observed (*ca.* < 2% yield). The formation of CNFs with a tripod morphology has been reported elsewhere in literature but this was observed at higher flow rates [3, 14]. As the flow rate increased to 50, 80 and 100 mL/min, the morphology of the fibers formed changed dramatically due to the restructuring of the Ni nanoparticles to give dominantly monomodal straight CNFs. The tripod structure was not observed at these flow rates. After 120 mL/min on-stream, a decrease in the CNFs growth (*ca.* 17% yield) was noted and CNFs showed a mono-directional growth (**figure5.8e**, see arrow).

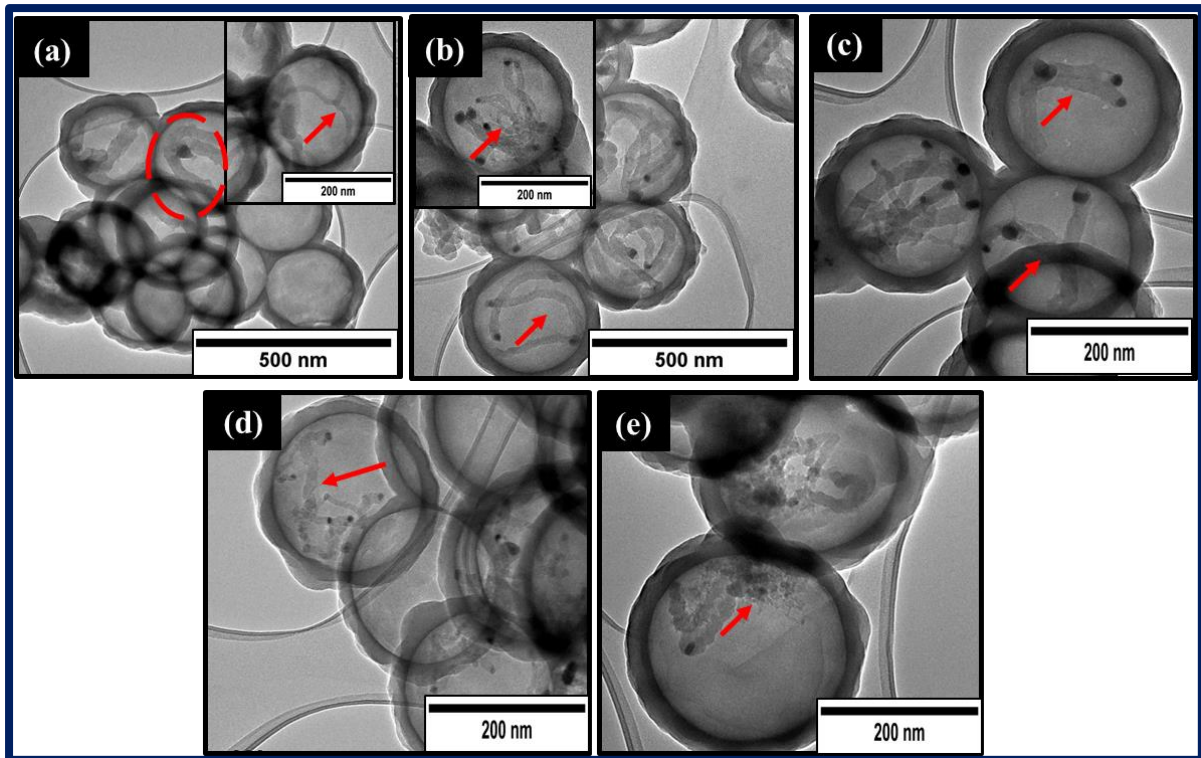


Figure 5. 8: TEM images of CNFs synthesized at different H₂ flow rate, (a) TCE _20, (b) TCE _50, (c) TCE _80, (d) TCE _100 and (e) TCE _120 mL/min.

Figure 5.9 shows the relationship between H₂ flow rate and % yield. The data reveal that at lower flow rates, the reaction is under diffusion control and at higher flow rate, the carbon yield decreased. Hydrogen is known to either accelerate or suppress the formation of carbon material. Pham-Huu *et al.* [21] showed that a too large increase in the H₂ content led to a slight decrease in carbon yield. Ci *et al.* [22] suggested that the presence of hydrogen in the feed drives the reverse reaction for decomposition due to the gasification of the deposited carbon.

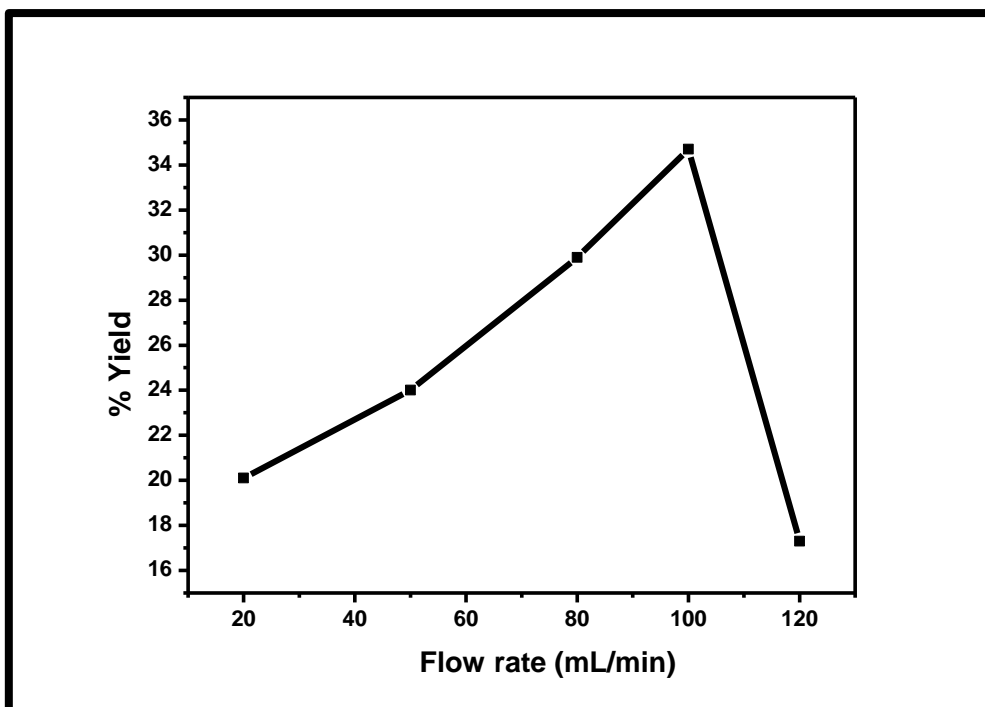


Figure 5. 9: Statistical plot of CNFs synthesized at different H₂ flow rates.

5.3.1.2.2. Raman analysis of CNFs grown at different H₂ flow rates.

Raman spectroscopy was used to probe the effect of flow rate on the synthesized CNFs. The Raman spectra are shown in **figure 5.10** and the data acquired is summarised in **Table 5.3**. The Raman spectra revealed the presence of the D and G bands featured around 1360 cm⁻¹ and 1590 cm⁻¹, respectively. It was observed that the H₂ flow rate had an insignificant effect on the D and the G band positions. The I_D/I_G intensity ratios were used to measure the structural quality of the carbon. It was observed that increasing the H₂ flow rate, the I_D/I_G ratio increased from 0.48 to 0.72 (**Table 5.3**). This means that varying the flow rate introduces structural defects. However, above 100 mL/min the I_D/I_G decreased which indicated that as the flow rate increased further, the carbon framework becomes more ordered.

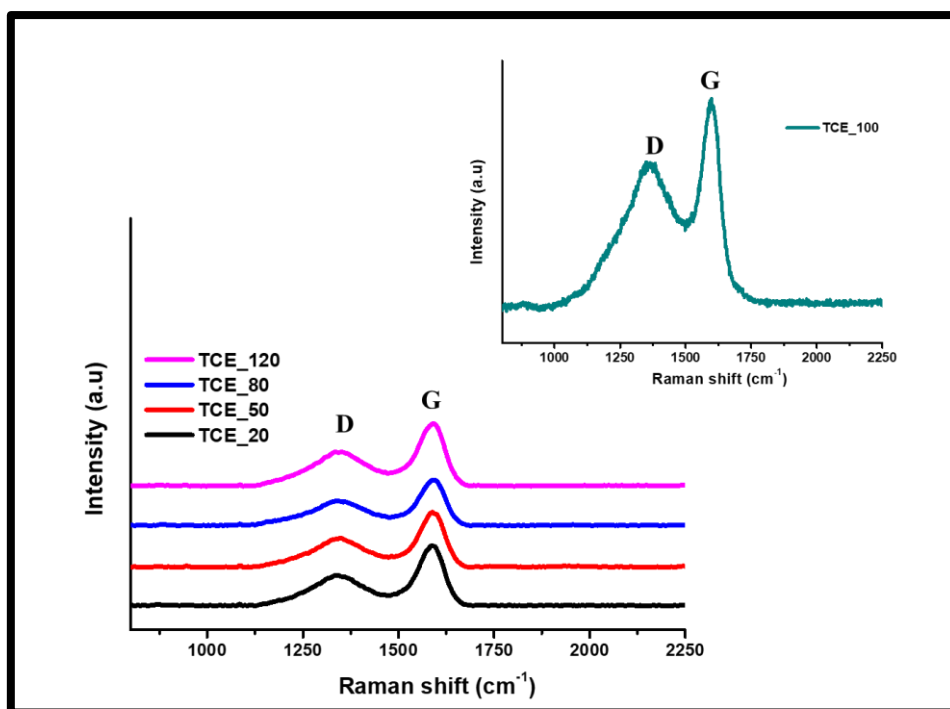


Figure 5. 10: Raman spectra of CNFs synthesized at different H₂ flow rate, TCE_20, TCE_50, TCE_ 80, TCE_100 and TCE_120 mL/min (synthesized at T= 450 °C, for 5 min).

Table 5. 3: The I_D/I_G ratios of D and G peaks of the obtained CNFs

Material	D band peak position (cm ⁻¹)	G band peak position (cm ⁻¹)	I_D / I_G ratio
TCE_20	1341	1585	0.48
TCE_50	1343	1587	0.50
TCE_80	1343	1588	0.52
TCE_100	1362	1595	0.72
TCE_120	1345	1587	0.54

5.3.1.2.3. TGA analysis of CNFs grown at different H₂ flow rates.

The thermal stability of the CNFs was studied to evaluate the effect of the H₂ flow rate on the synthesis of the CNFs. The TGA plots (**figure 5.11**) and DTG plots (**figure 5.12**) showed similar results to those obtained in the previous study. However, in this study, two decomposition peaks were observed in all experiments. The onset decomposition temperature for the first and second peaks was observed at $T < 200$ °C and $T > 400$ °C, respectively as shown in **figure 5.11**. As in the previous study, this was ascribed to the presence of additional amorphous and graphitic carbon in the material. The residual weight loss was found to be 0 wt% in all samples which showed that the samples contained little to no Ni residue.

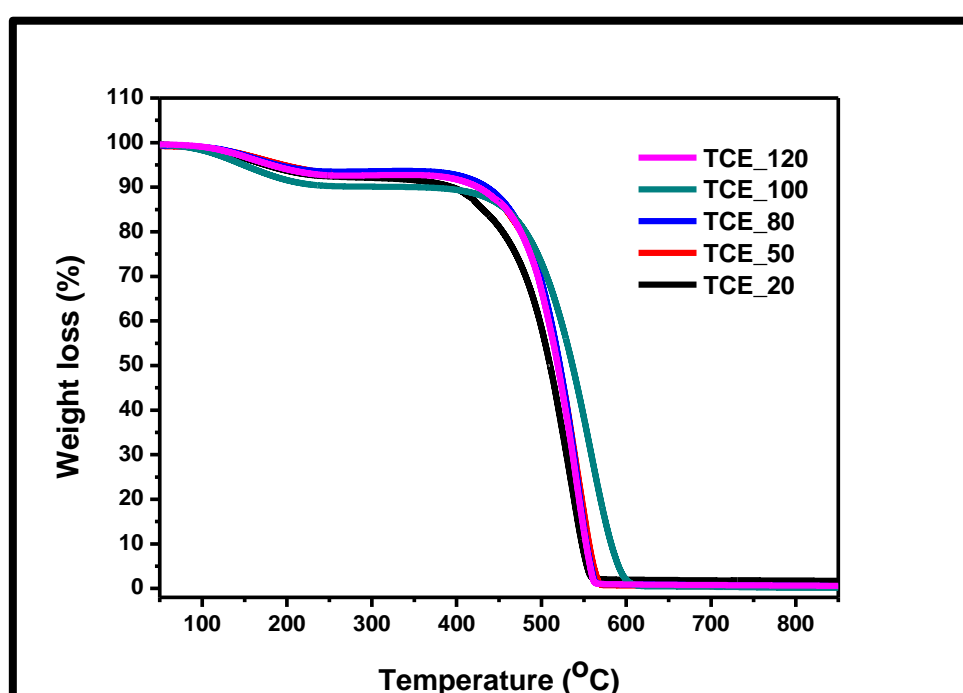


Figure 5. 11: TGA plots of CNFs synthesized at the different H₂ flow rate (T= 450 °C, growth time 5 min).

The DTG plots (**figure 5.12**) revealed that the maximum decomposition of TCE_20, TCE_50, TCE_80, and TCE_100 occur at 522, 532, 533 and 557 °C, respectively (**Table 5.4**). This suggested that as the H₂ flow rate increased the thermal stability of the CNFs formed increased. Also, it was observed that at 20 mL/min there is a presence of a shoulder peak at ~ 417 °C (indicated by an arrow), suggesting the presence of another form of carbon. This could tentatively be assigned to the decomposition of the tripod carbon morphology (as seen from TEM data) since this morphology was only observed at this flow rate. Moreover, it was noted that at 120 mL/min the thermal stability decreased. As such, the 100 mL/min flow rate was

chosen as the optimum H₂ flow rate for the synthesis of CNFs. Similar results were reported by Maubane *et al.* [15] for a flow rate study over unsupported Ni particles.

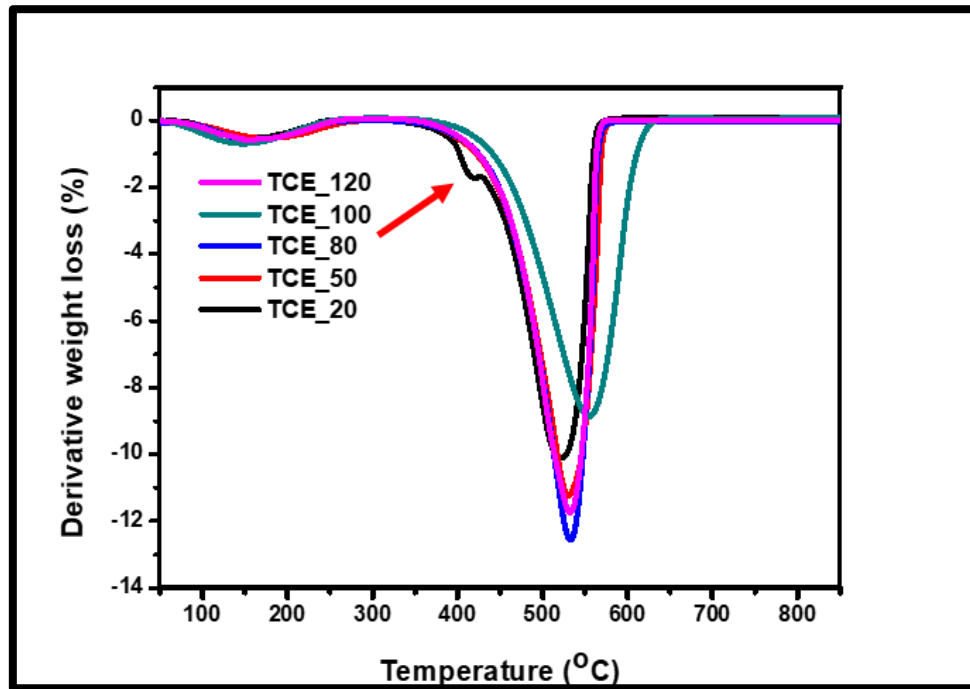


Figure 5. 12: TGA plots of CNFs synthesized at different H₂ flow rates (T= 450 °C, growth time 5 min).

Table 5. 4: Summarizes maximum decomposition temperatures of CNFs at different H₂ flow rates

Sample	Decomposition Temperature (°C)	
TCE_20	162	522
TCE_50	175	532
TCE_80	166	533
TCE_100	155	557
TCE_120	166	533

5.3.1.3. The influence of reaction time on the synthesis of CNFs.

Studies have shown that the duration of the reaction has an impact on the length and carbon yield of carbon nanomaterials [3, 5]. As such, the effect of reaction time on the synthesis of CNFs (length and morphology) was evaluated. Trichloroethylene was passed over the Ni catalyst for different time intervals (5-90 min). Standard reaction conditions were used i.e. hydrogen and nitrogen flow rate were both 100 mL/min. The N₂ was used as a carrier gas to bubble through the TCE. The reactions were carried out at 450 °C. The products collected were denoted as TCE_5, TCE_15, TCE_30, TCE_60 and TCE_90 min (labelled according to their reaction time).

5.3.1.3.1. TEM analysis of CNFs synthesized at different reaction times.

The interaction between TCE and Ni nanoparticles was studied at different time intervals 0 - 90 min. Prior to the introduction of TCE into the reaction chamber, TEM images revealed that the catalyst consisted of small irregular shaped Ni crystallites with an average diameter of 12 ± 8 nm (**figure 5.13a**). After 5 min on-stream, the Ni grains were irregular in shape and the carbon showed a monomodal fiber growth. When the on-stream time was increased to 15 and 30 min, Ni with variable shapes (disk-like, quasi-spherical, rhombohedra, **figure 5.13c**) were observed and the carbon showed a monomodal fiber growth with rough edges. At 60 min on-stream, a multiple CNF growth from a single nickel crystallite (see the circle, **figure 5.13e**) was observed. After 90 min of growth, the CNFs monomodal fiber growth was observed and fracturing of Ni crystallites to form thin and thick fibers was also observed. It was also noted the CNFs grown were of variable lengths as the reaction time increased.

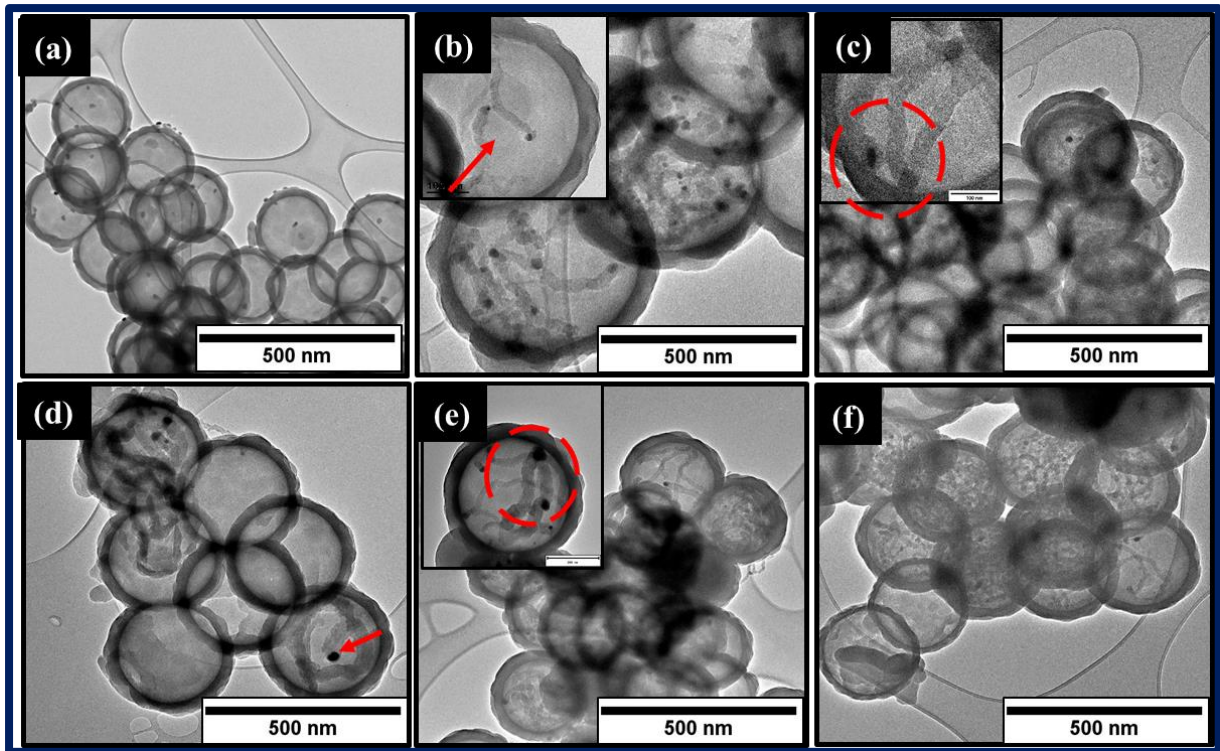


Figure 5.13: TEM images of CNFs synthesized at reaction time, (a) TCE_5, (b) TCE_15, (c) TCE_30, (d) TCE_60 and (e) TCE_90 min.

Figure 5.14 represents the carbon yield as a function of reaction time. The plot shows that as the reaction time increased, the carbon yield of CNFs increased. This suggests that, for as long as there are active sites on the nickel grain, the CNFs will continue growing.

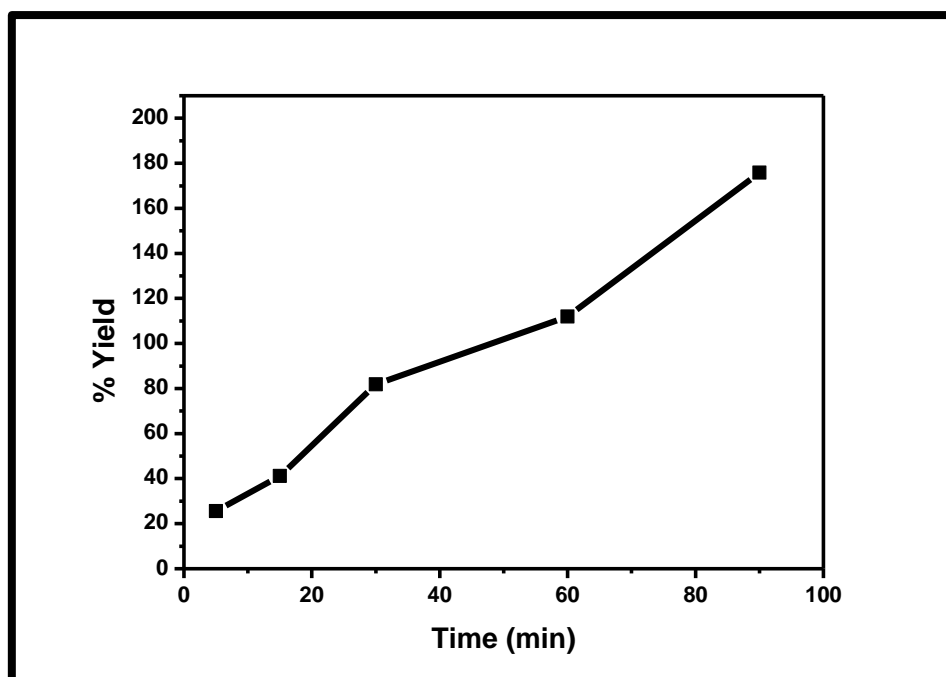


Figure 5. 14: Statistical plot of CNFs synthesized at different reaction times. A direct relationship between the % carbon yield and CNFs growth time was observed.

5.3.1.3.2. Raman analysis of CNFs synthesized at different reaction times.

Raman analysis was used to assess the degree of crystallization and defects present in the carbon materials as the reaction time was varied. The Raman spectra in **figure 5.15** showed the presence of the D and G bands. It was observed that as the reaction time increases, there was a decrease in the I_D/I_G ratio from 0.72 to 0.55 for TCE_5 and TCE_90, respectively (see **Table 5.5**). This indicates that as the reaction time increased, the degree of graphitization increased.

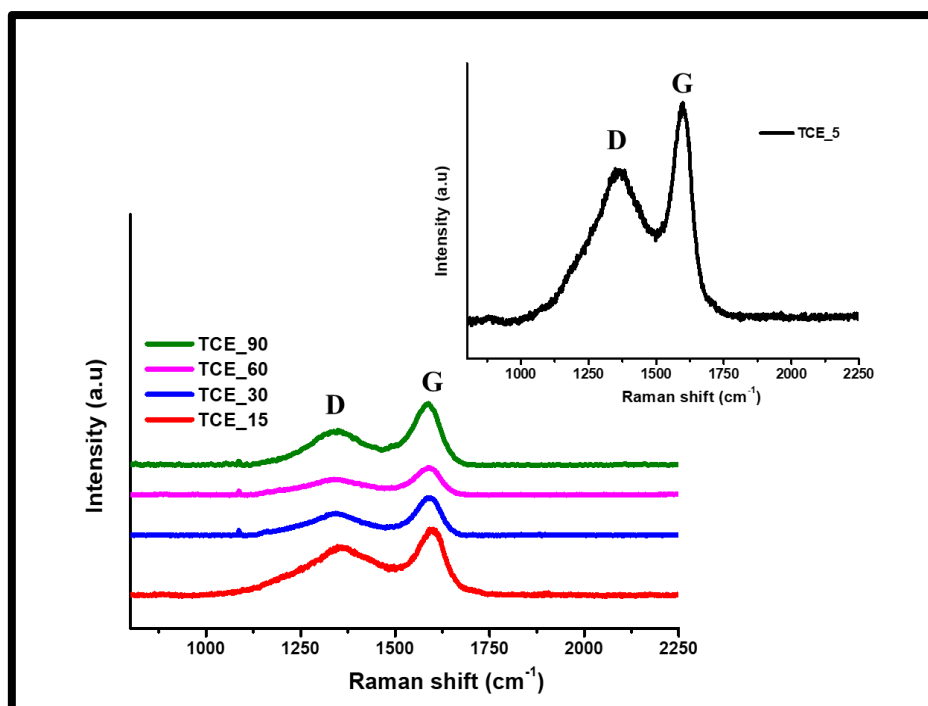


Figure 5. 15: Raman spectra of CNFs synthesized at different reaction times (synthesized at $T= 450\text{ }^{\circ}\text{C}$, H_2/N_2 flow rate =100 mL/min).

Table 5. 5: The I_D/I_G ratios of D and G peaks of the obtained CNFs

Material	D band peak position (cm^{-1})	G band peak position (cm^{-1})	I_D / I_G ratio
TCE_5	1362	1595	0.72
TCE_15	1360	1594	0.75
TCE_30	1342	1587	0.58
TCE_60	1342	1585	0.56
TCE_90	1345	1582	0.55

5.3.1.3.3. TGA analysis of CNFs synthesized at different reaction times using TCE.

The effect of reaction time on the growth of CNFs was further assessed using TGA analysis. **Figure 5.16** (TGA) and **figure 5.17** (DTG) shows plots of the as-synthesized CNFs as the reaction time is varied, when the measurements were conducted under an oxidizing

environment. DTG profiles revealed two prominent decomposition peaks at temperature < 200 °C and temperature < 570 °C at 5, 10 and 15 min. This is attributed to the presence of both amorphous carbon and graphitic carbon. At 30 and 60 min, the presence of the first decomposition peak was not observed, which suggests that as the reaction time increased, the carbon matrix became more ordered. Overall, it was also noted that increasing the duration of the reaction improved the thermal stability of the material significantly (see **Table 5.6**). These results are in good agreement with the Raman results, which indicated that the degree of graphitization increased as the reaction time increased. Notably, the residual weight after oxidation at 900 °C was found to be *ca.* 0 wt% in all samples (**figure 5.16**), which indicated that the amount of Ni present in the material was negligible.

Additionally, the dispersion of the FWHM of the decomposition peaks at high temperatures was found to be larger (94-133) compared to the FWHM of the HCSs (119) as the growth time increased. This indicates presence of two forms of carbons i.e. CNFs and HCSs as expected. Also, the thermal stability of the HCS + CNFs composite was found to increase as the reaction time increased compared to the pure HCSs (566 °C).

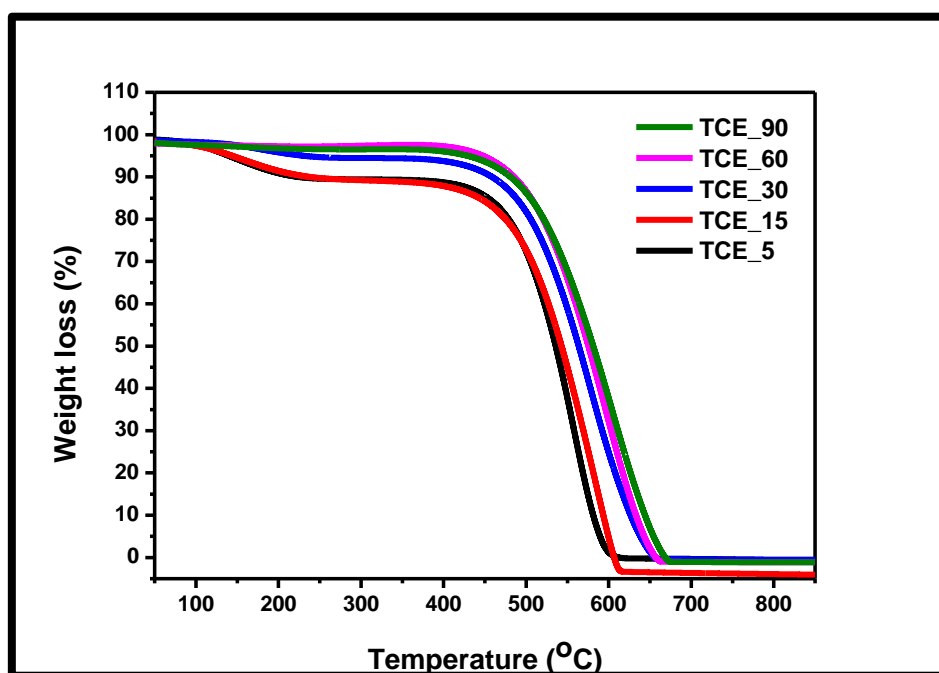


Figure 5. 16: TGA plots of CNFs synthesized at different reaction times ($T= 450^{\circ}\text{C}$, H_2/N_2 flow rate of 100 mL/min).

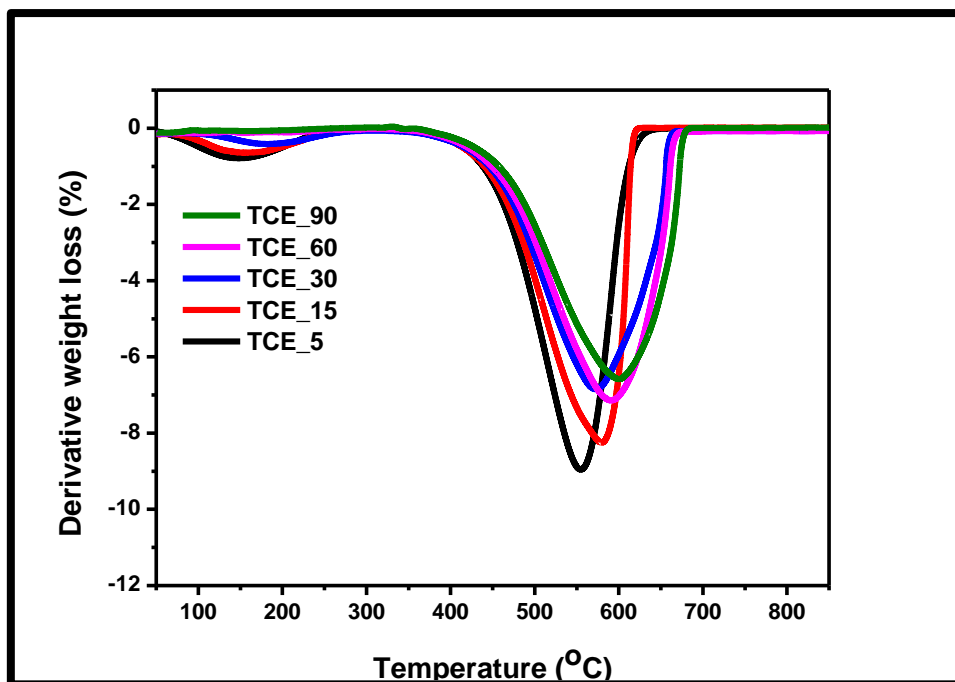


Figure 5. 17: DTG plots of CNFs synthesized at different reaction times ($T= 450^{\circ}\text{C}$, H_2/N_2 flow rate of 100 mL/min).

Table 5. 6: Summarizes maximum decomposition temperatures of CNFs at different time intervals

Sample	Decomposition Temperature ($^{\circ}\text{C}$)	
TCE_5	151	544
TCE_15	159	555
TCE_30	182	567
TCE_60	-	578
TCE_90	-	585

5.3.2. Synthesis of CNFs using different Ni precursors.

5.3.2.1. Characterization of NiO@HCSs catalyst using different Ni precursors

The effect of Ni precursor on the growth of CNFs was studied using different nickel compounds (nickel acetate hexahydrate, nickel chloride hexahydrate, and nickel nitrate). The Ni compounds were loaded inside the HCSs using a similar method discussed in **Chapter 3 (Experimental section)**. A loading of 5 wt% Ni (theoretically determined) was used to make the catalysts. The resulting products were denoted as Ni_chl, Ni_nit, and Ni_ace (labelled according to their nickel precursor).

5.3.2.1.1. Morphology analysis: TEM analysis of NiO@HCSs catalysts synthesized using different Ni precursors.

Figure 5.18 show representative TEM images of the NiO@HCSs catalysts made using different nickel precursors. All TEM images showed the presence of Ni particles on the HCSs framework. For Ni_nit, a few Ni nanoparticles (NPs) were observed within a single sphere. In contrast, nickel NPs in Ni_chl, and Ni_ace all appeared as small particles (irregular shaped) that formed agglomerates (**Figure 5.18b, c, see arrows**). Although the dispersion of Ni particles within the HCSs cavity slightly differed, the nickel crystallite sizes were similar. The nickel crystals were determined to be 14 ± 6 , 15 ± 5 and 15 ± 3 nm for Ni_nit, Ni_chl, and Ni_ace, respectively. It was also observed that most of the Ni (as NiO) resided inside the HCSs. The TEM images showed no significant changes in the morphology of the HCSs after Ni loading ($d = 426 \pm 5$ nm, HCSs ($d = 433 \pm 42$ nm, discussed in **Chapter 3**)).

However, the surface analysis (see **Appendix C, figure S5.2**) of the catalysts indicated a slight change in the surface areas of the catalysts after incorporation of Ni in the HCSs crystal structure. The surface area decreased from $395 \text{ m}^2/\text{g}$ (HCSs surface area) to 364, 355 and $349 \text{ m}^2/\text{g}$ for Ni_nit, Ni_ace and Ni_chl catalysts, respectively. This was ascribed to pore blockage of the HCSs pores by Ni particles. The samples exhibited a type IV isotherm with a H1 hysteresis loop, according to the IUPAC nomenclature. All catalysts revealed a pore size between 3-4 nm, which indicated the presence of mesopores.

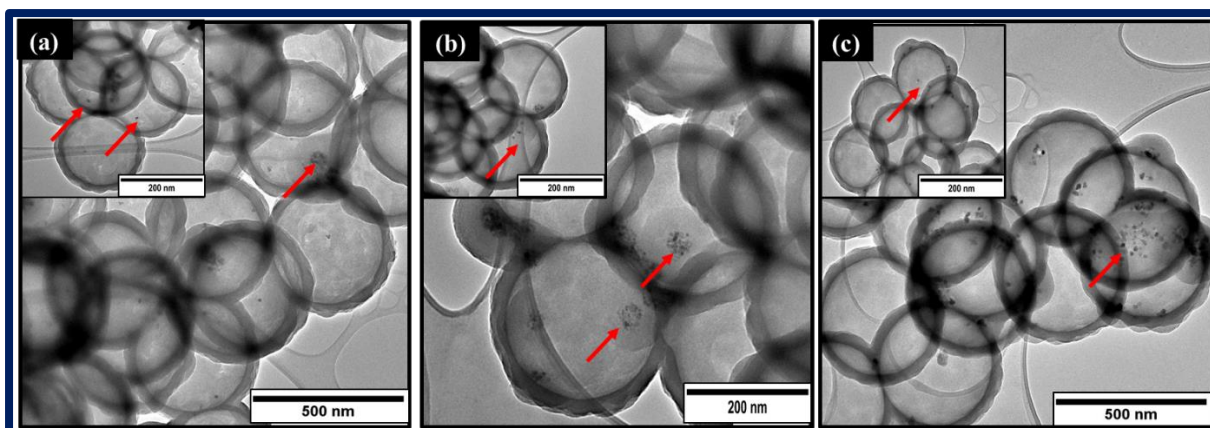


Figure 5. 18: TEM images of (a) Ni_nit, (b) Ni_chl and (c) Ni_ace catalysts

5.3.2.1.2. Structural analysis: XRD analysis of CNFs synthesized using different Ni precursors

XRD studies were done to ascertain the crystal structure of the carbon materials. The XRD patterns of the synthesized materials are shown in **figure 5.19**. A broad peak was observed at 2θ value of 21° assigned to the (002) graphite plane. It was however noted that the presence of this peak in the Ni_chl sample is very small. This observation was not expected, and no explanation can be given for this finding at present. Diffraction peaks were observed at 37° , 43° , 44° (very small twin peak) and 63° 2θ values. These peaks were assigned to both NiO and Ni species on the HCSs framework. The peaks were assigned to (111), (200), (111) and (200) planes of NiO/Ni, respectively [5, 15].

The NiO and Ni crystallite sizes were estimated using the Scherrer equation [16].

$$\text{Scherrer Equation..... } D_{hkl} = \frac{K\lambda}{\beta \cos \theta}$$

where D_{hkl} is the crystallite size, K - Scherrer's constant ($K=0.89$), λ -X-ray wavelength (0.179 nm), β = line broadening of full width half maximum diffraction peak in radians and θ = Bragg's angle.

The most intense diffraction peak of the as-synthesized materials characterized by the (200) plane at $2\theta = 43^\circ$ was used to estimate the average crystallite size of the NiO nanoparticles. Assuming that the NiO nanoparticles are spherical, the crystallite size of NiO was estimated to be 22 nm, 17 nm and 20 nm for Ni_chl, Ni_nit, and Ni_ace, respectively. The results obtained are consistent with the data obtained from TEM studies. The crystallite size of Ni could not be

determined. In addition, TEM and XRD studies revealed that the counter ion does not affect the size of the NiO nanoparticles.

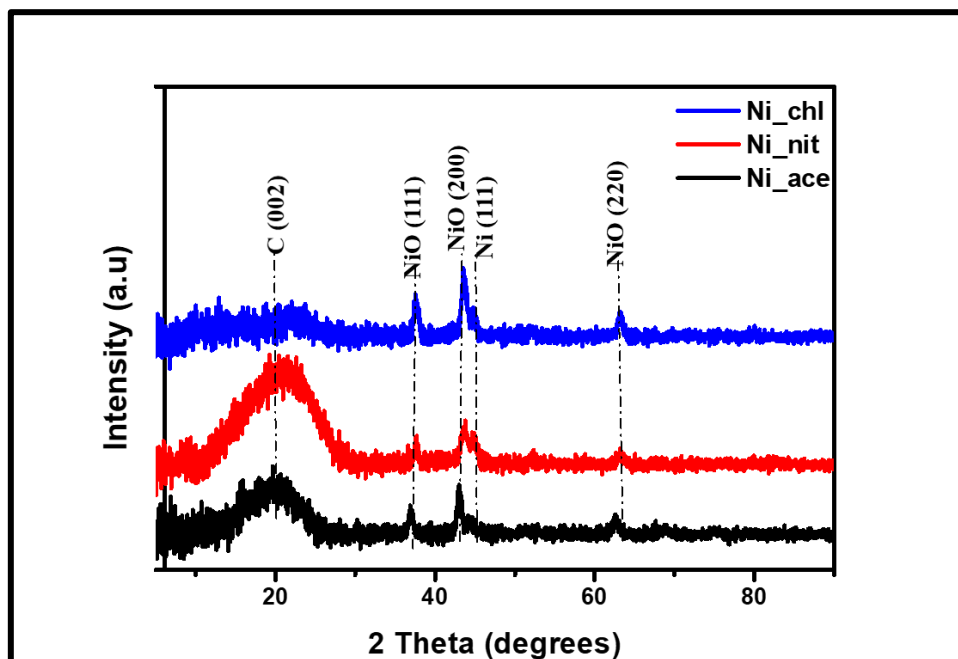


Figure 5. 19: XRD spectra of Ni_chl, Ni_nit and Ni_ace catalysts.

5.3.2.2. Synthesis of CNFs synthesized using different Ni precursors

5.3.2.2.1. Morphology analysis of CNFs synthesized using different Ni precursors: TEM analysis.

Before CNFs synthesis, TPR studies were conducted on the NiO@HCSs catalysts to deduce the reduction temperature of NiO nanoparticles. The TPR data (**Appendix C, figure S5.3**) revealed very small peaks, which was attributed to a low concentration of the NiO nanoparticles. These peaks appear at ~ 230 °C and 250 °C. In the studies undertaken, the reduction of NiO species from all three as-prepared catalysts occurred at *ca.* $T > 350$ °C (the estimate was made from the TPR data (**figure 3.12**)). Thus, in all cases, the NiO would have been reduced to Ni prior to CNF growth.

CNFs were synthesized by decomposition of TCE over the NiO@HCSs catalysts prepared from the different nickel compounds. Standard conditions were used for the synthesis of CNFs, i.e. the flow rate of hydrogen and nitrogen was both 100 mL/min. The CNFs were grown at 450 °C for 5 min. The resulting black carbonaceous soot was collected and characterized. The products were denoted as TCE_nit, TCE_chl, and TCE_ace (named after their nickel precursor catalyst).

Figure 5.20 shows TEM images of CNFs synthesized using different nickel compounds. The CNFs grown from all the catalysts show a dominance of a mono-directional growth of the CNFs from a single Ni crystal. The CNFs grown using Ni_chl catalyst showed fibers with predominantly a hollow central core (**figure 5.20a**, inset). The formation of this type of morphology has been attributed to the deformation of the metal particle during CNF growth which alters the relative rate of carbon diffusion and fiber nucleation [5]. In contrast, the CNFs grown from Ni_nit and Ni_ace formed CNFs with the hollow core (see **figure 5.21** for a clearer view of this morphology) and irregular shaped CNFs with rough outer edges. The diameter of the fibers was found to be 30 ± 7 , 24 ± 3 and 27 ± 7 nm for TCE_chl, TCE_nit, and TCE_ace, respectively. It was noted that the fiber diameter often exceeded the starting Ni particle size. The average diameter of Ni grains was found to be 32 ± 4 , 15 ± 3 and 25 ± 7 nm for TCE_chl, TCE_nit, and TCE_ace, respectively. This observation has been reported previously in the literature [3, 5, 13-15]. The yields obtained from all catalysts were about the same, *viz.* $\sim 27\%$ yield.

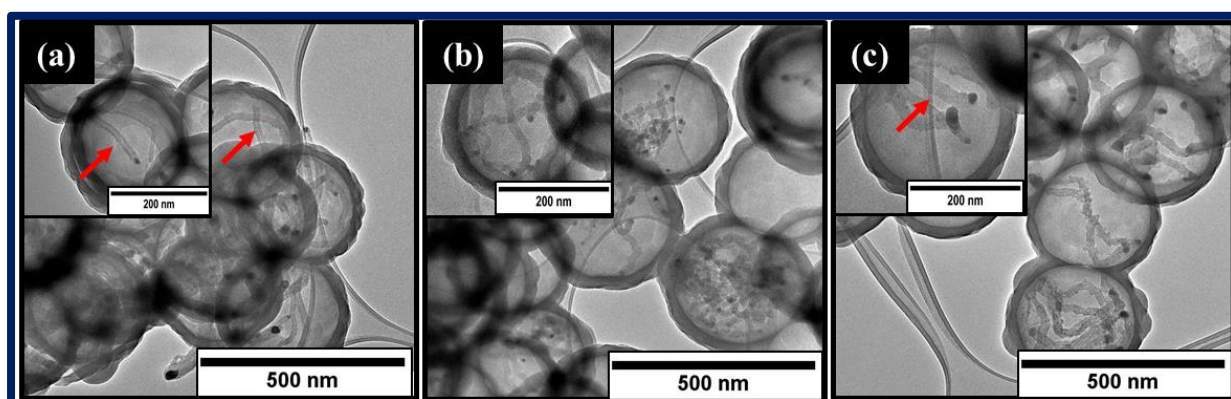


Figure 5. 20: TEM images of TCE_chl, TCE_nit, and TCE_ace, showing CNFs with a monomodal growth (synthesized at 450 °C, $H_2/N_2= 100$ mL/min, for 5 min).

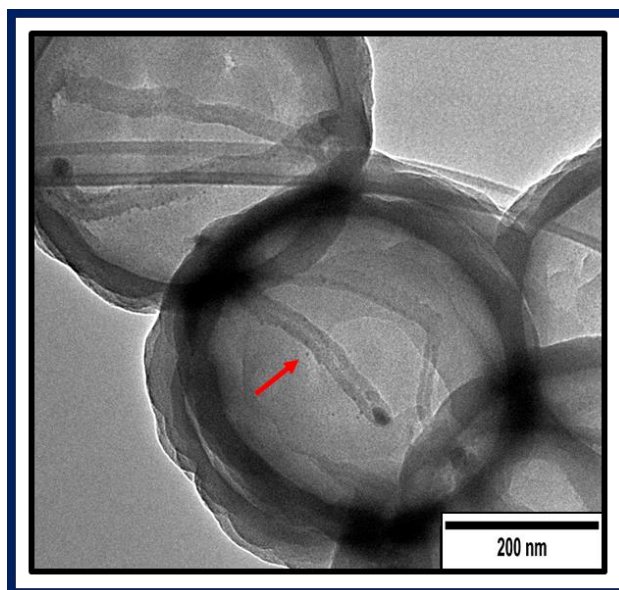


Figure 5. 21: TEM image of CNFs with a hollow central core.

5.3.2.2.2. Raman analysis of CNFs synthesized using different Ni precursors

Raman analysis was conducted to gauge the effect of Ni precursor on the growth of CNFs. The Raman spectra are shown in **figure 5.22** and reveal the presence of the D and G bands at approximately $1350 -1360 \text{ cm}^{-1}$ and $1590-1600 \text{ cm}^{-1}$, respectively [16-17]. The I_D/I_G ratio of the TCE_chl, TCE_nit, and TCE_ace (summarized in **Table 5.7**) were found to be 0.60, 0.63 and 0.50, respectively. It is evident from these values that using nickel acetate for the CNFs growth results in a more graphitic carbon framework.

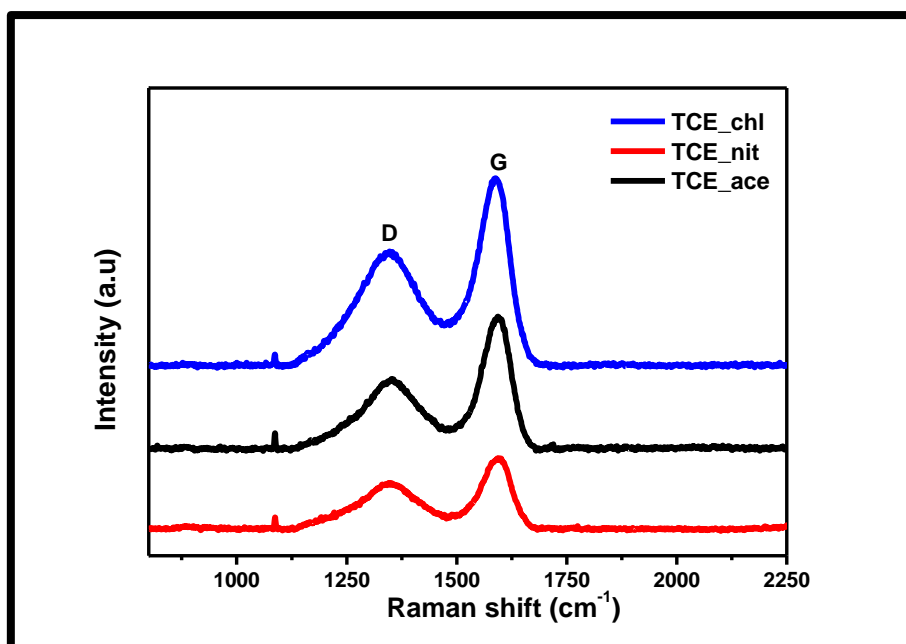


Figure 5. 22: Raman spectra of TCE_chl, TCE_nit, and TCE_ace (synthesized at 450 °C, $H_2/N_2= 100$ mL/min, for 5 min).

Table 5. 7: The I_D/I_G ratios of D and G peaks of the CNFs prepared from different Ni compounds

Material	D band peak position (cm^{-1})	G band peak position (cm^{-1})	I_D / I_G ratio
TCE_nit	1345	1590	0.63
TCE_chl	1343	1585	0.60
TCE_ace	1349	1591	0.50

5.3.2.2.3. TGA analysis of CNFs synthesized using different Ni precursors

TGA analysis was performed to investigate the influence of using different Ni precursors on the thermal stability of the synthesized CNFs. The TGA and their corresponding DTG plots recorded for the synthesized CNFs are presented in **figure 5.23** and **figure 5.24**, respectively. An interesting observation in the TGA profiles is that all materials gave no residual masses (0 wt. %). It is also noted that all catalysts were stable over a wide temperature range and only started decomposing at $T > 530$ °C.

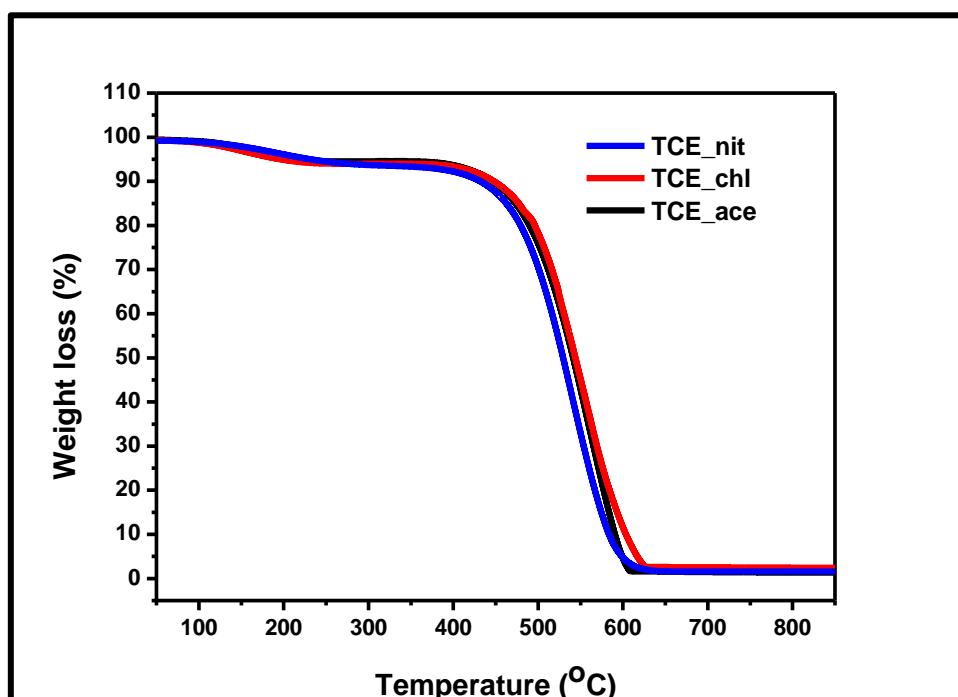


Figure 5. 23: TGA profiles of CNFs synthesized from different Ni compounds (synthesized at 450 °C, H₂/N₂= 100 mL/min, for 5 min).

The DTG plots (**figure 5.24**) provide information about the maximum decomposition temperature of the synthesized CNFs. It was observed that the as-prepared materials showed two decomposition temperatures (see **Table 5.8**). The TCE_nitrate, TCE_chl and TCE_ace CNFs showed maximum decomposition temperatures at 537, 543, and 545 °C, respectively. It was noted that CNFs synthesized using Ni_ace catalyst are slightly more thermally stable compared to other catalyst systems. This data corroborated the Raman data which revealed more graphitic carbon material.

Zielinska *et al.* [16] suggested that the difference in the thermal stabilities might be due to different interactions of metal nanoparticles with carbon atoms inducing defects in the crystal structure.

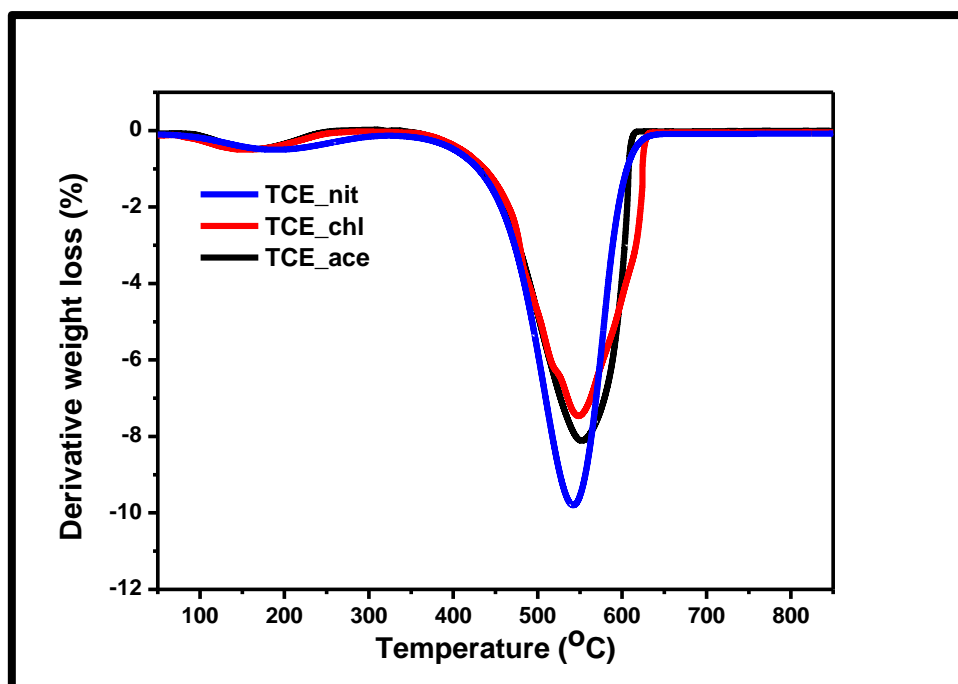


Figure 5. 24: DTG profiles of CNFs synthesized from different Ni compounds (synthesized at 450 °C, H₂/N₂= 100 mL/min, for 5 min).

Table 5. 8: Summarizes maximum decomposition temperatures of the as-prepared CNFs

Sample	Decomposition Temperature (°C)	
TCE _nit	165	537
TCE_chl	155	545
TCE_ace	165	544

Conclusions

In summary, carbon nanofibers were successfully grown on 0.5 wt% NiO@HCSs using TCE as a carbon precursor. The reaction parameter studies revealed that employing TCE for the growth of CNFs had a significant influence on the carbon yield and the morphology of the CNFs. In all studies, the formation of monomodal fiber growth from a single Ni crystallite was observed. TEM micrographs from the temperature study showed that the temperature affected the fiber morphology. Various fiber morphologies were noted as the temperature was varied; irregular shaped fiber with rough outer edges, flower-like morphology and straight fiber with

a hollow cavity. The flow rate study also showed differences in the morphology of the CNFs. At 20 mL/min, a tripod-like morphology was observed and increasing the flow rate resulted in the formation of dominantly monomodal straight CNFs, attributed to the restructuring of the Ni crystallites. The Raman and TGA studies showed changes in carbon morphology as the reaction parameters were varied.

Variation of the Ni counter ion revealed that different nickel compounds had a very modest influence on the fiber morphology. TEM images obtained from all nickel compounds showed that the as-prepared CNFs exhibited dominantly CNFs with a hollow central core. Raman spectroscopy studies showed that the CNFs synthesized using nickel acetate were more graphitic ($I_D/I_G = 0.50$) compared to the other nickel compounds. TGA studies corroborated the Raman results and showed that the CNFs synthesized from nickel acetate were more thermally stable.

Overall, the data obtained from the reaction parameter studies (temperature, time and flowrate) using TCE as a carbon source for the growth of CNFs showed different results from the acetylene study.

References

1. I.V. Mishakov, V.V. Chesnokov, R.A. Buyanov, A.L. Chuvilin, *Reaction Kinetics, Mechanisms and Catalysis*, 76 (2) (2002) 361-367.
2. S. Ya. Brichka, G.P. Prikhod'ko, Yu. I. Sementsov, A.V. Brichka, G.I. Dovbeshko, O.P. Paschuk, *Carbon*, 42 (2004) 2581–2587.
3. A. Shaikjee, N.J Coville, *Materials Letters*, 68 (2012) 273–276.
4. A. Nieto-Márquez, I Espartero, J. C Lazo, Amaya Romero, J.L Valverde, *Chemical Engineering Journal*, 153 (2009) 211–216.
5. A. Nieto- Márquez, J.L Valverde, M A. Keane, *Applied Catalysis A: General*, 332 (2007) 237–246.
6. A. Shaikjee, N. J. Coville, *Carbon*, 50 (2012) 1099–1108.
7. X. Qi, C. Qin, W. Zhong, C. Au, X. Ye, Y. Du, *Materials*, 3 (2010) 4142-4174.
8. R. Lv, F. Kang, W. Wang, J. Wei, J. Gu, K. Wang, D. Wu, *Carbon*, 45 (2007) 1433–1438.
9. N. Tang, W. Zhong, A. Gedanken, Y. Du, *Journal of Physical Chemistry B*, 110 (2006) 11772-11774.
10. G. Xu, B. Chen, H. Shiki, T. Katsumata, H. Takikawa, T. Sakakibara, S. Itoh, T. Ina, *Japanese Journal of Applied Physics*, 44 (2005) 1569.
11. H. Li, C. Shi, X. Du, C. He, J. Li, N. Zhao, *Materials Letters*, 62 (2008) 1472–1475.
12. Y. Chen, C. Liu, J-H. Du, H-M. Cheng, *Carbon*, 43 (2005) 1874–1878.
13. A. Shaikjee, P.J. Franklyn, N.J. Coville, *Carbon*, 49 (2011) 2950-2959.
14. M.S. Maubane, S.S. Bhoware, A. Shaikjee, N. J. Coville, *Diamond & Related Materials*, 72 (2017) 53-60.
15. M.S. Maubane, *Nickel and copper catalysed synthesis of carbon fibers*, Ph.D. Thesis, University of the Witwatersrand, Johannesburg, (2013).
16. B. Zielinska, B. Michalkiewicz, E. Mijowska, R.J. Kalenczuk, *Nanoscale Research Letters*, 10 (2015) 430.
17. Y. Li, C. Pan, J. Wang, *Material Science*, 39 (2004) 1091-1094.
18. E. -J. Shin, M.A. Keane, *Applied Catalysis B: Environmental*, 18 (1998) 241-250.
19. L. D. Cherukuri, G. Yuan, M. A. Keane, *Topics in Catalysis*, 29 (3-4) (2004) 119-128.
20. J. Zhang, T.C. Ekström, S.K. Gordeev, M. Jacob, *Materials Chemistry*, 10 (2000) 1039.

21. C. Pham-Huu, N. Keller, V.V. Roddatis, G. Mestl, R. Schlögl, M.J. Ledoux, *Physical Chemistry Chemical Physics*, 4 (2002) 514-521.
22. L. Ci, Y. Li, B. Wie, J. Liang, C. Xu, D. Wu, *Carbon*, 38 (2000) 1933-1937.

CHAPTER 6

General conclusions and recommendations

The research study focused on methods to encapsulate Ni inside the HCSs (Ni@HCSs) and to investigate the concept of using HCSs as a nanoreactor to build carbon structures (CNFs) inside the HCSs with controllable size and morphology from the encapsulated nickel catalyst using the CVD approach. Different nickel catalysts, carbon sources and nickel compounds were employed for the synthesis of CNFs. The as-synthesized Ni@HCSs and the HCS + CNFs composites were characterized using various techniques (SEM, TEM, TGA, XRD, TPR, BET and Raman spectroscopy).

6.1. Conclusions

The control over the size of nickel nanoparticles through the metal confinement strategy within the HCSs was studied. The encapsulation of nickel inside the HCSs allowed better control of the nickel particle size compared to their counterparts deposited outside the HCSs surface. The nickel particle size narrowed from 35 ± 11 nm to 22 ± 5 nm (on encapsulation), both at 5 wt%. The use of a silica template for nickel encapsulation resulted in both the removal of the silica and nickel nanoparticles by HF. When a polystyrene template was used, most of the nickel nanoparticles were incorporated inside the HCSs at a lower loading (0.5 wt%) compared to a high loading (5 wt% and 10 wt%).

The data obtained revealed that the hollow cavity of the HCSs can be exploited to build structures within the hollow cavity. The CNFs were successfully synthesized outside and inside the HCSs. The synthesis of CNFs outside the HCSs resulted in the enormous growth of the CNFs compared with the CNFs growth inside, thus the control over the morphology and size of the CNFs outside the HCSs was difficult. The TEM images of the CNFs synthesized inside the HCSs (0.5 wt%) showed the formation of thick and thin CNFs with helical and worm-like morphology confined inside the HCSs walls. The average diameter of the linear/helical CNFs was found to be *ca.* 29 nm and 10 nm for worm-like CNFs (450 °C). This indicated that small nickel particles result in the formation of CNFs with a worm-like morphology and larger particles resulted in the formation of linear/helical CNFs. The TGA studies showed that the

thermal stability of the HCS+ CNFs composite increased compared to the pure HCSs as the reaction parameters were varied (temperature, time and flow rate).

The use of TCE as a carbon precursor resulted in unique and interesting CNFs morphologies. The CNFs with rough edges, flower-like morphology, tripod-like, and a hollow central core were formed. These results indicated that the catalyst continuously restructured as the reaction parameters (temperature, time and flow rate) were varied. The Raman and TGA studies showed that the CNFs synthesized using TCE as a carbon precursor resulted in the formation of a highly ordered carbon as the reaction parameters (temperature and growth time) increased.

The study of the effect of using different nickel compounds revealed that different nickel compounds had an insignificant effect on the morphology of the CNFs. The TEM images showed the formation of CNFs predominantly with a hollow central core and rough outer edges in all the samples synthesized. TGA studies showed that the different nickel compounds had a modest effect on the thermal stability of the CNFs in comparison with the HCSs.

Moreover, the study showed that different carbon precursor influences the fiber growth (see **figure 6.1**). Acetylene resulted in the formation of dominantly monomodal and bimodal fiber growth with straight and helical morphology. At high temperature (600 °C), nickel nanoparticle fragmentation was observed, and this resulted in the formation of thin fibers with a worm-like morphology. In contrast, the use of TCE as a carbon precursor resulted in the formation of monomodal fiber growth with rough outer edges. At 600 °C, nickel fragmentation was not observed instead CNFs with a flower-like and hollow central core were formed.

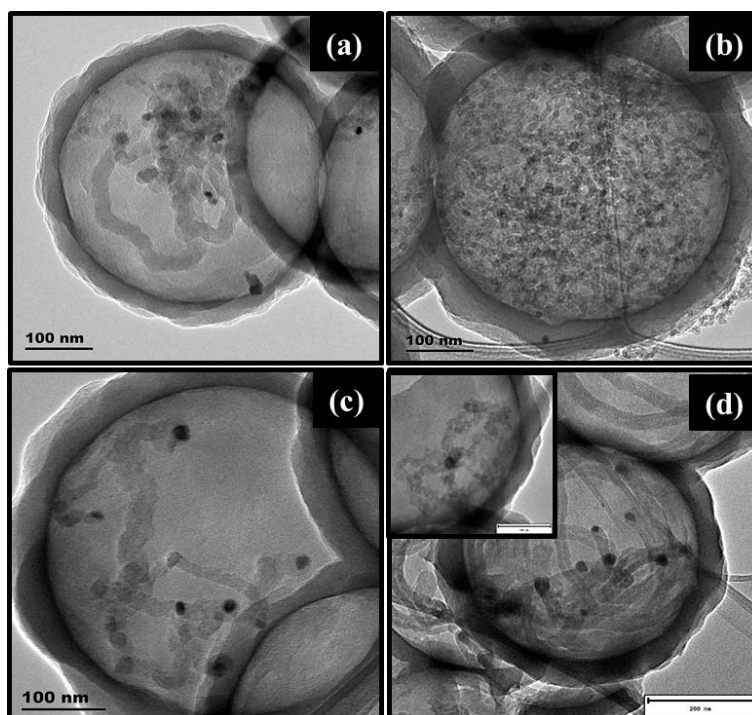


Figure 6. 1: TEM images of CNFs synthesized using different carbon precursors, Acetylene (a, b) and TCE (c, d) synthesized at 450 °C and 600 °C.

6.2. Recommendations

The studies conducted in this work revealed the viability of building structures inside the hollow carbon spheres (HCSs). The carbon nanofibers were fully confined within the cavity of HCSs at lower loadings and this led to control of the length of the CNFs grown. The relationship between the particle size, morphology, and the CNFs morphology could not be effectively determined as the fibers continued growing. To have a better understanding of the effect of particle size, morphology and carbon source on the synthesis of the CNFs, it is therefore recommended that further studies be undertaken on the preparation of the HCSs with different porosities and functional groups. This could allow a better assessment of the influence of reaction conditions on the fiber growth inside the hollow carbon spheres and prevent deposition of Ni outside the HCSs.

Moreover, the results attained in this study could pave a way in employing other carbon precursors such as CO, ethylene, etc. to building other carbon nanomaterials with different morphologies. This could open a window in the development of new class of catalysts and further potential applications in many fields.

In addition, we further recommend that a study should be undertaken to investigate the kinetics of the reaction (e.g. turnover frequencies and other kinetic parameters). This would shed more light on possible reaction mechanisms, reaction conditions, or precursors that are desirable for the reaction.

Supplementary Information

Appendix A

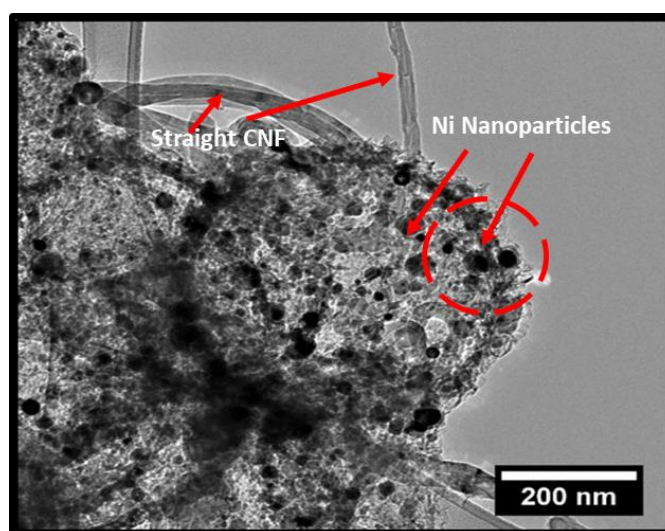


Figure S3. 1: TEM image of Ni@HCSs-1.

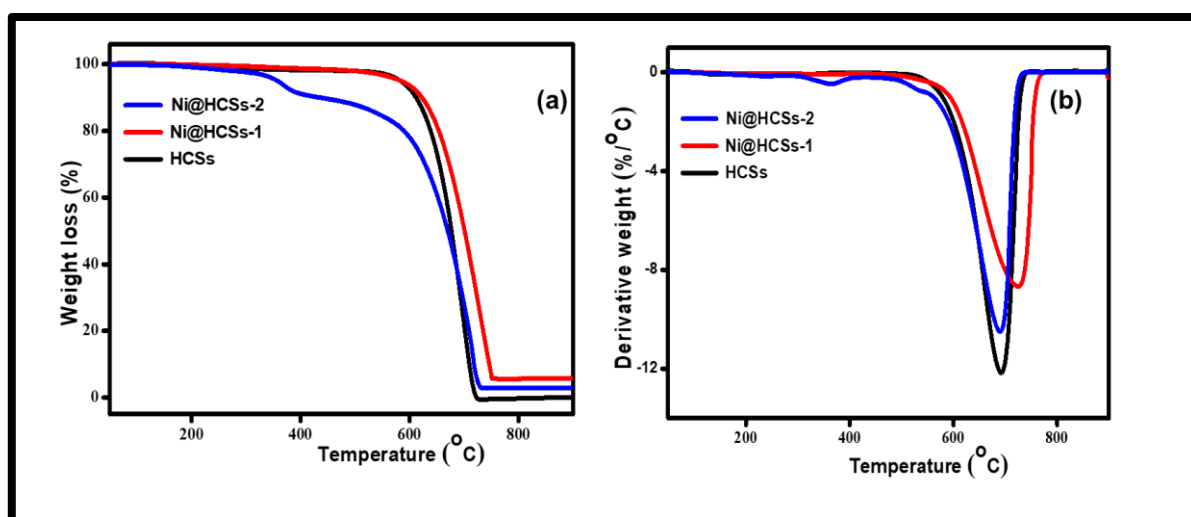


Figure S3. 2: TGA profiles (a) and derivative curves (b) of the HCSs and NiO@HCSs catalysts synthesized using silica template.

Table S3. 1: Surface area data of HCSs and NiO@HCSs catalysts synthesized using silica template

Sample	Surface area (m ² /g)	Pore size (nm)
HCSs	121 ± 1.	15
Ni@HCS-1	166 ± 4	13.2
Ni@HCS-2	61 ± 1	30.5

Appendix B

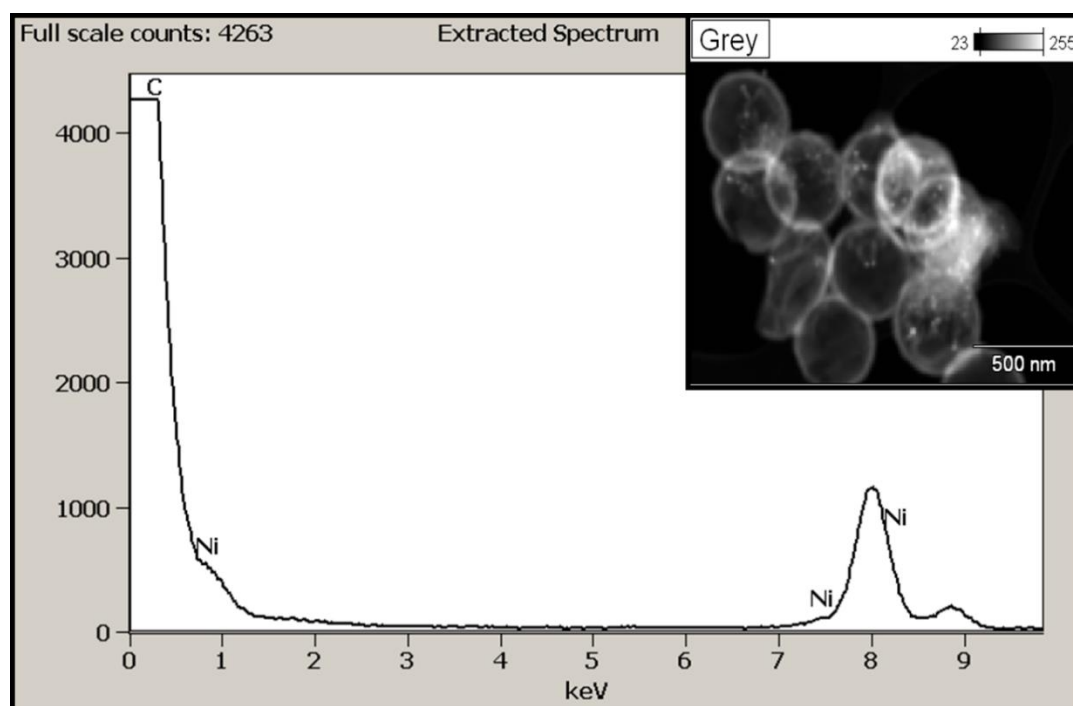


Figure S4. 1: EDS spectra of CNFs synthesized at 450 °C for 5 min using acetylene as a carbon source.

Appendix C

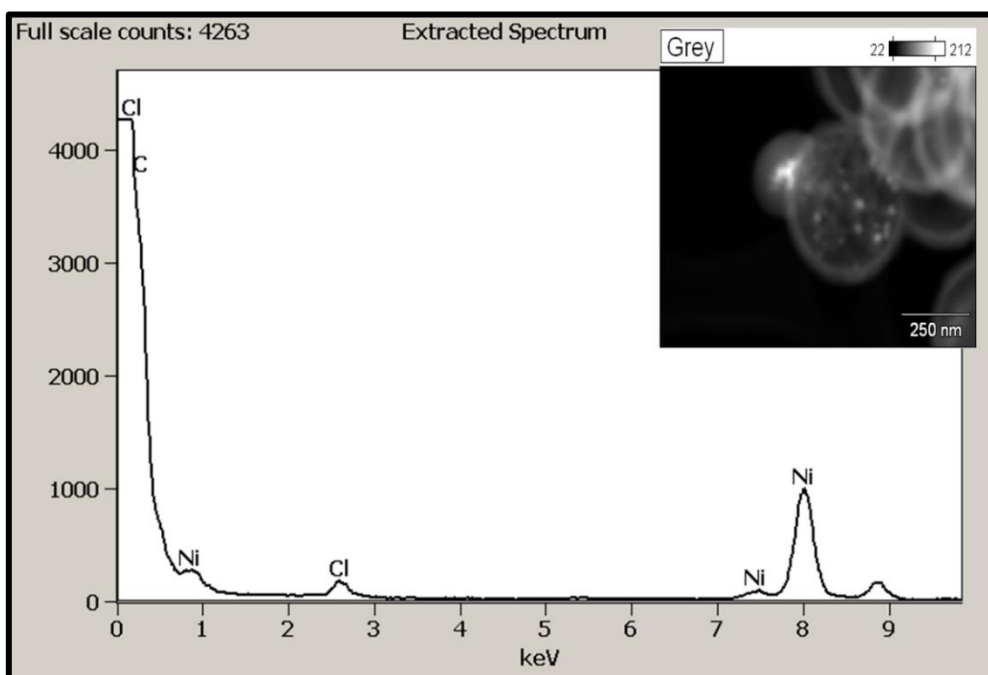


Figure S5. 1: EDS spectra of CNFs synthesized at 450 °C for 5 min using TCE as a carbon source.

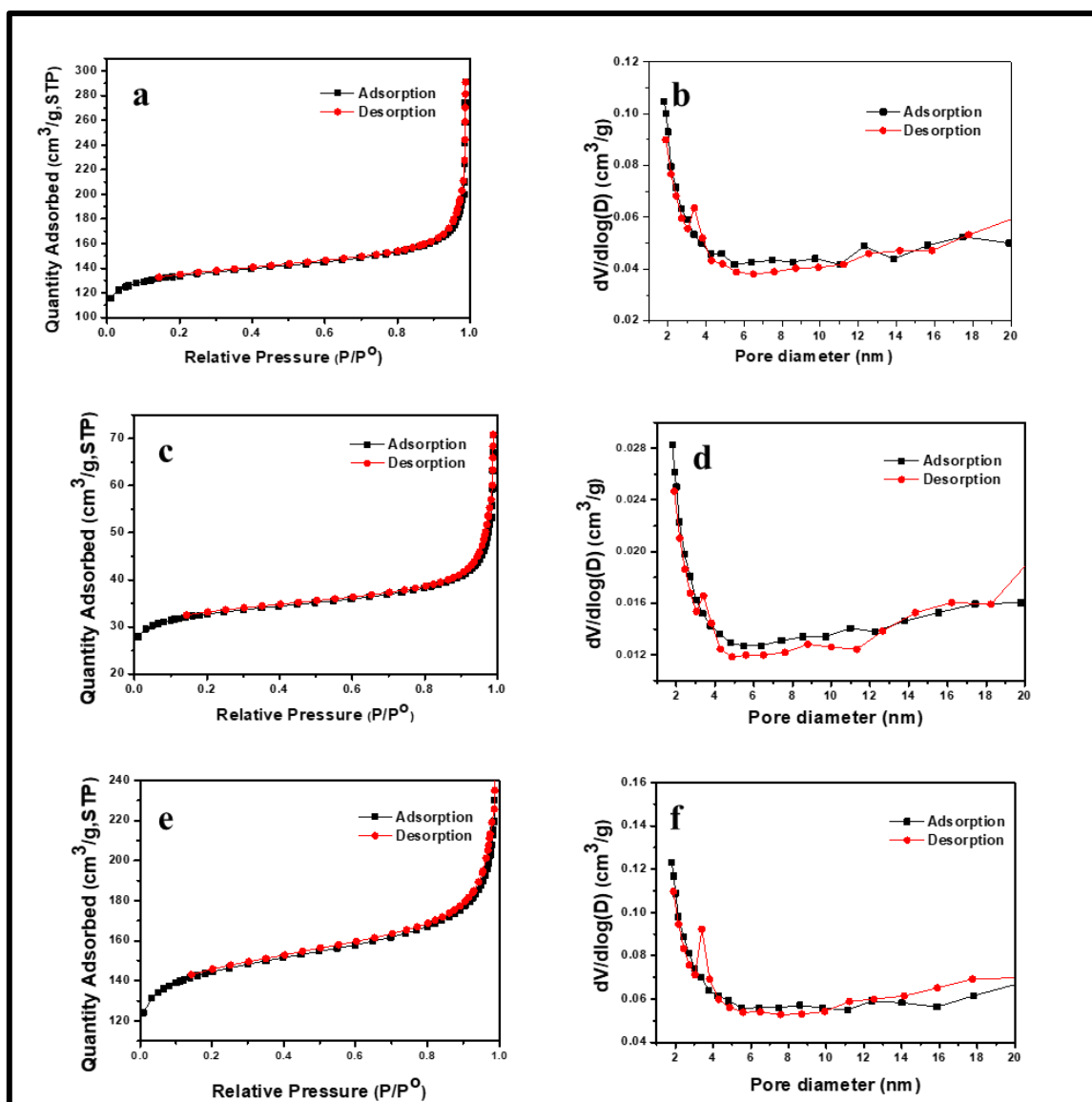


Figure S5. 2: N₂ adsorption-desorption and corresponding pore size distribution curves of NiO@HCSs catalysts (a, b) Ni_{nit}; (c, d) Ni_{ace} and (e, f) Ni_{chl}.

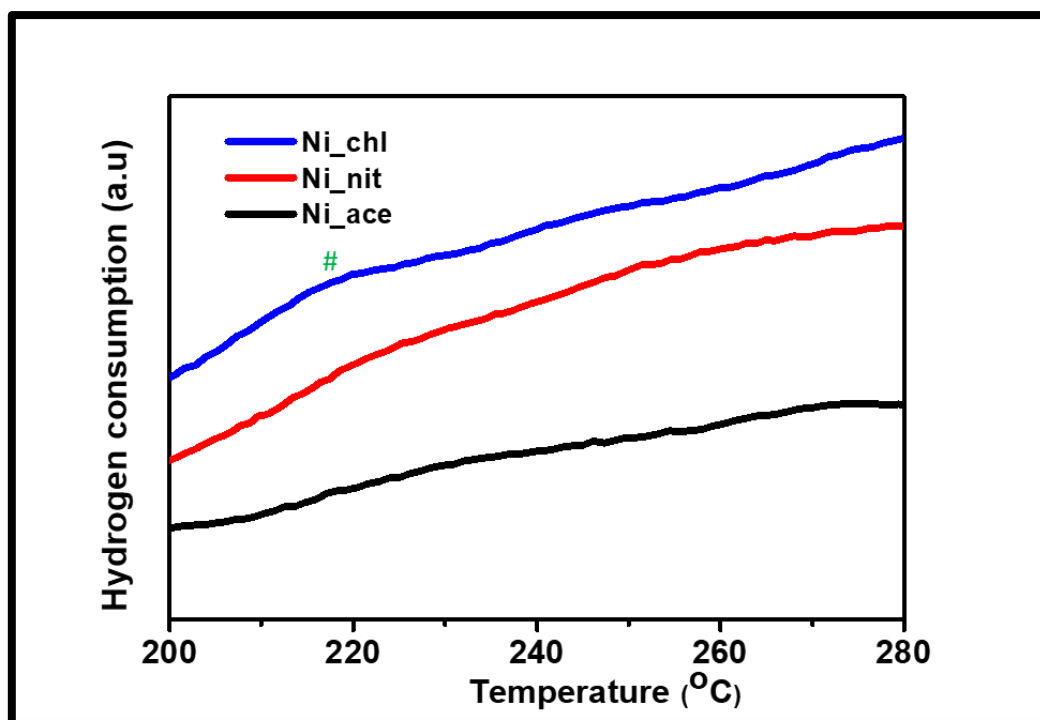


Figure S5. 3: TPR profiles of NiO@HCSs catalysts prepared from different nickel compounds.

